Rheology and structure of foams

Zur Erlangung des akademischen Grades einer

DOKTORIN DER INGENIEURWISSENSCHAFTEN (DR.-ING.)

von der KIT-Fakultät für Chemieingenieurwesen und Verfahrenstechnik des
Karlsruher Instituts für Technologie (KIT)
genehmigte

DISSERTATION

von
Dipl.-Ing. Annika Ricarda Völp
aus Frankfurt am Main

Tag der mündlichen Prüfung: 25.05.2022

Erstgutachter: Prof. Dr. Norbert Willenbacher

Zweitgutachterin: Prof. Dr. Regine von Klitzing

Preface

This thesis is based on four peer-reviewed scientific journal articles. All articles have been drafted during my experimental work on foams and interfaces at Karlsruhe Institute of Technology (KIT), Institute of Mechanical Process Engineering and Mechanics in the group of Applied Mechanics from March 2015 to December 2020.

An introduction to the current state of science on foams is provided at the beginning of this thesis. The main body of this thesis consists of following publications:

1. High throughput object recognition and sizing in disperse systems using an image processing tool based on template matching

Annika R. Völp, Felix Fessler, Jasmin Reiner, Norbert Willenbacher

In: Chemical Engineering & Technology

2. In-situ rheological and structural characterization of milk foams in a commercial foaming device

Annika R. Völp, Lisa Kagerbauer, Jan Engmann, Deniz Z. Gunes, Cécile Gehin-Delval, Norbert Willenbacher

In: Journal of Food Engineering

3. Structure and rheology of foams stabilized by lupin protein isolate of *Lupinus.angustifolius*

Annika R. Völp, Jonas Seitz, Norbert Willenbacher

In: Food Hydrocolloids

4. Elasticity and yield stress of foams: Contribution of interfacial elasticity

Annika R. Völp, Norbert Willenbacher

In: Soft Matter

The thesis concludes with a summary and an outlook.

Acknowledgements

Diese Seiten sind das Resultat meiner Arbeit in einer Zeit, in der mein Leben von großen Veränderungen geprägt war – erste Arbeitsstelle, Familiengründung, Wohnungsbau.
Es war nicht selten eine große Herausforderung meine Bestrebungen und diese Arbeit, mit meinen Pflichten und Wünschen zu vereinbaren. Dabei haben mir viele Menschen geholfen, die alle auf unterschiedliche Weise einen Anteil zum Gelingen meiner Doktorarbeit beigetragen haben. Diesen Menschen möchte ich allen von Herzen danken und nur einige davon seien hier erwähnt:

Vor allen, möchte ich meinen Eltern danken, die mich Lebzeiten unterstützt und mir meinen Werdegang ermöglicht haben. Danke für jedes Schulbrot, danke, dass ihr mir ein Studium ermöglicht habt, danke für jedes Lob und für eure Zeit und Aufmerksamkeit, die ihr mir und euren Enkeln gebt.

Norbert, ich danke dir für deine Geduld und die vielen Stunden, die du in unsere Arbeit investiert hast, für das Wissen und die Fertigkeiten, die du mich gelehrt hast, und die Ermutigungen zum Weitermachen. Danke auch für die zahlreichen Inspirationen aus Kunst, Politik und sozialem Engagement, die mir am lebhaftesten in Erinnerung bleiben werden.

Александр, спасибо, что ты всегда поддерживаешь и вдохновляешь меня идти дальше. Твоя энергия и сила воли ведут меня.Ты лучший муж и отец. Я тебя люблю.

Yelena und Lukjan, danke dafür, dass ihr mir immer wieder zeigt worauf es wirklich ankommt und alle noch so groß erscheinende Probleme relativiert. Ich hoffe ihr verzeiht mir, dass ihr zu selten meine ungeteilte Aufmerksamkeit hattet.

Danke Hansen und Laura, für die unermesslich großen Kredite auf meinem Kinderbetreuungskonto. Danke, auch an Carsten, Rese, Johann, Jaque und Fabi für die lebenswerten Momente mit euch, die mir Erholung und die Kraft zum Weitermachen gaben, immer wenn ich sie am nötigsten hatte.

Luba, ďakujem, že vždy kŕmite mňa a moju rodinu láskou a oddanosťou.

Ceren, birçok iyi tartışma için teşekkür ederiz. Senin sayende her gün iş yerime gelmeye değerdi.

Moritz, danke, dass du mein größter Kritiker und mein bester Sekretär warst.

Ronald, gracias, cada día iluminaste nuestra oficina con tu sonrisa cordial.

Ophélie, merci pour chaque câlin et pour avoir donné un sens à ma dernière année à l'AME.

Danke an Paul, Boris, Clara, Leon, Moni, Steffen R., Katharina, Irene, Frank, Erin, Walter, Johannes, Müge, Chenhui, Johanna, Annika, Steffen F., Hongye, David, Karsten, Claude, Bernhard, Beate, Ekaterina, Jennifer, Lilie, Patrick, Max, Karla, Kasia, Katrin, Karim, Yiliang, Felipe, Bruna, Jonas, Kevin, Wolf und Bo, die die Arbeitsgruppe AME zu einem wunderbaren Arbeitsplatz gemacht haben!

Danke, Christina Avelia, Felix Fessler, Jan Geerds, Jonas Seitz, Joshua Möhrmann, Lisa Kagerbauer, Ludwig Höfert, Marian Schwenkschuster, Oliver Stratil, Pascal Zimmerer, Ting Xu für euren Beitrag zu meiner Doktorarbeit. Ich danke Jan Engmann für die Wertschätzung und Zusammenarbeit. Ich danke Prof. Regine von Klitzing für die Korrektur, Prof. Heike Karbstein, Prof. Manfred Willhelm und Prof. Wiebke Drenckhan für den Zugang zu ihren Geräten.

Abstract

Dispersing air into a solution of surface-active species, produces foam with rheological properties that dramatically differ from those of the Newtonian solution. When the foam's gas volume fraction exceeds the maximum bubble packing fraction, the interfacial tension along the bubble separating lamellae bestows bulk elasticity on the foam at small strain. When the strain exceeds the specific yield point, the foam structure breaks, i.e. the bubbles rearrange, and the foam flows like a viscous fluid. Owing to attributes like the visco-elastic rheology, and the increase in volume and interfacial area, foams are applied in food, cosmetic, cleaning or pharmaceutical products. Besides the rheology, which is linked to the foam structure, the foam structure itself plays an important role in the stability of the foam and the perception of a foamed product.

The aims of this thesis are to investigate the relationship between foam structure and rheology in foam columns subject to free drainage and to evaluate whether it exists a relationship between interfacial elasticity of foaming solutions and the yield stress or shear modulus of corresponding foams universally valid among different foaming systems. Based on these data a predictive model relating foam rheological parameters and interfacial elasticity of corresponding solutions should be developed.

Foam rheology has been investigated in terms of elastic shear modulus and yield stress and the foam structure has been characterized in terms of gas volume fraction and bubble size distribution for a broad variety of foaming agents comprising of small molecular weight surfactants, block copolymers, plant- and animal-derived proteins, silica nanoparticles and complex food systems. The interfacial elasticities of the same foaming solutions were determined in shear and oscillation. A suitable foaming process was set up similar to the membrane foaming apparatus previously presented by Bals et al. (Bals and Kulozik, 2003a). The gas volume fraction was determined using the correlation with the electric conductivity of the foam. To capture the bubble size distribution, an endoscopic setup combined with automated image analysis was developed that enables to monitor size distribution changes in situ with high temporal resolution.

The gas volume fraction and bubble size distribution measurement techniques were additionally implemented in the construction of an in-situ foam characterization cell based on a commercial milk whipper. The cell allowed for determination of temporal changes of these foam structure characteristics with a spacial resolution of 1 cm along the direction of gravity. The cell was mounted onto a torque rheometer with a customized vane rotor and gradients in yield stress were determined in foams made from different milk types. Spacial and temporal changes in foam yield stress correlated with bubble size and gas volume fraction according to the currently known, phenomenological model.

In particular, the foamability and foam characteristics of protein isolate from lupin seeds were probed under changes of physico-chemical conditions in the protein solution. The lupine protein yields foam with great robustness to heat treatment and were found to display a promising base for the formulation of vegan aerated food products. A lupin plant milk was formulated with foam properties similar to those of bovine milk. Exemplarily for other protein stabilized foams, the foam stabilizing effect of lupin protein aggregates, sufficiently big to block plateau channels, was

investigated and the widely assumed foam drainage retarding mechanism was evidenced in endoscopic video observations.

The effect of ionic strength and pH on foams was investigated also for block copolymer solutions, bovine serum albumin solutions, and silica nanoparticle dispersions. The interfacial elastic modulus in shear and dilation was determined for the different foaming solutions and the results cover a broad range of two decades. This allowed us to quantify the contribution of interfacial elasticity on foam elasticity and yield stress. A common scaling of these rheological characteristics with a generalized Laplace pressure, i.e. the sum of interfacial tension and twice the interfacial elastic modulus divided by the bubbles' Sauter radius, was found. Deviation from this scaling was observed for nanoparticle stabilized foams and protein solutions at high ionic strength. We hypothesize that in these cases lamellae spanning networks, not governed by the interfacial elasticity, additionally contribute to the foam shear modulus and yield stress.

Zusammenfassung

Das Dispergieren von Luft in Lösungen aus oberflächenaktiven Stoffen erzeugt Schäume mit rheologischen Eigenschaften, die sich drastisch von jenen der Newtonischen Lösungen unterscheiden, wenn der Gasvolumenanteil die maximalen Packungsdichte der Blasen übersteigt. Die Grenzflächenspannung entlang der Lamellen, die die Blasen voneinander abgrenzen, verleiht dem Schaum unter niedriger Scherbeanspruchung elastischen Charakter. Übersteigt die Deformation die schaumspezifische Fließgrenze, bricht die Schaumstruktur auf, d.h. Blasen gleiten aneinander ab, und der Schaum fließt gleich einer viskosen Flüssigkeit. Aufgrund von Eigenschaften wie der viskoelastischen Rheologie, der Volumen- und der Grenzflächenvergrößerung werden Schäume in Lebensmitteln, Kosmetika, Reinigungsmitteln oder pharmazeutischen Produkten eingesetzt. Neben der Rheologie, die mit der Schaumstruktur korreliert, spielt die Schaumstruktur selbst eine wichtige Rolle für die Stabilität des Schaums und die Wahrnehmung eines geschäumten Produktes.

Ziel dieser Arbeit ist, den Zusammenhang zwischen Schaumstruktur und -rheologie in Schäumen, die der freien Dränage unterliegen, zu untersuchen. Des Weiteren gilt zu evaluieren, ob ein Zusammenhang zwischen der Grenzflächenelastizität von Lösungen und der Fließgrenze bzw. dem Schermodul der daraus hergestellten Schäume existiert, welcher für verschiedene Schaumsysteme universell gültig ist. Basierend auf diesen Daten soll ein Modell entwickelt werden, das die rheologischen Parameter von Schäumen und die Grenzflächenelastizität der entsprechenden Lösungen in Beziehung setzt.

Die Schaumrheologie und die Schaumstruktur wurde für eine Vielzahl von Schaumbildnern, bestehend aus niedermolekularen Tensiden, Blockcopolymeren, pflanzlichen und tierischen Proteinen, Silica-Nanopartikeln und komplexen Lebensmittelsystemen, charakterisiert. Für alle Schäume wurden während der Dränage das elastische Schermodul, die Schaumfließgrenze, der Gasvolumenanteil und die Blasengrößenverteilung gemessen. Schäume mit enger Blasengrößenverteilung wurden mittels Begasung der Lösungen durch eine Glasmembran in Anlehnung an die zuvor von Bals et al. (Bals and Kulozik, 2003a) vorgestellte Schäumungsapparatur hergestellt. Die Gasvolumenanteile wurden mittels Messung der elektrischen Leitfähigkeit des Schaums bestimmt. Zur Erfassung der Blasengrößenverteilung wurde ein endoskopischer Aufbau in Kombination mit einer automatisierten Bildanalyse entwickelt, der es ermöglicht, Änderungen der Größenverteilung in situ mit hoher zeitlicher Auflösung zu verfolgen. Die Grenzflächenelastizitäten der wässrigen Lösungen, die auch zur Schaumherstellung dienten, wurden in Scherung und Dehnung bestimmt.

Die Messmethoden für den Gasvolumenanteil und die Blasengrößenverteilung wurden zusätzlich in eine in-situ Schaumcharakterisierungszelle, basierend auf einem kommerziellen Milchschäumer, intergiert. Der Aufbau ermöglichte die Bestimmung der zeitlichen Veränderungen dieser Schaumstruktureigenschaften mit einer räumlichen Auflösung von 1 cm entlang der Schwerkraftrichtung im Schaum. Die Zelle wurde auf ein Rotationsrheometer mit einem hierfür entwickelten Flügelrotor montiert, um Gradienten der Schaumfließgrenze für verschiedenen Milchsorten zu bestimmen. Die räumlichen und zeitlichen Veränderungen der

Schaumfließgrenze korrelierten mit der Blasengröße und dem Gasvolumenanteil gemäß dem gegenwärtig anerkannten, phänomenologischen Modell.

Insbesondere wurden die Schäumbarkeit und die Schaumeigenschaften von Lösungen von Proteinisolat aus Lupinensamen mit verschiedenen Temperaturbehandlungen, pH-Werten und Ionenstärken untersucht. Es wurde gezeigt, dass sich aus Lupinenproteinlösungen mit großer Robustheit gegenüber Wärmebehandlung, stabile Schäume erzeugen lassen. Damit birgt Lupinenprotein Potential für die Formulierung von veganen, geschäumten Lebensmitteln. Es wurde eine Lupinen-Pflanzenmilch formuliert, deren Schaumeigenschaften mit denen von Kuhmilch vergleichbar sind. Exemplarisch für andere proteinstabilisierte Schäume wurde die schaumstabilisierende Wirkung von Lupinenproteinaggregaten, die groß genug sind, um Plateaukanäle zu blockieren, untersucht. Die weithin angenommene Behinderung der Schaumdränage durch die Aggregate konnte in endoskopischen Videobeobachtungen nachgewiesen werden.

Der Einfluss von Ionenstärke und pH-Wert auf Schäume wurde auch für Blockcopolymer-Lösungen, Rinderserumalbumin-Lösungen und Silica-Nanopartikel-Dispersionen untersucht. Der Grenzflächen-Elastizitätsmodul in Scherung und Dehnung wurde für die zu schäumenden Lösungen bestimmt und deckt einen breiten Bereich von zwei Dekaden ab. Dies ermöglichte es, den Beitrag der Grenzflächenelastizität zur Schaumelastizität und Fließgrenze zu quantifizieren. Beide dieser rheologischen Parameter skalieren mit einem verallgemeinerten Laplace-Druck, gegeben durch die Summe aus Grenzflächenspannung und dem zweifachen Grenzflächenelastizitätsmodul geteilt durch den Sauter-Radius der Blasen. Abweichungen von dieser Skalierung wurden für nanopartikelstabilisierte Schäume und Proteinlösungen bei hoher Ionenstärke beobachtet. Es wird angenommen, dass in diesen Fällen lamellenübergreifende Vernetzung der Partikel oder Proteine, welche nicht in der Grenzflächenelastizität abgebildet wird, zusätzlich zum Schermodul und zur Fließgrenze des Schaums beiträgt.

Content

1 Theoretical background and research proposal

1.1 Research proposal

The greater aim of this thesis is to gain a deeper understanding and better control of the rheological and structural properties of foams. In particular, the investigation on gravity driven gradients in foam structure and rheology and the relationships between structure and dynamics at different length scales is focused. A multi-scale approach is used, which includes investigations at the macroscopic foam and the air/liquid interface. This requires different methodological approaches and developments of measurement setups allowing for in-situ characterization of transient phenomena with spacial resolution.

The size distribution of gas bubbles dispersed in a transparent liquid at low gas volume fractions can be accessed by endoscopic imaging techniques combined with bubble detection algorithms. However, automated bubble detection becomes challenging for densely packed foams with high gas volume fraction. Because of light scattering at the foam lamellae, strongly varying contrast and reflections on the foam images prevent bubble detection based on simply image binarization. Therefore, the first objective of this thesis was to develop an endoscopic setup to image densely packed bubbles at any position inside the foam with even contrast and to automatize the bubble detection. The latter enables fast analysis of long image sequences and thereby capture bubble size distributions with high temporal resolution.

Besides the bubble size distribution, the gas volume fraction defines the foam structure and both characteristics are linked as the foam drainage promotes foam coarsening and vice versa. Consequently, in a foam subject to free drainage gas volume fraction and bubble size gradients evolve in the direction of gravity and intensify with propagating foam age. The foam stiffness plays an important role for most aerated products and can be characterized by its yield stress which decreases with increasing bubble size and increases quadratically with gas volume fraction. In draining foams, these effects might mutually cancel out each other and the spacial and temporal changes of foam yield stress are not obvious. A setup for foam generation and in-situ characterization of foam structure and yield stress during drainage at various heights inside the foam was developed. This setup is based on a commercial milk whipper and was evaluated using various milk types.

In view of the growing demand of the food industry for aerated products based on plant proteins, an investigation on lupin protein stabilized foams was carried out. With this thesis, the findings of previous studies on foam stability under different conditions in lupin protein solutions (pH, salt

concentration, addition of thickeners) were extended with information on the foam and interfacial rheological properties.

In preliminary work, it was shown for milk proteins that yield stress and shear modulus of foams are directly linked to interfacial rheological properties of the corresponding foaming solutions. Based on these results, the research thesis has the objective to test whether the correlations between foam rheology and interfacial elasticity of the corresponding milk protein solution also apply to other foaming systems. Small and large molecular weight surfactants, different proteins, and form-invariant nanoparticles were used for foam stabilization. A physically based model was developed to predict the foam rheological parameters considering the interfacial rheological properties of the corresponding solutions.

1.2 Liquid foams

Liquid foams consist of concentrated gaseous bubbles dispersed in a continuous liquid phase. In contrast to bubbly liquids, the gas bubbles in liquid foams are densely packed and gas volume fractions are greater 63%, corresponding to the maximum volume fraction of randomly packed, equally sized spheres. The formation of foam involves an immense increase of interfacial area and overcoming the counteracting interfacial tension requires quite some energy. The physics of mechanical foaming techniques are elucidated in Chapter 1.2.2.

Foams are meta stable systems, subject to drainage when gravity separates gas and liquid due to their distinct densities, to coalescence of bubbles due to energetically favored reduction of the gas/liquid interface driven by the interfacial tension, and to coarsening because of gas diffusion from smaller to bigger bubbles driven by gas pressure differences. These mechanisms govern different time scales depending on the physiochemical properties of the liquid and gaseous phase. The phase density difference and the viscosity of the liquid phase set the drainage time. When bubbles approach, the presence of surface-active species in the liquid phase covering the interface decrease the coalescence rate by many orders of magnitude. And besides the solubility of the gaseous phase, these interfacial layers of surface-active species, serving as a barrier for gas diffusion, determine the coarsening rate. The foam structure, defined by its gas to liquid volume ratio and the bubble size distribution, is under constant change during foam aging as a result of the instability mechanisms but also affecting them itself. For instance, as broader the bubble size distribution as faster the foam coarsens, and as larger the gas volume fraction as lower is the drainage rate. The complex interplay between foam stability and its structure is addressed in Chapter 1.2.3.

The most remarkable attribute of foam is its rheology, which tremendously differs from those of the single liquid and gaseous phases. Even though the latter may be purely Newtonian fluids, the foams formed from these phases exhibit the characteristics of an elastic solid at low strains and of a viscous fluid once the strain surpassed a critical yield value. The origin of the foams' viscoelasticity lies in the enormous interfacial area. The interface is subject to interfacial tension and elastically stores energy when the foam and herby the bubbles' interfaces get deformed. Further insight on the rheological characteristics of foam is presented in Chapter 1.2.4.

1.2.1 Liquid foam applications

The perhaps first and most frequent experience we make with foam is when using soap, shampoo and cleaning detergents. The functionality of these products lies in solubilization of undesired

substances originally immiscible in water to ease their removal. This is provided by surface active agents (surfactants) possessing a hydrophilic moiety that renders its solubility in wash water and a hydrophobic moiety that adsorbs to the surface of nonpolar pollutant as grease, oil, or particles. The surfactants encapsulate the pollutant droplets or particles with the hydrophilic moieties forming a shell and making them miscible in rinsing water. Surfactants also reduce the interfacial tension of water and as a side effect ease the encapsulation of air bubbles onto whose nonpolar interface they adsorb likewise. This causes the formation of foam and even though the foamability of a cleaning agent is not related to its cleaning performance, the consumers' association between both determines the satisfactory cleaning perception (Cornwell, 2018). However, e.g. for shampoos and shaving creams the volume increase accompanying the foam formation and its viscoelasticity provides functionalities like spreadability and stiffness. Cleaning agents exhibit a longer dwell time when applied as a foam on vertical surfaces. Sagging is slowed down due to the yield stress of the foam.

Though gas bubbles do not provide any nutritional benefit and aerating food is often time and energy consumptive, foams are also appreciated in foods, as beverages, baked products, whipped diary and egg products, extruded and expanded cereals, chocolate and confectionary (Campbell and Mougeot, 1999). The popularity of aerated food is subordinately due to the flavor enhancing effect of the increased surface area, but primarily due to its distinct texture. Aerating bestows solids with softness or crispness and liquids with creaminess. Examples of prominent liquid food foams can be enjoyed on beer and cappuccino. In both cases, proteins adsorbing to the bubbles' interfaces and preventing them from coalescence are responsible for foam stabilization. Apart, from the pleasant consumers perception, the foam on beverages also damps sloshing from the glass or cup, due to wall friction. This affect could potentially be used to prevent instabilities caused by sloshing in liquid tanks in motion, such as in oil tank trucks or firefighting aircrafts (Sauret et al., 2015).

Foams are also used as fire-extinguishing agents itself and thrown over large conflagrations to suffocate them and to isolate the surrounding from heat. The foams are created at the place of incidence using a Venturi nozzle type device to incorporate air into water from local sources, previously blended with 1% to 6% of foaming concentrate. By this, the foaming solution volume is increased up to 1000-fold. Firefighting foaming concentrates are water-based solutions of sodium alkyl sulfate, fluorosurfactants, or proteins. (Blunk, 2018)

Foam fractionation and froth flotation are industrial foam applications that take advantage of the property of gas bubbles to concentrate hydrophobic species at their interfaces. This ability is used e.g. to separate valuable proteins from aqueous solutions, metal grains from metal sulfide or metal oxide ores, bitumen from oils sands, and organic pollutants from wastewater. The principle comprises sparging an aqueous solution or suspension with gas bubbles, adsorption of hydrophobic species to the bubbles interface, creaming of the bubbles due to buoyancy and harvesting of the foam. In froth flotation systems for separation of valuable mineral particles from gangue particles of the ore, this is realized in vessels with an air inlet at the bottom. The aqueous ore pulp, with particles previously ground to ideally 10 to 200 µm in size, and the air is mixed vigorously to prevent the mineral particles from sedimentation and to maximize the contact of bubbles with the particles. Because the wettability difference of the valuable minerals and the gangue is rarely sufficient for effective separation, flotation reagents need to be added to the pulp.

They are classified in collectors adsorbing to the mineral particles and enhancing their hydrophobicity, frothers lowering the interfacial tension for creation and stabilization of the frothlayer on the pulp, and modifiers altering the pH or the redox potential to increase the particle-collector interaction. (Sedev and Connor, 2018)

These exemplary applications of liquid foams underline the key role of the surface-active species to form foams that meet the particular application's requirement. The presence of amphiphilic substances stabilizing the bubbles interfaces is essential to create foam with a considerable lifetime.

1.2.2 Foaming techniques

The foam generation is accompanied by the creation of new gas/liquid interface which is counteracted by the interfacial tension σ. The creation of a bubble requires an energy input of at least $E=4\sigma R^2$ and hence, for typical bubble sizes R and interfacial tensions σ, foam generation is an energy consumptive process (Drenckhan and Saint-Jalmes, 2015). This energy can be applied physically, chemically or biologically. Physical foaming comprises mechanical foaming (e.g. bubbling, sparging, whipping, or shaking) and phase transition due to pressure release (e.g. in sparkling drinks, by extrusion, in shaving foam). Foams may be generated by chemical (e.g. with baking powder, polyurethane foaming) or electro-chemical reaction or biologically, e.g. with the aid of yeast. All foaming techniques comprise the formation of bubbles in a liquid followed by their spontaneous assembly and compaction due to gravity. An extensive description of foaming techniques is provided in a review article (Drenckhan and Saint-Jalmes, 2015). An excerpt, summarizing the mechanical foaming techniques used in this thesis, their underlying physics and typically achieved foam production rates and bubble sizes, is presented in the following:

Bubbling and sparging

The most simply described way to disperse bubbles into a liquid is by releasing air into a stationary liquid through a single orifice. If this happens slowly enough, at quasi-static conditions, interfacial stresses dominate over viscous and inertial stresses. Hence, the capillary number $Ca=\eta U/\sigma$, giving the ratio between viscous and interfacial stress with the fluid viscosity η and velocity U, and the Weber number $We=\rho U^2 L/\sigma$, presenting the ratio between inertial and interfacial stress with the fluid density ρ and a characteristic length L, are $<<1$. The pressure difference between liquid and gas that needs to be applied in order to press the gas through an orifice with radius R_0 scales linearly with the interfacial tension σ, as suggested by the Young-Laplace law (de Gennes et al., 2013)

$$\Delta p=2\sigma/R. \tag{1.1}$$

It reaches a maximum when the bubbles interface is maximal curved as it is the case at the point when the gas forms a hemisphere with radius $R=R_0$ at the orifice outlet. When the maximum pressures is exceeded, the bubble grows spontaneously, decreasing its Laplace pressure, and eventually detaches from the orifice when the buoyancy force of the approximately spherical bubble $F_b=\Delta\rho g(4/3\pi)R^3$ (with $\Delta\rho$ being the difference between the densities of liquid and gas) exceeds the surface tension force $F_\sigma=2\pi\sigma R_0$. From $F_b=F_\sigma$. The radius of the detaching bubble R can be approximated as

$$R\sim(\sigma/\Delta\rho g)^{2/3}R_0^{1/3}=Bo^{-1/3}R_0 \qquad \text{for } Ca \text{ and } We<1 \qquad (1.2)$$

where the Bond number $Bo=\Delta\rho gL^2/\sigma$, stands for the ratio between gravitational and interfacial stress. It depends on the characteristic length scale $L=R_0$. The foams produced using this "dripping bubble" method are highly monodisperse with typical bubble sizes between a few hundred micrometers and a few millimeters but the production is restricted to a few bubbles per second.

If the gas flow Q_g is increased in the same setup, viscous drag force exerted by the liquid onto the gas bubble and inertial forces of the gas and the liquid need to be considered. The viscous drag retards the bubble detachment from the orifice and the bubbles become larger. Neglecting the surface tension and inertia forces following approximation for the bubble size R was found:

$$R\sim(\eta Q_g/(\Delta\rho g))^{1/4}\sim(Ca/Bo)^{1/4}R_0 \qquad \text{for } Ca>>1 \text{ and } We<1. \qquad (1.3)$$

When Q_g is further increased inertia forces cannot be neglected and with increasing ratio between inertial and interfacial stress given by the Weber number $We=\rho U^2L/\sigma$, with the characteristic length $L=R_0$, the gas bubble forming at the orifice outlet gets elongated. At sufficiently high We, the bubble formation is entirely due break-up of the emerging gas jet caused by Rayleigh-Plateau instability. In that case, interfacial and viscous forces can be neglected leading to

$$R\sim Q_g^{2/5}/g^{1/5}\sim(We/Bo)^{1/5}R_0 \qquad \text{for } Ca>>1 \text{ and } We>>1. \qquad (1.4)$$

The final bubble size is proportional to the gas jet radius and in the order of that radius, but somewhat larger. However, the gas jet does not necessarily break into bubbles of equal size, as small "satellite" bubbles may form during the rupture.

In most cases the system is operated in between the limiting cases of a dripping bubble and jet break-up and interfacial, inertia, gravity and viscous forces apply simultaneously. A more complex model for the bubble size is proposed by Jamialahmadi et al. (Jamialahmadi et al., 2001):

$$R=[5/Bo+9.261(We/Bo)^{0.18}/Ga^{0.39}+2.14(We/Bo)^{0.251}]^{1/3}R_0 \qquad (1.5)$$

where the Galilei number $Ga=g\rho^2L^3/\eta^2$ comprises the characteristic length $L=R_0$.

The bubble detachment from the orifice changes when the surrounding liquid is flowing, either in co-flow or crossflow, and creates additional inertial and viscous forces. The influence of the liquid flow is even enhanced in confined condition as it is the case in microfluidic channels. As the gravity is neglectable in such small geometries ($Bo<<1$), the bubble detachment from the orifice occurs only when the capillary force is exceeded by the viscous drag of the surrounding fluid.

The viscous drag is given by an approximation of the Stokes force $F_V=6\pi R\eta_l U_l$, with the bubble radius R and the viscosity η_l and flow velocity U_l of the surrounding liquid, and $F_V= F_\sigma$ yields

$$R\sim\sigma/(\eta_l U_l)\ R_0 = R_0/Ca_l \qquad \text{for } Bo<1 \qquad (1.6)$$

with Capillary number of the liquid Ca_l. As for bubbling into stationary liquid, there is a transition from the dripping bubble case to the emergence of a gas jet at the orifice outlet when bubbling into a flowing liquid. This transition occurs when viscous forces dominate over interfacial tension forces at a well-defined critical Capillary number of the liquid Ca_l in confined geometries. The transition strongly depends on the density and viscosity ratio of the gas and surrounding liquid. At low Reynolds number $Re=\rho LU/\eta$, giving the ratio between inertial and viscous stress, We increases proportional with Re and the transition occurs at a fixed Capillary number $Ca=We/Re$. In the jetting regime, the length of the jet before the gas ligament breaks up into bubbles depends on the flow velocities of gas and liquid. If inertial forces of the gas dominate the jetting, the gas jet is decelerated by the surrounding liquid and widens with increasing distance from the orifice, which leads to bubbles with radii larger than R_0. In the extreme case Eq.1.4 applies. If the flow of the surrounding liquid dominates the jetting, the gas is accelerated and the jet narrows with increasing distance from the orifice, leading to bubbles with radii smaller than R_0. In this case the bubble radius scales with the ratio between the flow rate of the gas Q_g and the surrounding liquid Q_l

$$R\sim (Q_g/Q_l)^{2ß}\ R_0 \qquad (1.7)$$

with a pre-factor and power $ß$ depending on the microfluidic geometry and the ratio between the gas and liquid viscosities. This way, the bubble size can be tuned down to a few micrometers by creating thin gas jets. However, the foam production rate in microfluidic devices are below 0.1 l/min and beyond technical relevance.

In most applications foaming occurs through many orifices in parallel, e.g. when bubbling through a perforated plate with regularly distributed, equal holes or sparging through a porous disc with irregularly distributed pores with a characteristic size distribution. The latter applies for the foaming apparatus used in the studies described in Chapter 4 and 5. Hydrodynamic coupling between holes within a critical spatial range and the coupling through fluctuations in the pressure and flow field of the gas on the other side of the plate add complexity to the bubbling processes described above. For example, the orifice with the biggest radius releases a bubble at lowest pressure and the resulting pressure drop in the gas reservoir prevents the bubbling from smaller orifices. Hence, at low pressure corresponding to low gas flow rates highly monodisperse foams can be produced. With increasing pressure, bubbles are also released from smaller orifices and the foam becomes polydisperse. The pressure fluctuations can be reduced by increasing the orifice length or placing a fine porous medium below the perforated disk. Using such perforated or porous discs, bubbles with sizes typically ranging from a few hundred micrometers to one millimeter can be produced and the size distribution ranges from monodisperse to 50% polydispersity depending on conditions as flow rate, liquid properties and orifice geometry and spacing. The average bubble size is in general proportional to the average pore size of the sparger disc. The foam production rate is around 1 l/min per cm^2 disk area.

Plunging and whipping - gas entrainment at free surfaces and bubble break-up under shear

Another method to incorporate gas into a liquid and create bubbles is by gas entrainment at free surfaces due to perturbation of the interface followed by bubble break-up under shear. This commonly requires abrupt changes of fluid velocities or geometrical constraints and is well known from foam generation by ocean weaves or a plunging water jet into the bathtub. The plunging jet is also used as a standardized foamability test, called the Ross-Miles test, comparing foam column heights produced from 200 ml solution that plunged a height of 90 cm from a funnel onto the surface of a volume of 50 ml of the same solution. The liquid jet creates an opening like a cone at its impact region on the liquid surface and the cone tip curvature r depends on the capillary number $Ca=\eta U/\sigma$, with the jet velocity U, i.e. $r\sim\exp(-Ca)$. At a critical cone tip curvature r_c, corresponding to a critical capillary number which scales logarithmically with the viscosity ratio of gas and liquid $Ca_{crit}\sim-\ln(\eta_g/\eta_l)$, the cone tip is increasingly stretched and breaks into smaller bubbles. The rate of gas entrainment, however, depends only on the gas viscosity, as the gas film separates the jet from the rest of the fluid. Typical foam production rates are in the order of 1 l/min and bubble sizes vary between a few hundred micrometers and a few millimeters, with polydispersity increasing with jet velocity. In plunging jets of low viscosity high Reynolds numbers $Re>100$ and low capillary numbers $Ca<1$ apply. Under such conditions, inertial instabilities, as the Kelvin-Helmholtz instability, occurring when two immiscible fluids with different densities flow aside with a strong velocity difference, alter the jet cross-section before its impact. The fluctuations in the jet cross section change the gas entrainment and can even lead to another type of entrainment at high Weber numbers $We=ReCa$. The jet breaks up into smaller ligaments which in turn break up into droplets and this can lead to entrainment of significant amount of gas, as demonstrated by breaking waves.

Many foaming devices are designed to entrain air and subsequently break up bubbles in order to obtain foams with desired bubble size and gas volume fraction. Blenders, as the one described in Chapter 3, are commonly used to produce foams and combine air entrainment and bubble break-up under active shear. A bubble exposed to a simple shear flow is deformed into ab elongated steady shape whose aspect ratio depends on the Capillary number Ca of the surrounding liquid flow. The aspect ratio increases with increasing Ca and fluid viscosity until a critical deformation γ_{crit} is reached, corresponding to a critical capillary number Ca_{crit}. Beyond this deformation, Rayleigh-Plateau instabilities, cause the break-up of the elongated bubble into smaller bubbles with sizes in the order of the radius of the bubble thread at γ_{crit}. The critical capillary pressure decreases with increasing viscosity ratio of gas and liquid η_g/η_l, and $Ca_{crit}\approx3$ for a bubble in water. Because the critical capillary pressure is associated with γ_{crit}, the size of bubbles after the shear induced break-up decreases with decreasing η_g/η_l. The critical capillary number varies with η_g/η_l depending on the type of flow (elongational, rotational, shear) as it can lead to entirely different shapes of the deformed bubble. For small viscosity ratios η_g/η_l, the critical capillary number decreases from pure shear flow to purely extensional flow, hence resulting bubble size increases. Besides bubble break-up due to Rayleigh-Plateau instability, other phenomena, called “tip-streaming” and “end-pinching”, cause bubble break-up far below the critical capillary number. Tip-streaming describes the creation of very small bubbles at the tip of an elongated bigger bubbles in shear flow and is promoted by presence of surfactants reducing the interfacial tension. End-pinching occurs when the flow around an elongated bubble is suddenly stopped or the

capillary number of the flowing liquid decreases. The extended bubble tends to restore its spherical shape, but when its contracts, the ends of the extended bubble rip off. This may repeat several times at the ends of the remaining extended bubble, respectively, resulting in a string of bubbles. In a blender, liquid and gas are drastically heterogeneously sheared and liquid fraction and average bubble size decrease gradually over time until an equilibrium state is reached. The final foam structure depends on the rheology of the liquid and the rotating speed of the blender and the bubble size ranges between tens of micrometers and one millimeter. The foam production rate is about 1 l/min, but further bubble break-up until the equilibrium bubble size is reached may take longer. To overcome the scale-up limits of the batch process various rotor-stator mixers have been developed. Gas and liquid are pressed continuously through a set of narrowly spaced static and rotating parts and, at high shear rates, bubbles sizes of a few micrometers can be produced.

Shaking

Shaking a container filled with gas and liquid is a very simple way to produce foams and was used for foam stability comparisons in the study presented in Chapter 4. But it involves all mechanical processes discussed above which makes it difficult to describe quantitatively. It is also used in the "Bartsch test", performing controlled flips of a cell at controlled frequency, that provides a qualitative estimation of the foamability of solutions. In a simpler experiment, 2D foams are generated in a flat cell, then the average bubble size decreases with the number of flips and the bubble size distribution saturates with a Gamma distribution. The average bubble size depends on the gas to liquid volume ratio in the cell and is linked to the capillary length.

1.2.3 Structure and stability

The geometrical structure of foams is of particular interest as it determines many properties, as the scattering of light and sound, foam drainage, their electrical conductivity, their elasticity and flow behavior. The structure of foams is determined by the ratio between gas and liquid and the size distribution of the dispersed gas bubbles and is subject to temporal instability mechanisms (drainage, coarsening, coalescence). Foams subject to gravitational forces drain, i.e. the liquid phase separates from the foam, until a quasi-equilibrium state is reached when the gravitational force pulling the liquid face downwards, the buoyancy force pulling the bubbles upwards, and the capillary forces pulling the liquid into bubbles' interstices are balanced. The equilibrium is restricted to time scales short enough to allow diffusive gas transfer between bubbles (coarsening) and liquid film rupture (coalescence) to be neglected. The bubbles are considered incompressible, because the bubbles' excess pressure given by Young-Laplace law (see Eq.1.1) is two orders of magnitude smaller than the atmospheric pressure. The equilibrium foam structure at a given gas volume fraction is defined by minimization of the interfacial energy $E=\sigma S$, which scales linearly with the total interfacial area S in a foam at a constant interfacial tension σ.

Unlike in emulsion, the differences between phase densities, bubble sizes and interfacial tension are high in foams such that the surface energy and also the potential energy due to buoyancy $\Delta\rho g R^4$ is far higher than the neglectable thermal energy $k_B T$. Hence, the bubbles are trapped in local energy minima and topological changes which would reduce the global energy do not happen spontaneously because of too high energy barriers. Energetically, lower states can, however, be obtained with mechanical shearing, coarsening or by injection of foaming solution and therefor the bubble packing strongly depends on the foaming technique. (Drenckhan and Hutzler, 2015)

Gas volume fraction

The bubbles' shape depends on the local gas volume fraction of the foam

$$\varphi = n\, 4/3\pi \langle R^3 \rangle \qquad (1.8)$$

with the number of bubbles per unit volume n, and it decreases in the direction of gravity. At the bottom of a foam column the bubbles are undeformed spheres, as displayed in Fig.1.1A. The maximum packing fraction of randomly close packed spherical bubbles with moderate polydispersity is ≈0.635. This corresponds to a critical gas volume fraction φ_c. At higher gas volume fraction φ, the bubbles deform and curved liquid films (lamellae) separating the bubbles form. Plateau's laws describe that always three lamellae meet at 120° angle along an edge (Plateau border) and always four of those edges meet at tetrahedral angle at a vertex, as illustrated in Fig.1.1B. These local structures result from minimization of interfacial area in dry foams with $\varphi > 0.95$, but deviations may occur in wet foams with $0.63 < \varphi < 0.85$. The transition in foam structure along the direction of gravity follows the gas volume fraction from wet foam at the bottom of the foam column to dry foam at the foam's top. The height of wet foam, i.e. with $\varphi < 0.85$, at the bottom of the foam column is $\approx l_c^2/d$, with the bubble diameter d and the liquid's capillary length

$$l_c = (\sigma/\Delta\rho g)^{1/2} . \qquad (1.9)$$

(Drenckhan and Hutzler, 2015).

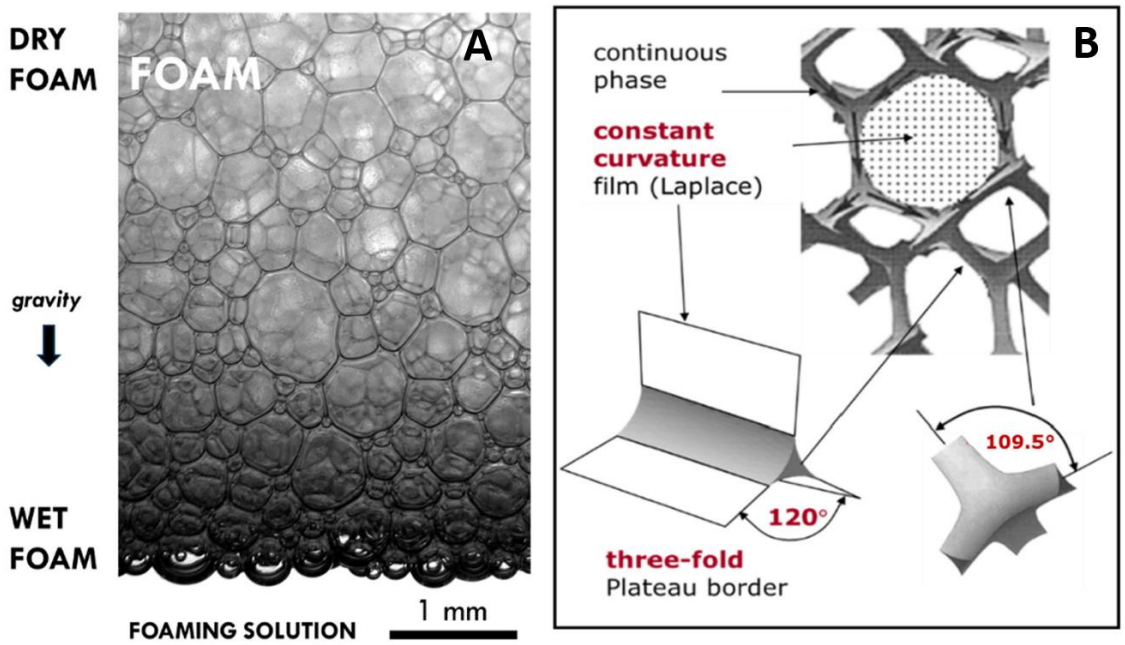

Figure 1.1: (A) Gradient of liquid fraction in a liquid foam subject to drainage under gravity causes transition of bubbles´ shape from spherical at the foam bottom to polyhedral in the dry limit at the foam´s top. (B) Plateau's laws, applying for dry foams with φ>0.95, describe that always three lamellae meet at 120° angle along an edge (Plateau border) and always four of those edges meet at tetrahedral angle at a vertex. (Drenckhan and Hutzler, 2015)

As mentioned above, the gas volume fraction in freely draining foams is subject to temporal changes driven by the gravitational force $F_g=gm$ and the buoyancy $F_b=\rho g\ 4/3\pi R^3$, separating gas bubbles from the surrounding liquid, and the counteracting capillary force, which resists the bubble deformation by retaining the liquid in the bubbles' interstices. The force that must be applied per unit area of a membrane, only permeable for liquid and being pressed onto a foam to achieve a certain gas volume fraction, was measured and established as osmotic pressure Π by Princen et al. (Princen and Kiss, 1987):

$$\Pi=\sigma\varphi^2\ \mathrm{d}(S/V)/\mathrm{d}\varphi \qquad (1.10)$$

where S/V is the interfacial area per unit volume of foam. In experiments and simulations (see Fig.1.2A), a semiempirical expression for the osmotic pressure as a function of φ was found

$$\Pi=k\ \sigma/\mathrm{R}\ (\varphi-\varphi_c)^{\beta}/(1-\varphi)^{1/2} \qquad (1.11)$$

with $k\approx3.5$, $\beta\approx2.5$, and $\varphi_c=0.63$ (Princen and Kiss, 1987). The drainage equilibrium is reached, when the osmotic pressure and the buoyancy over any vertical distance in the foam dh are equal, $\mathrm{d}\Pi=\varphi(h)\Delta\rho g\ \mathrm{d}h$. This determines the equilibrium liquid distribution as a function of vertical position in the foam (Drenckhan and Hutzler, 2015):

$$\varphi_l(h)=1-\varphi(h)=(1-\varphi_c)/(1+\ h\ R_{32}/l_c^2)^2. \qquad (1.12)$$

Fig.1.2B shows that equilibrium liquid fractions obtained for emulsions and foams collapse onto a master curve when plotted versus the height normalized by l_c^2 and the reciprocal bubble or droplet Sauter radius $R_{32}=\langle R^3\rangle/\langle R^2\rangle$.

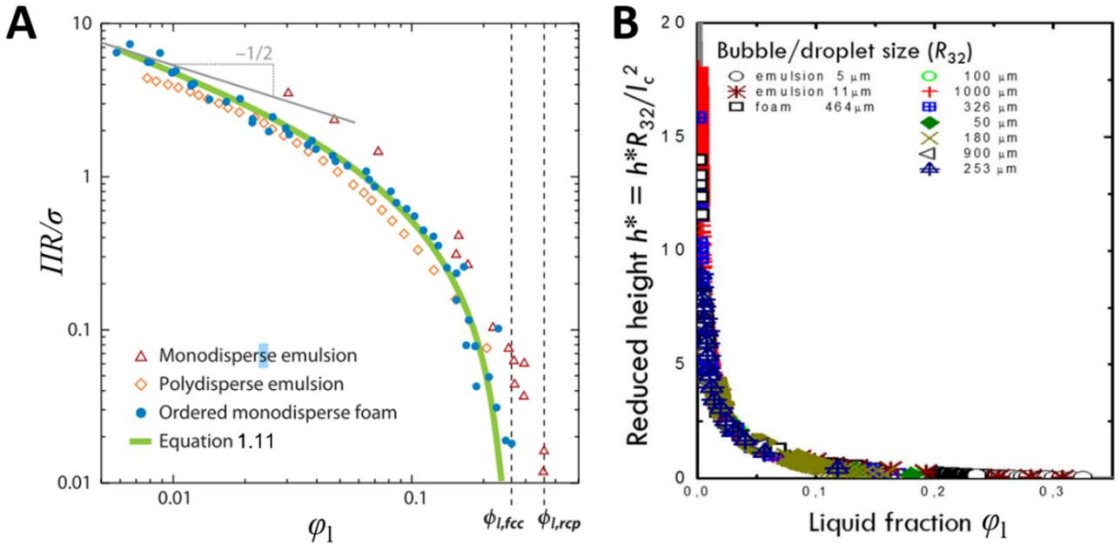

Figure 1.2: (A) Osmotic pressure normalized by σ/R versus liquid volume fraction φ_l of foams and emulsions. Green line corresponds to Eq.1.11. In the limit of dry foams, $\Pi\approx 0.6\sigma/(R(1-\varphi)^{1/2})$. The liquid fraction in face-centered cubic structures $\varphi_{l,fcc}$ and random closed packed spheres $\varphi_{l,rcp}$ are marked with dashed lines. (Cohen-Addad et al., 2013) (B) Liquid fraction profiles of foams and emulsions with various bubble or droplet sizes versus the foam/emulsion height normalized by the characteristic length l_c^2/R_{32}. (Drenckhan and Hutzler, 2015)

Drainage

Before an equilibrium liquid distribution throughout the foam is reached, the spatial liquid fraction gradient is subject to temporal changes. During drainage, different liquid fraction profiles emerge along the vertical axis in a foam depending on the type of foam drainage, as shown in Fig.1.3, i.e. free drainage describing the spontaneous evolution from a wet foam to the equilibrium state, forced drainage applicable to a dry foam continuously flooded with liquid from its top, and pulsed drainage corresponding to a finite amount of liquid that propagates through a dry foam. The liquid flow rate per unit area of foam is described by Darcy's law:

$$Q/S=K(\rho g-\mathrm{d}p/\mathrm{d}h)/\eta, \qquad (1.13)$$

with a cross-section area S perfused by a constant liquid flow Q and $\mathrm{d}p/\mathrm{d}h$ is the capillary pressure gradient. The forced drainage experiment, with constant flow conditions throughout the wet region of the foam, i.e. $\mathrm{d}p/\mathrm{d}h=0$, provides an experimental setup to determine the foam permeability $K=\eta Q/(S\rho g)$, with the liquid's viscosity η and density ρ (Cohen-Addad et al., 2013).

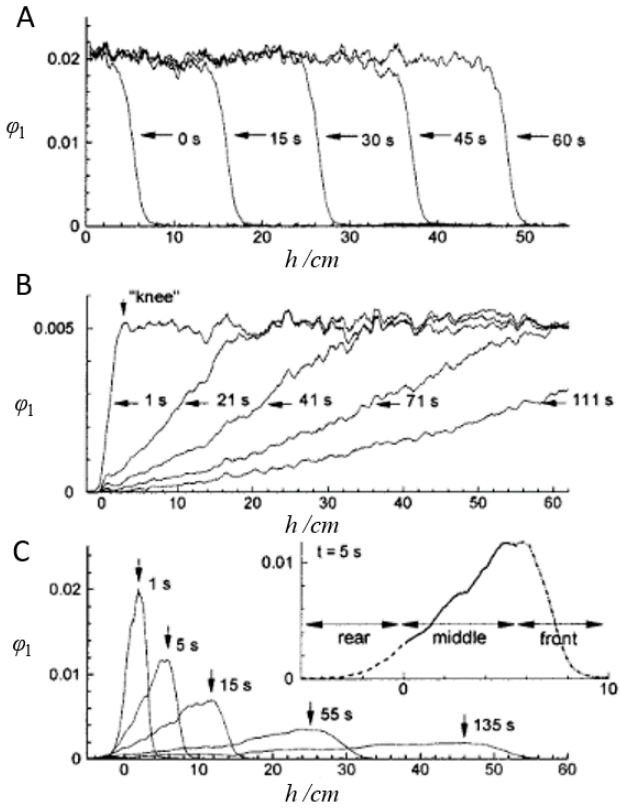

Figure 1.3: Liquid fraction profile of foams subject to (A) forced drainage, (B) free drainage, and (C) pulsed drainage. Profiles are labeled with the foam age. h=0 corresponds to the foam top. (Koehler et al., 2000)

For Plateau borders, whose cross sections are concave triangles with curvature $1/R_{Pb}$, a capillary pressure $P_c=\sigma/R_{Pb}$ can be derived from Young-Laplace's equation (see Eq.1.1). When φ>0.97, the cross sectional area of a Plateau border is $S=(3^{1/2}-\pi/2)R_{Pb}^2$and $R_{Pb}=R((1-\varphi)/C)^{1/2}$ with the geometrical constant C (≈0.333 for monodisperse ordered foams) (Cohen-Addad et al., 2013). As the curvature $1/R_{Pb}$ is larger than the curvature of the lamellae, the emerging pressure difference causes liquid to flow from the lamellae into the Plateau borders. The liquid then drains through the Plateau borders due to gravity. For relatively dry foams, following one-dimensional form of the drainage equation describes the spatial and temporal changes of liquid volume fraction in a foam, with the assumption that the fluid travels exclusively through Plateau borders and vertices and liquid flow through lamellae can be neglected:

$$d\varphi_l/dt + d/dh(K\rho g/\eta) - d/dh(\sigma K \varphi_l^{-3/2}/(2cR\eta)\, d/dh(\varphi_l)) = 0. \quad (1.14)$$

The permeability $K\sim R^2\varphi_l^{3/2}$ for the limiting case of the fluid exhibiting plug flow with free slip at the boundary of the Plateau borders, corresponding to mobile interfaces (also see Chapter 1.3.2), and flow resistance is only due to shear flow in the vertices. For no-slip conditions at the boundary of the Plateau-border, corresponding to rigid interfaces, the fluid exhibits Poiseuille flow and $K=S\, k_{Pb}\, \varphi_l/3 = 0.0032\, R^2\, \varphi_l^2$, with the dimensionless Plateau-border permeability k_{Pb}=0.02. However, in reality, the boundary conditions lie in between these two limiting cases and $1/K=1/K_{mobile}+1/K_{rigid}$. (Cohen-Addad et al., 2013)

At a fixed position in the foam h, the drainage equation predicts the power law behavior $\varphi_l \sim t^{-k}$ with k varying between 2/3 for rigid interfaces and 1 for mobile interfaces, as also found in free drainage experiments of foam with mobile interfaces, displayed in Fig.1.4A (Koehler et al., 2000). Fig.1.4B shows that at fixed times, the solution of the drainage equation for free drainage boundary conditions predicts the liquid fraction, which corresponds to the cross-section area of the Plateau borders, to increase linearly within a downward vertical distance in the foam with the slope decreasing with time (Verbist et al., 1996). This agrees with the experimental data.

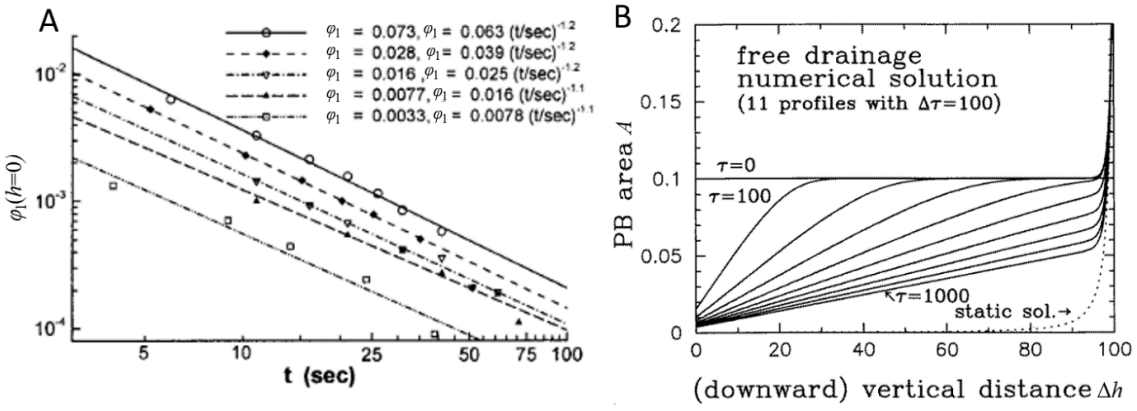

Figure 1.4: (A) Liquid volume fraction versus foam age at the foam top h=0 for five free drainage profiles, with initial average liquid fraction φ_l=0.0033, ..., 0.073. The lines show the best fit to the power-law behavior $\varphi_l \sim t^{-k}$. (Koehler et al., 2000) (B) Numerical solution of the drainage equation for free drainage boundary conditions, giving the Plateau border cross sectional area, corresponding to the foam liquid fraction, versus the height in the foam. (Verbist et al., 1996)

The Boussinesq number $Bq=\eta_{interface}/(\eta R_{Pb})$, with the interfacial viscosity $\eta_{interface}$, characterizes the influence of the interfacial mobility on the flow through the Plateau borders. Large Bq corresponds to rigid interfaces causing the velocity profile of a Poiseuille flow, as illustrated in Fig.1.5A. Fig.1.5B shows the decrease of the Plateau border permeability k_{Pb} with increasing Boussinesq number Bq. For small Bq, the interface travels with the velocity of the bulk and, except for the three corner regions of the cross section of the Plateau border at which the fluid is pinned, plug flow emerges. The Plateau border permeability k_{Pb} increased linearly with decreasing Bq, for $0.01<Bq<1$. (Cohen-Addad et al., 2013)

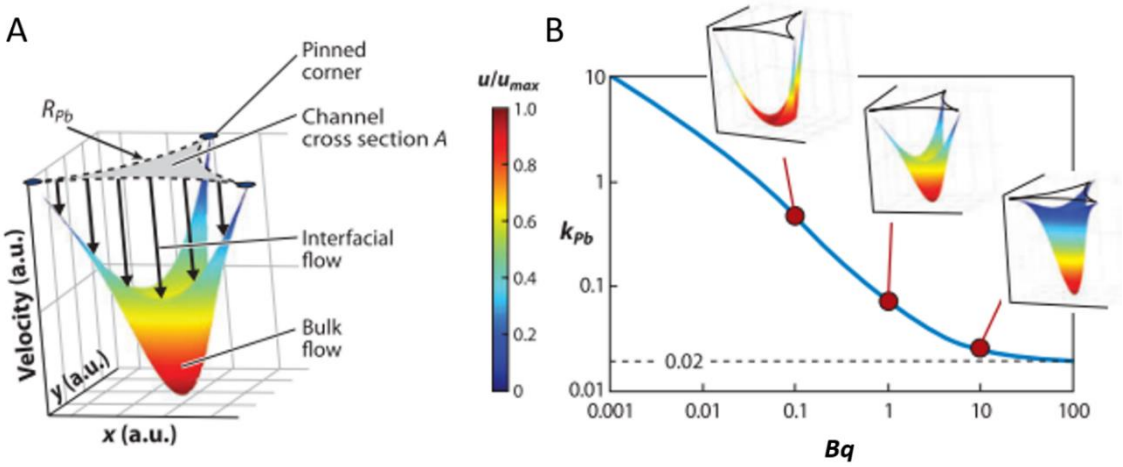

Figure 1.5: (A) Liquid velocity field in an infinitely long Plateau border of radius R_{Pb}. (B) Dimensionless channel permeability k_{Pb} versus Boussinesq number. At the limit of rigid interfaces, corresponding to large Bq, k_{Pb}=0.02. At low Bq, k_{Pb} increases due to surface shear flow. The evolution is illustrated by the three surface plots for Bq = 0.1, 1, and 10. (Cohen-Addad et al., 2013)

Gas volume fraction determination

The gas volume fraction in foams is experimentally accessible by various techniques, i.e. measuring the depth of immersion of a foam column in a liquid, estimating local liquid fraction from the Plateau borders on photographs of foam, measuring the electrical conductivity, or X-ray scattering.

The most commonly used technique is to measure the electrical conductivity of the foam and calculate the gas volume fraction using a semi-empirical correlation with the ratio between foam and solution conductivity κ established and probed for many different foaming solutions by Feitosa et al. (Feitosa et al., 2005a):

$$\varphi=1-(3\kappa+33\kappa)/(1+25\kappa+10\kappa^2). \quad (1.15)$$

This provides a reliable extension of the linear relationship $\varphi=3\kappa$, valid in the dry limit (Weaire and Hutzler, 1999), to lower gas volume fractions.

Bubble size distribution

Monodisperse, periodic foams

In 1887, Kelvin found a structure to divide space in cells of equal volume and shape (truncated octahedron) with minimized cell surface area that can be experimentally generated by draining a hexagonal-close packing of spherical bubbles. In the Kelvin structure each bubble has 14 neighboring bubbles arranged in a body-centered cubic (BCC) packing. Only over 100 years later in 1994, Weaire and Phelan computed a structure with 0.3% less surface area. It consists of two different cell shapes with equal volume packed in a BCC structure with an average of 13.5 neighboring bubbles.

But it took until 2012 to create a foam obtaining the Weaire-Phelan structure, as it cannot be formed in a container with flat walls. For monodisperse disordered foams, simulations predict the average number of neighboring bubbles to be 13.7, which is close to that in the ordered structures discussed above.

The BCC structures emerge in monodisperse dry foams with φ>0.95 obeying Plateau's laws. In wet foams, i.e. at φ around the critical volume fraction φ_c=0.635 for random close packed (RCP) monodisperse foams, bubbles are approximately spherical. An average of 6 nearest neighbors, as found for random packing of frictionless spheres, is reasonable, even not yet evidenced for foams. In wet foams, the buoyancy force acting on a bubble is neglectable compared to the surface tension which prevents bubble deformation, such that the bubbles may be considered as hard spheres. Minimization of the potential energy of the bubbles, due to buoyancy, favors packing of minimal density. Therefore, wet monodisperse foams crystallize spontaneously into face-centered cubic (FCC) or hexagonally close packed (HCP) structures yielding 12 nearest neighbors per bubble. The bubble volume fraction is 0.7405 for bubbles in FCC and HCP lattices. Regardless of the foaming technique, monodisperse spherical bubbles, even previously randomly close packed, reorganize into FCC and HCP structures, with FCC favored, as it is mechanically more stable. However, the crystallization may take several days.

Fig.1.6 shows a transition from the FCC (right photograph inset) to BCC (left photograph inset) structure in monodisperse ordered foams that occurs with increasing gas volume fraction, e.g. due to foam drainage, and vice versa. Fig.1.6 also displays the surface excess for both structures $\varepsilon(\varphi)=(S(\varphi)-S_0)/S_0$, with the bubble surface area S and the undeformed spherical bubble surface S_0, versus the gas volume fraction for both structures. The transition point from predominantly FCC structure with eightfold vertices to BCC structure with four-fold vertices occurs at $\varphi_I\approx0.063$, predicted from the cross-over. In periodic foam structures, the relative surface excess scales linearly with the number of neighboring bubbles N:

$$\varepsilon(\varphi)\sim N(\varphi-\varphi_c)^2/(18\varphi_c^2\ln(\varphi-\varphi_c)). \quad (1.16)$$

The number of neighbors increase from 6 at φ_c with increasing gas volume fraction following a power law $(N-6)\sim(\varphi-\varphi_c)^{1/2}$. (Drenckhan and Hutzler, 2015)

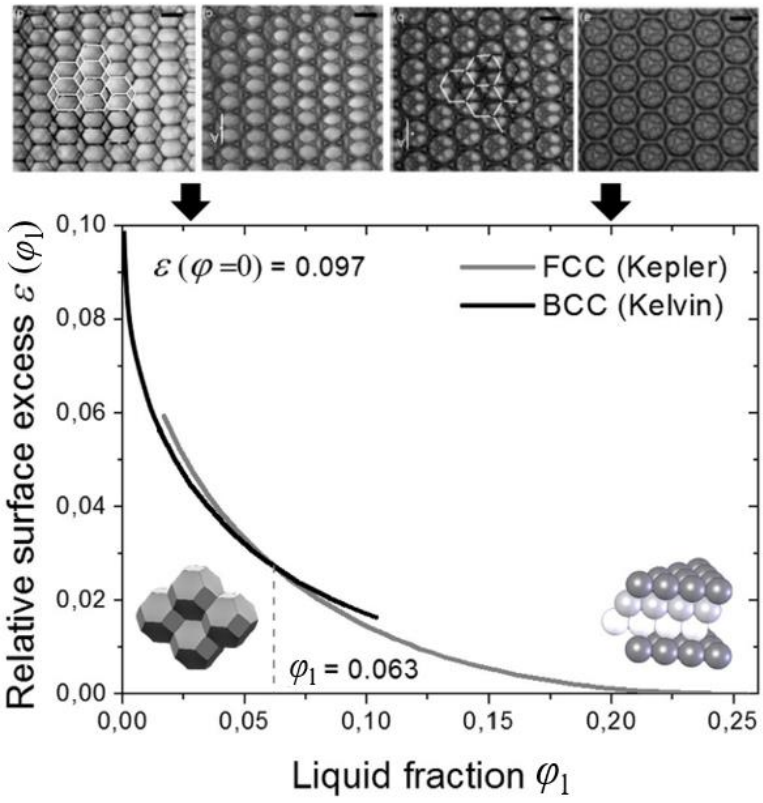

Figure 1.6: Relative surface access $\varepsilon(\varphi)$ (Eq.1.16) of dry foams with FCC structure and wet foams with BCC structure versus their liquid fraction. The cross-over between the functions mark the transition point at $\varphi_l \approx 0.063$. The insets show photographs of foam undergoing the transition from BCC to FCC structure from left to right. (Drenckhan and Hutzler, 2015)

Polydisperse disordered foams

In contrast to ordered foams derived from precisely set experimental conditions, real foams generally consist of disordered bubble packings with polydispersity depending on the foaming technique (see also Chapter 1.2.2). The average bubble size in a polydisperse bubble distribution is characterized by the Sauter mean radius $R_{32}=\langle R^3\rangle/\langle R^2\rangle$, where the equivalent sphere radius $R=(3/(4\pi)V)^{1/3}$ is given by the bubbles' volume and $\langle\ \rangle$ is the arithmetic mean. The polydispersity parameter

$$p_{32}=R_{32}/\langle R^3\rangle^{1/3}-1 \qquad (1.17)$$

was introduced by Kraynik et.al (Kraynik et al., 2004).

Increasing polydispersity results in a broadening of the probability distribution of the neighboring bubbles number N, corresponding to the facets of a bubble in dry foam, and a decrease of the average of N, as shown in Fig.1.7A and B. Note, that locally, structures emerge that deviate from the randomness of the packing.

It is statistically favored that the number of neighbors increases with the size of the bubble and that large bubbles are surrounded by smaller ones, which results in the correlation illustrated in Fig.1.7C. The surface energy in a foam decreases with increasing polydispersity, as shown in Fig.1.7D. (Drenckhan and Hutzler, 2015)

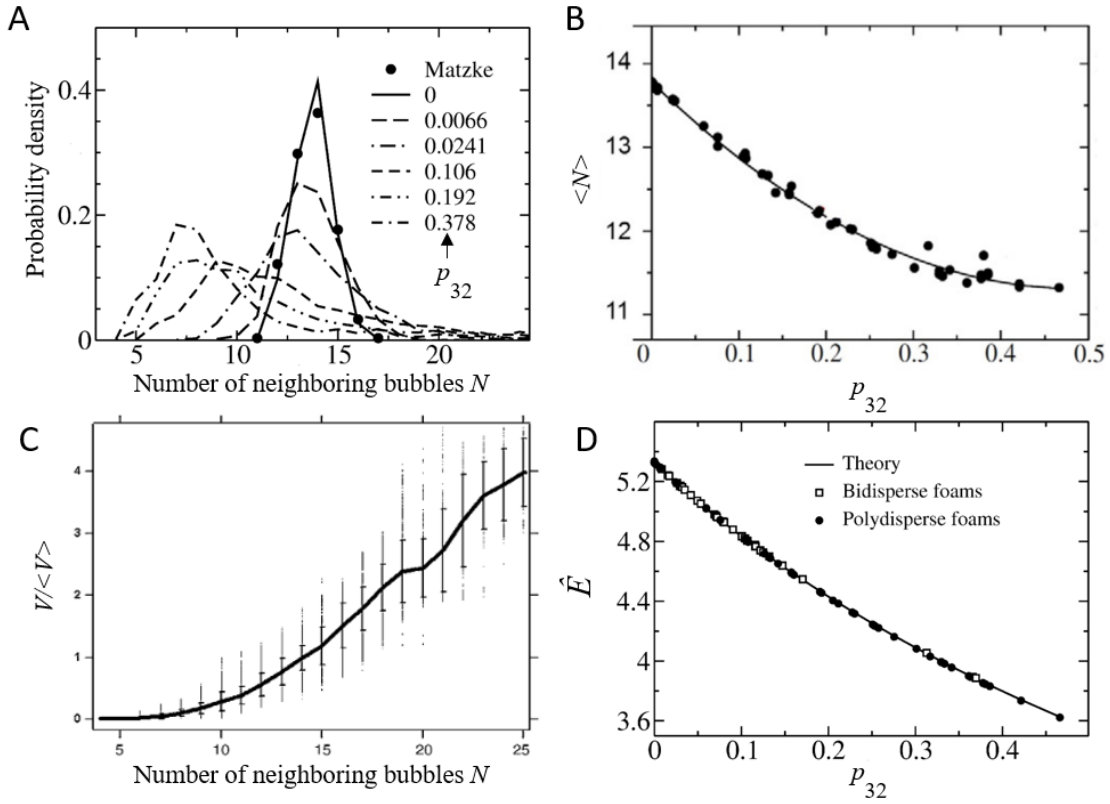

Figure 1.7: (A) Probability distribution of the number of bubbles with N neighbors in foam simulations for different polydispersities p_{32}, defined in Eq.1.17 (adapted from (Kraynik et al., 2004)). Data points show experimental data available for monodisperse disordered foams, taken by Matzke (Matzke, 1946). (B) Average number of neighboring bubbles N versus polydispersity p_{32}. Solid line is a quadratic fit to the data obtained from foam simulations (adapted from (Kraynik, 2006)). (C) Bubble volume normalized by the average bubble volume from simulations of polydisperse foam as a function of the number of neighbors N (adapted from (Drenckhan and Hutzler, 2015; Jurine et al., 2005). (D) Scaled energy $\hat{E}=E/(\sigma/\langle V^{1/3}\rangle)$ versus polydispersity p_{32} from simulations for polydisperse and bidisperse foams. The solid line is given by $\hat{E}=5.32/(1+p_{32})$ (adapted from (Kraynik, 2006)).

Surprisingly, the interfacial area to volume ratio of bubbles in a dry foam is independent of their number of neighbors, in contrast to polyhedra with flat facets, as shown in Fig.1.8. The bubbles interfacial area is always about 10% bigger than for a sphere with the same volume. The normalized surface area $S/\langle V\rangle^{2/3}$ characterizes the deviation of the bubbles shape from a sphere and is approximately 5.23. This leads to the simple theory that the surface energy in a foam is

$$\hat{E}=E/\langle V\rangle^{2/3}=\sigma S/\langle V\rangle^{2/3}=5.23/(1+p_{32})\ \sigma/\langle V\rangle^{1/3} \qquad (1.18)$$

which is in good agreement with simulation data shown in Fig.1.7D.

Hence, for a known bubble size distribution and p_{32}, the foams' interfacial area can be calculated. (Kraynik, 2006)
This is of particular interest for understanding the diffusive coarsening process.

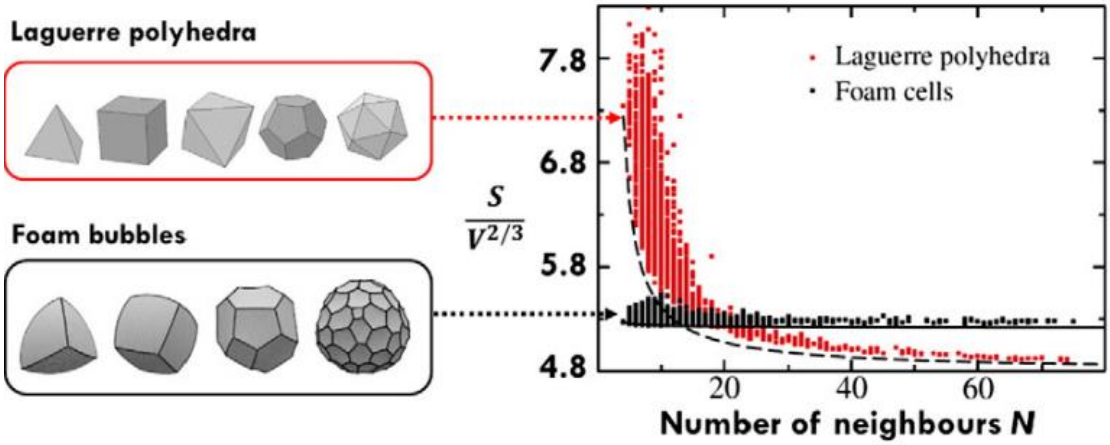

Figure 1.8: Normalized surface area S for all bubbles and Laguerre polyhedral normalized by their volume $V^{2/3}$ from simulation of their corresponding packings versus the number of neighbors N, respectively. The normalized surface area of bubbles exhibits a constant value of 5.32±0.04, because they adjust their shape in close packing. (Drenckhan and Hutzler, 2015; Kraynik, 2006)

Coarsening

In polydisperse foams, diffusive gas transport through the lamellae from smaller into larger bubbles causes the foam structure to coarsen, i.e. the average bubble size and the polydispersity increase. This coarsening process is also known as disproportionation and in case of isolated bubbles related to "Ostwald ripening" of granular matter. The gas transport is driven by the Laplace pressure difference between bubbles with different interfacial curvatures, which can be approximated by the bubbles' radii R: $\Delta p=\sigma/\Delta R$ (see Eq.1.1).

The dimensionless diffusive growth rate of a bubble with a given volume V is

$$G=3/(2D_{\mathrm{eff}})\mathrm{d}V^{2/3}/\mathrm{d}t=-1/2\Sigma\Delta p_i S_i/(\sigma V^{1/3})=-1/V^{1/3}\int 1/2(1/R_{i1}+1/R_{i2})\mathrm{d}S_i \qquad (1.19)$$

with sum over its facets i, with the respective surface area S_i and pressure difference Δp_i which results from the facet's curvature given by the principle radii R_{i1} and R_{i2} (Jurine et al., 2005). The effective diffusion coefficient $D_{\mathrm{eff}}=\mathrm{d}V/\mathrm{d}t/(S_i\Delta p_i)$ determines the speed of gas transfer through the bubble's surface as defined by Fick's law. G depends on the number of neighboring bubbles, which are equal to the number of facets, as displayed in Fig.1.9. For bubbles with less than approximately 14 facets, the growth rate is negative (Jurine et al., 2005).

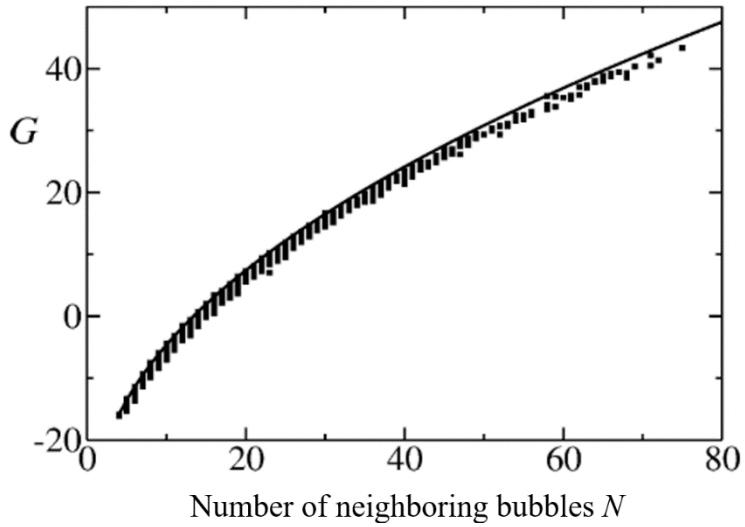

Figure 1.9: Dimensionless diffusive growth rate *G* of individual bubbles versus number of neighbors N from foam simulations and the theory of idealized foam cells, called isotropic Plateau polyhedra (IPP), which have *N* identical spherical-cap faces and satisfy Plateau's laws (solid line) (adapted from (Kraynik, 2006)).

Bubbles with negative growth rate eventually disappear owing to the growth of the larger bubbles. Both leads to a decrease of the number of bubbles for a fixed total bubble volume with increasing coarsening time. Starting initially with the same number of bubbles but different size distribution, the decreasing rates are quite distinct but converge to the same final state only within different time periods, as shown in Fig.1.10. At this final state, the decreasing rate are equal constants and the foam has reached the regime of self-similar growth. (Jurine et al., 2005)

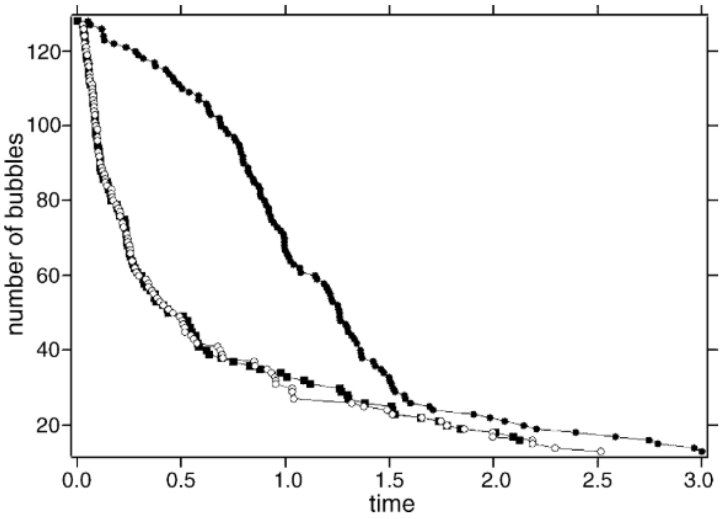

Figure 1.10: Decrease of the number of bubbles with coarsening time in simulations of a cluster of initially 128 bubbles with initially peaked volume distribution (closed circles) and exponential volume distributions (open circles and closed squares). The foam volume is constant, and the time units correspond to D_{eff}. (Jurine et al., 2005)

Self-similar growth at long times is evident from the linear growth of $\langle V \rangle^{2/3}$ in dry foams, as can be deduced from Fig.1.11. In two dimensional foams, the von Neumann´s law describes the growth of the bubble area A_N for each bubble with N facets

$$dA_N/dt = 2\pi/3\sigma D_{eff} (N-6). \quad (1.20)$$

From this as well as from the experimental data, a power law behavior $R_{32} \sim (\sigma D_{eff} \Delta t)^{1/2}$ can be derived for dry foams (Weaire and Hutzler, 1999).

Also, in wet foams, where bubbles are spheres entirely characterized by their radii, the bubble volume distribution relative to their average $V/\langle V(t) \rangle$ reaches a universal distribution at long times after a transient regime. The growth regime becomes self-similar and the average volume $\langle V(t) \rangle$ increases linearly with time. (Jurine et al., 2005).
Hence, $R_{32} \sim (\Delta t)^{1/3}$ is found for wet foams with spherical bubbles, which is in accordance with the constant volumetric growth rate found in "Ostwald ripening" theory (Lambert et al., 2010).

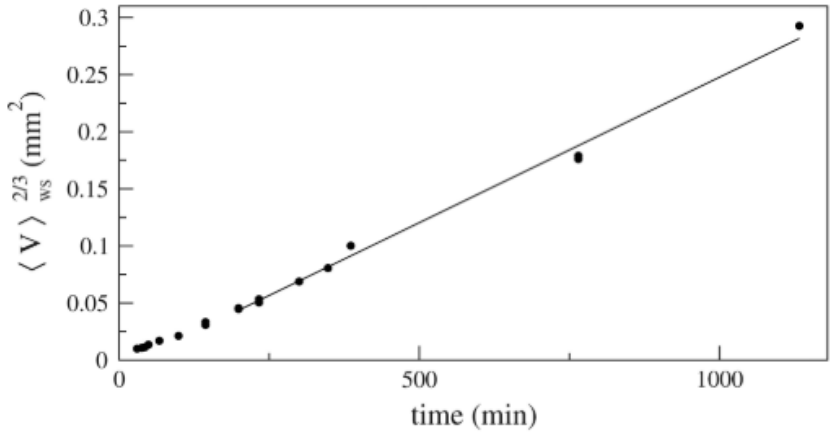

Figure 1.11: $\langle V \rangle^{2/3}$ from experimental data of bubble volume V in foam versus coarsening time (points) and linear fit to the data for t>250 min, corresponding to the self-similar growth regime (solid line).(Lambert et al., 2010)

Coalescence

Another instability mechanism causes an increase in average bubble size is the coalescence of bubbles due to rupture of separating lamellae. It sets in after the foam has drained and leads eventually to foam collapse. At short characteristic coalescence times, bubbles also coalesce during the foaming process. The equilibrium between bubble creation and coalescence determines the foam volumes that outlast the foaming process and its structural properties (Drenckhan and Saint-Jalmes, 2015). The rupture of a lamellae is caused either mechanically, leading to a deterministic time of rupture, or entirely by thermodynamic fluctuations leading to a stochastic rupture time. In both cases the rupture times strongly depend on the mechanical properties of the interfaces and the limiting cases of rigid and mobile interfaces are considered.

Regarding stochastic rupture of an isolated liquid film, the rupture time is set by the sum of timescales of four successive processes. The two interfaces of a film are attracted to each other by Van der Waals forces which are counteracted by the electrostatic and steric repulsion force of the surfactant molecule adjacent to the interfaces and result in a disjoining pressure depending on the film thickness h. The disjoining pressure $\Pi_{disjoin}$ profile, given in Fig.1.12, allows for two metastable states with different film thicknesses at the same disjoining pressure, called common and Newton black film. (Rio and Biance, 2014)

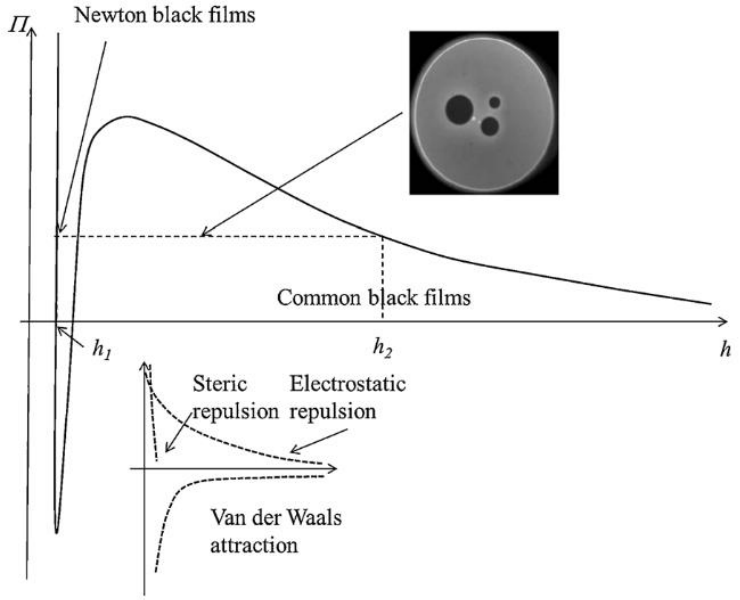

Figure 1.12: Schematic disjoining pressure curve versus film thickness h. Common black films (CBF) exhibit film thickness h_2, and Newton black films (NBF) thickness h_1. Photograph inset shows a spinodal decomposition between both states with thinner films (dark spots) inside a thicker film, typically observed in a Thin Film Pressure Balance which was developed by Mysels and Malcom (Mysels and Malcolm, 1966), and Exerowa et al. (Exerowa et al., 1987; Exerowa and Scheludko, 1971). Graph inset displays the contribution of steric, electrostatic and Van der Waals interactions.(Rio and Biance, 2014)

First, liquid film with initial thickness h drains to a thickness, which corresponds to a common black film (CBF). This takes tens of microseconds for rigid interfaces and less than a microsecond for mobile interfaces. Second, the film passes a barrier of $\Pi_{disjoin}$ to reach the state of a thinner newton black film (NBF), which last from hundreds of microseconds for mobile interfaces to almost infinity for rigid interfaces. Third, a thermal instability in film thickness fluctuation or surfactant concentration fluctuation at the interface develops and creates a patch of interface which is bare of surfactant. This takes between a few hundred microseconds for mobile to almost infinity for rigid interfaces. Once the bare spot has about the size of the film thickness h, a hole is created in the film within about 300 milliseconds. Last, the hole quickly opens within a negligible time of tenths of microseconds. It becomes clear, that the development of Newton black films and development of instabilities set the time scale for film rupture. (Rio and Biance, 2014)

In foams, when a critical capillary pressure is exceeded, which is defined by the disjoining pressure barrier, also spinodal decomposition between two film thicknesses may arise leading to Newton and common black films in the lamellae simultaneously, as shown in the inset of Fig.1.12. Subsequently, instabilities in the thinner part develop and lead to lamella rupture. In experiments on emulsions and foams, a critical osmotic pressure, at which coalescence occurred, increased linearly with the reciprocal lamella size $1/R_{lamella}$. As the critical osmotic pressure Π_{crit} can be related to the capillary pressure P_c via

$$\Pi_{crit}=P_c-2\sigma/R_{lamella}=\sigma/R_{crit}-2\sigma/R_{lamella}, \quad (1.21)$$

σ/R_{crit} corresponds to the critical capillary pressure (Rio and Biance, 2014). Fig.1.13 exemplarily displays the dependency of the foam lifetime on the capillary pressure and shows a strong drop at certain pressure corresponding to the critical capillary pressure (Khristov et al., 2002).

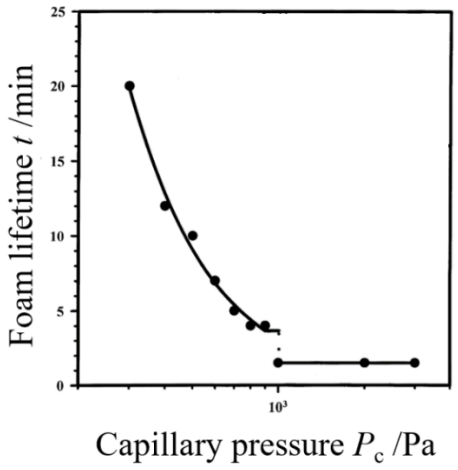

Figure 1.13: Foam lifetime of foams with Newton black films made from sodium dodecyl sulfate solutions versus capillary pressure P_c (adapted from (Khristov et al., 2002)).

The mechanically driven coalescence can be induced by shear between two bubbles and is defined by the contact time of the bubbles and the time necessary to drain the liquid in the contact zone. Also, two contacting bubbles coalesce, when they are pulled apart, due to surfactant depletion in a nipple that forms in the contact zone. When bubbles are pressed together, the rupture depends critically on the amount of liquid present at the beginning of contact. (Rio and Biance, 2014)

In both cases, for coalescence due to a critical capillary pressure or liquid fraction, the foam collapse is mainly determined by the foam drainage time for mobile interfaces, which is in the order of tens of minutes. For more rigid interfaces, the collapse is determined by the sum of the foam drainage time, which may last several hours, and the stochastic time scale for instabilities to develop in the lamellae (Rio and Biance, 2014). For concentrated monodisperse emulsion, a scaling of the droplet size with $t^{-1/2}$ was found in simulations, shown in Fig.1.14. This agrees with a stochastic film rupture, as the coalescence rate is proportional to the droplet area. However, the disjoining pressure varies with the bubble size, but its affect was neglected for the analysis. (Deminiere et al., 1999)

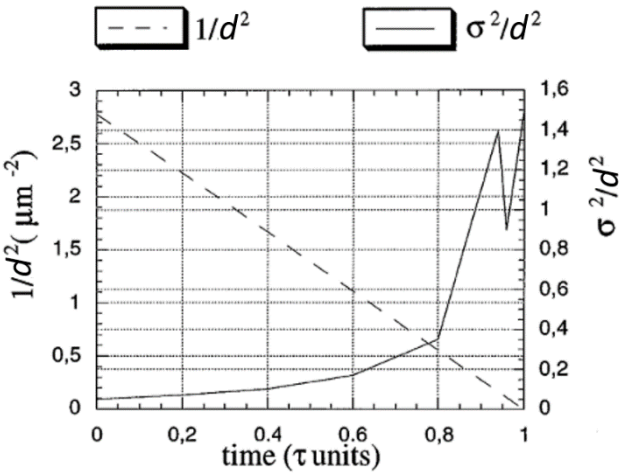

Figure 1.14: Time dependency of $1/d^2$ and σ^2/d^2 (polydispersity) deduced from Monte Carlo simulations, with d being the average droplet size in a concentrated, initially monodisperse emulsion and σ being the standard deviation of the size distribution.(adapted from Deminiere et al., 1999)

Bubble size distribution determination

The bubble size distribution in foam may be obtained from photographs of foam through a flat transparent interface at the foam container wall. Capturing the foam with an endoscope submerged into the foam may provide more reliable information, because the foam in the center of the foam column is most likely in a less distorted state. In both cases the size distribution of the bubbles captured is not equal to the bulk bubble size distribution because bubbles organize differently at flat interfaces. However, it gives a good approximation of the average bubble size. More exact bulk size distribution may be obtained from image analysis of single bubble layers spread onto liquid surfaces but requires stable bubbles. In general, multiple reflections and refractions of light at the lamellae complicate the acquisition of the foam structures in the bulk by photography (van der Net et al., 2007). Resulting complex image features impede quantitative and automated analysis of foam structures. An approach to solving these issues is presented chapter 2. A less invasive technique makes use of the property of foam to increasingly scatter light with decreasing bubble size, in order to access the average bubble size. From the liquid fraction, obtained with one of the techniques described above, and the light attenuation, the average bubble size may be determined. The most powerful techniques for foam visualization comprise magnetic resonance and X-ray tomography. These provide 3D scans of the bulk foam revealing size, shape and environment of every bubble. As films are not detected below a considerable thickness, tomography is mainly restricted to moderately wet foams. The long measuring times also require extremely stable and rigid foams.

1.2.4 Foam Rheology

Liquid foams act either like a solid or a liquid depending on the strain they are exposed to, their gas volume or liquid volume fraction, and their bubble size distribution. At small shear strain, foams behave as solids, as schematically shown in Fig.1.15A, and their elasticity arises from the increase in interfacial energy *E* upon deformation. The elasticity, characterized by the shear modulus *G*, decreases with decreasing gas volume fraction and vanishes at the critical packing fraction of the bubbles when bubbles become spacialy separated spheres, as illustrated in Fig.1.15B. The maximum strain a foam can sustain before bubbles rearrange, is the yield strain, corresponding to a yield stress. The yield stress also decreases with decreasing gas volume fraction and becomes zero at the critical gas volume fraction (see Fig.1.15B). In yielding foam, the stress is relaxed by rearrangements of bubbles. This results in plastic foam deformation and eventually laminar flow of the bubbles at high strain rates (see Fig.1.15A), and macroscopically the foam behaves as shear-thinning fluid. The flow behavior is also dependent on the foam structure, i.e. the bubble size distribution, and dynamics at interfaces that set the conditions of flow in films and Plateau borders. Generally, foam rheology is considered at time scales that fix the gas volume fraction. But slow flow is also coupled to aging effects like bubble rearrangements due to coarsening.

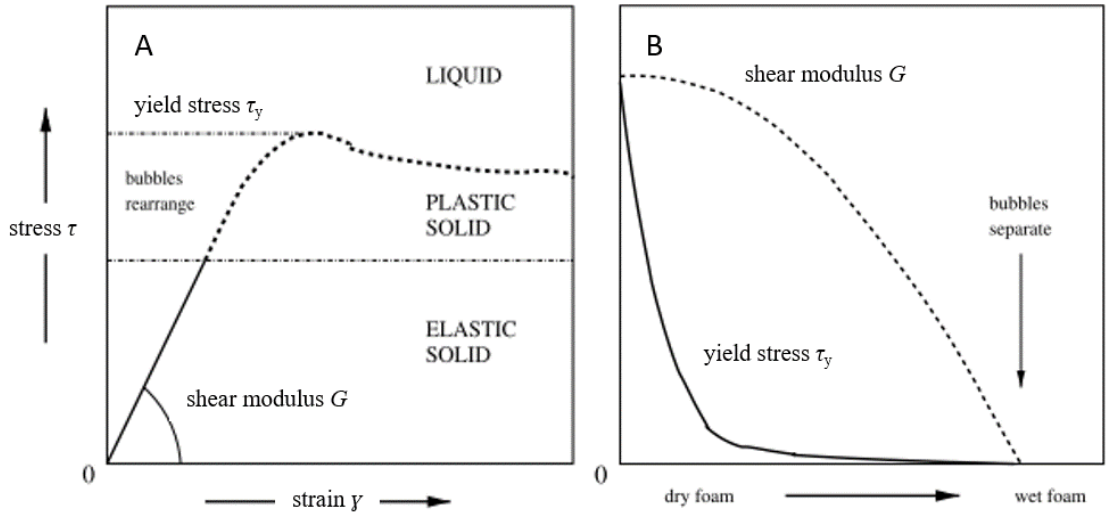

Figure 1.15: (A) Schematic stress–strain correlation for a liquid foam. Shear modulus *G* given by the ratio of stress τ and strain γ increase linearly with increasing strain below the critical strain at which bubbles start to rearrange. At higher strains, bubbles flow and foam exhibits liquid-like behavior. (B) Yield stress and shear modulus correlate with the liquid fraction of the foam. (The shear modulus is shown for the two-dimensional case) (adapted from (Weaire et al., 2003))

Viscoelasticity and yield point

Foams are viscoelastic fluids, i.e. they possess partially viscous and partially elastic behavior. In foams that are strained a fraction of the imposed energy is stored within the deformed bubble interfaces and the other fraction dissipates because of intrinsic friction. Basic shear rheological parameters can be defined with a model consisting of a homogeneous medium, e.g. foam, between two parallel plates with area S and distance y. Shifting one plate sticking to the foam bulk by a distance x while the other plate stays fixed, causes a strain $\gamma = x/y$, assuming the resulting flow in the foam is laminar and stationary. The temporal change of γ per time unit is the shear rate $d\gamma/dt = \dot{\gamma}$. The shear stress exerted onto the foam $\tau = F/S$ is defined as the force F required to move that plate normalized by its area S. Foams exhibit a range, called linear viscoelastic regime, in which the resulting stress τ is proportional to the applied strain γ:

$$\tau = G\gamma \tag{1.22}$$

with the constant shear modulus G. The limit of the linear regime is marked by the yield stress τ_y at which the foam structure breaks, i.e. the bubbles reposition, and the apparent shear modulus starts to decrease with increasing stress (see Fig.1.16A). The viscoelasticity is commonly characterized by the stress/strain relationship in oscillatory sinusoidal deformation, with a strain amplitude γ_0 in the linear viscoelastic regime, at a fixed angular frequency ω: $\gamma = \gamma_0 \sin(\omega t)$. This results in a shear stress response with amplitude τ_0 and a phase angle δ between 0° for ideal elastic solids and 90° for ideal viscous liquids: $\tau = \tau_0 \sin(\omega t + \delta t)$.

The sum of the storage modulus $G' = \tau_0/\gamma_0 \cos(\delta)$, characterizing the elastic contribution, and the loss modulus $G'' = \tau_0/\gamma_0 \sin(\delta)$, characterizing the viscous contribution, gives the complex shear modulus:

$$G^* = G' + iG'' . \tag{1.23}$$

The ratio between G' and G'' is called loss factor and gives the tangent of the phase angle $\tan(\delta)$.

When varying the strain amplitude at a fixed frequency in an oscillatory shear measurement, characteristic curves for G' and G'', as shown in Fig.1.16A, are obtained and the linear viscoelastic regime, where G' and G'' are constant, can be determined.

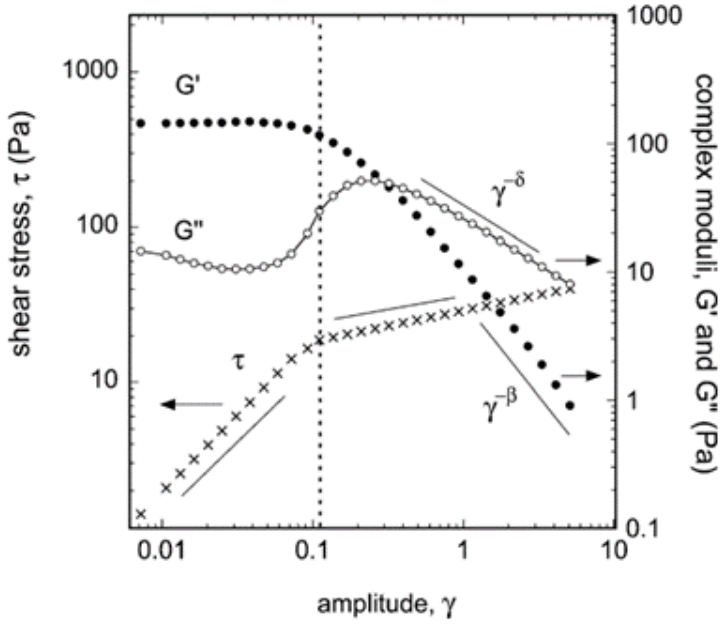

Figure 1.16: Typical results of elastic modulus *G*', loss modulus *G*'', and shear stress τ versus γ for an oscillatory strain amplitude sweep. The yield stress, corresponding to the end of the linear viscoelastic regime here with constant G´, is marked with a vertical dashed line. (Marze et al., 2009)

Storage and loss modulus also exhibit characteristic dependence on the oscillatory frequency for shear deformation with fixed strain amplitude γ_0 in the linear viscoelastic regime. The frequency dependence of the complex shear modulus of jammed systems is described by

$$G^*(\omega)=G_0(1+(i\omega/\omega_c)^{1/2})+i\omega\eta_\infty \quad (1.24)$$

with the plateau modulus G_0, the fluid viscosity in the high frequency limit η_∞, and the characteristic relaxation frequency ω_c. The latter is set by the dissipation in the lamellae which dominates in case of rigid interfaces and $\omega_c \sim 1/R$. For mobile interfaces, the dissipation occurs mainly at the junctions between lamellae and Plateau borders. The characteristic relaxation frequency $\omega_c \sim 1/(\eta R+\eta_{interface})$ increases with the dilatational interfacial viscosity $\eta_{interface}$ and is one order of magnitude higher than for rigid interfaces. (Cohen-Addad et al., 2013)

Modelling yield stress and shear modulus

Batchelor et al. (Batchelor, 1970) showed that the elastic stress in a suspension scales with the product of the interfacial tension and the integral over all interfaces per unit volume of foam. Hence, in a monodisperse foam the elastic modulus as well as the yield stress scale with σ/R. To predict their dependence on the gas volume fraction, a series of studies, starting from Princen (Princen, 1982, 1979), considered topological changes of a 2D foam model with zero liquid fraction comprising of ordered monodisperse hexagonal bubbles. The model, comprising of four, equally sized, hexagonal cells is shown in Fig.1.17A.

When an external strain is applied while Plateau's rule is obeyed (fixed 120° angle), the vertices shift to defined positions (Fig.1.17B), and the edge lengths of the hexagons change up to the point where the bubbles take the shape of rectangles (Fig.1.17C). This marks an unstable state, as Plateau's rule is violated, corresponding to the yield strain. At higher strain the stress is relaxed in a topological rearrangement of the bubbles, called T1 event, arriving in a stable state again (Fig.1.17C). Such T1 events were also observed in 2D foams, shown by the photographic insets in Fig.1.17 (Dollet and Raufaste, 2014). The bubble irreversibly repositioned and the foam is plastically deformed. From the force, defined by the surface tension and the changes in edge length, and the strain calculated from the geometry as a function of edge length, the yield stress $\tau_y=0.525\sigma/R$ can be deduced (Princen, 1982).

With the definition of the gas volume fraction as the ratio between a circular and a hexagonal area an expression for the elastic modulus in dependence of the gas volume fraction φ was derived $G'=0.525\sigma/R\varphi^{1/2}$ (Princen, 1982). Princen modified the liquid fraction by inserting concave triangles at the vertices which strongly reduces the yield stress and yield strain (Princen, 1982). Qualitatively, these findings were confirmed in simulations on 3D Kelvin foams.

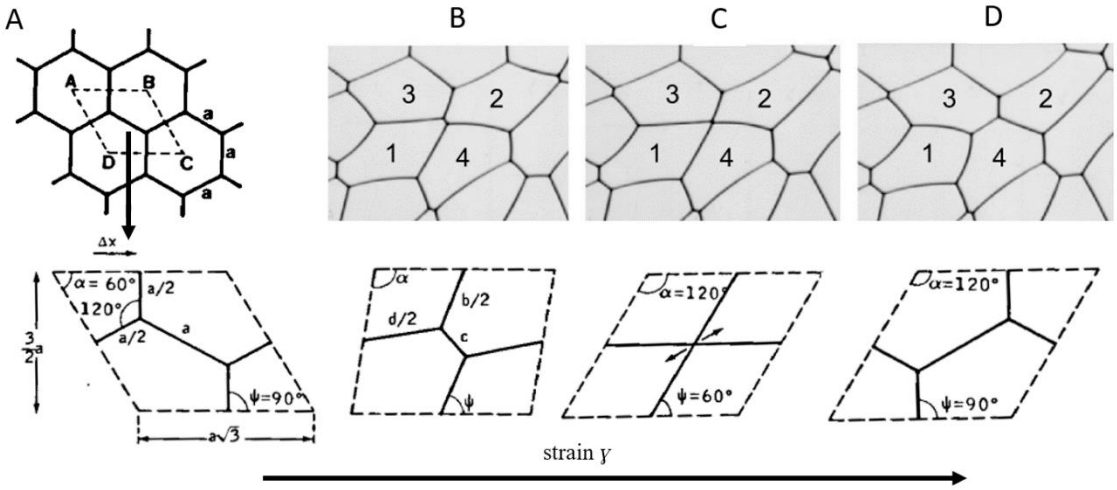

Figure 1.17: (A) Honeycomb lattice model with four cells obeying Plateau´s rule with equal side lengths at strain $\gamma=0$. B) Side lengths change when strain γ is applied but Plateau´s rule is still obeyed. (C) Cells become rectangular, violating Plateau`s rule, at $\gamma=2/(3\sqrt{3})$ and this instable state correspond to the yield strain. (D) Surpassing the yield point, cells retain a stable state with hexagonal shape and equal side lengths. (adapted from (Princen, 1982)) Photograph insets illustrate the plastic bubble rearrangement in the T1 event. (Dollet and Raufaste, 2014)

Several approaches were made to model the influence of disorder in the bubble arrangements (Cox and Whittick, 2006; Kruyt, 2007; Stamenović, 1991) but simulating disorder while obeying Plateau's rule simultaneously stays challenging.

From simulations on 3D polydisperse foams, it was pointed out that the Sauter bubble diameter takes into account the effect of polydispersity (Kraynik et al., 2004). Princen (Princen, 1985, 1982) suggested an extension of the model for the yield stress $\tau_y \approx \sigma/R\varphi 1/3 f(\varphi-\varphi_c)$ in 3D foams, accounting for the excess of the gas volume fraction over the critical packing fraction with a function $f(\varphi-\varphi_c)$ that becomes zero at the jamming transition. From experiments on emulsions, he found $f(\varphi-\varphi_c)$ to be described by $(\varphi-\varphi_c)^2$ with $\varphi_c=0.7405$, as applicable for Kelvin foam (Princen, 1985). Mason et al (Mason et al., 1996) concluded following model for the yield stress from experiments on monodisperse emulsion with $\varphi_c=0.635$ corresponding to random close packing:

$$\tau_y = k\,\sigma/R_{32}(\varphi-\varphi_c)^2 \tag{1.25}$$

with a numerical prefactor $k\approx 0.5$. Lexis and Willenbacher (Lexis and Willenbacher, 2014a) empirically extended the model by a weak contribution of the viscosity of the liquid phase normalized to the viscosity of water $\tau_y \sim (\eta/\eta_w)^{1/3}$.

For the shear modulus of polydisperse emulsions, Princen and Kiss (Princen and Kiss, 1986) found $G' \approx \sigma/R\varphi^{1/3}(\varphi-\varphi_c)$. A decade later, Mason et al. (Mason et al., 1995) proposed a model for the shear modulus, rationalized with an anharmonic potential between droplets in contact (Lacasse et al., 1996):

$$G' = a\,\sigma/R_{32}\varphi(\varphi-\varphi_c). \tag{1.26}$$

With a numerical prefactor $a\approx 1.6$, this agreed with experiments on disordered monodisperse emulsion (Lacasse et al., 1996) and foams (Marze et al., 2009; Saint-Jalmes and Durian, 1999). However, these experimental data consider systems with mobile interfaces whereas for rigid interfaces prefactors a and k were found to be higher and depend on the interfacial elasticity (Lexis and Willenbacher, 2014b; Tsibranska et al., 2020b). The correlation of yield stress and shear modulus with interfacial elasticity is further addressed in Chapter 5.

Quasi-static foam flow

Flowing foams are non-Newtonian fluids with their viscosity $\eta=\tau(\dot{\gamma})/\dot{\gamma}$ being a nonlinear function of the shear rate $\dot{\gamma}$. When foams are exposed to a stress greater than the yield stress τ_y they behave as shear thinning fluid described by a Herschel-Bulkley law:

$$\tau=\tau_y+k_v\,\dot{\gamma}^n=\tau_y+\tau_v(\dot{\gamma}) \tag{1.27}$$

with the foam consistency k_v and the power law index $n<1$. The shear rate dependent viscous stress $\tau_v(\dot{\gamma})$ depends on the mechanism of viscous dissipation during foam flow and is not well understood (Denkov et al., 2008).

For the case of mobile interface and neglectable surface force, it may be assumed that the dissipation arises from the viscous friction in the lamellae of bubbles sliding past each other.

Their thickness $h \sim RCa^{1/2}$ and the viscous bulk stress

$$\tau_v \approx \sigma / R\, Ca^{1/2} \tag{1.28}$$

scale with the capillary number $Ca=\eta\dot{\gamma}R_{32}/\sigma$ with a power of n=1/2 (Denkov et al., 2008). This has been confirmed in experimental studies (Denkov et al., 2005, 2009; Princen and Kiss, 1989), as shown in Fig.1.18. For micrometer-sized bubbles, the surface force can become relevant and the power law index n>1/2. In case of rigid interfaces, the dissipation arises also from the viscous friction in the dilated interfaces and n<1/2. Also, n<1/2 was observed for liquid phase that exhibits shear-thinning behavior. (Tcholakova et al., 2008)

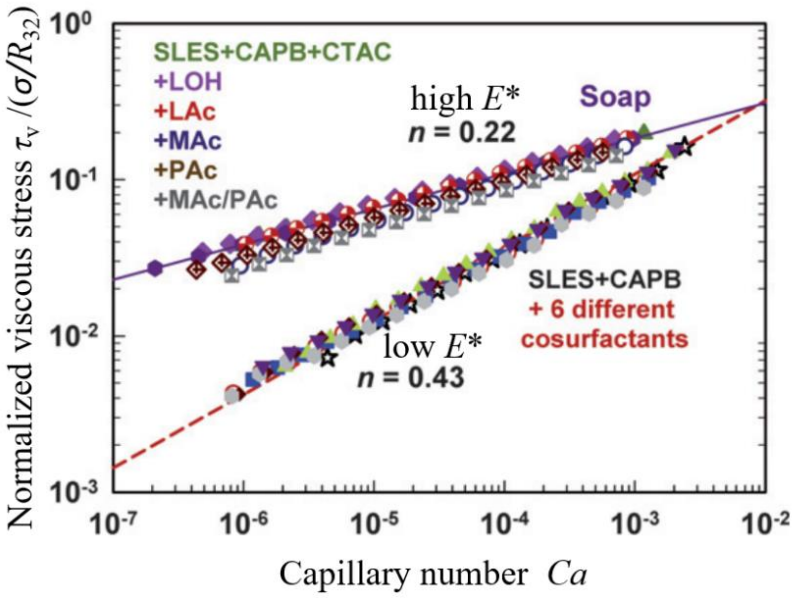

Fig1.18: Viscous stress normalized by ratio of interfacial tension and bubble Sauter radius σ/R_{32} versus capillary number Ca of foams made from soap, and solutions of sodium lauryl ether sulfate (SLES), coco amidopropyl betain (CAPB) , cetyl trimethyl ammonium chloride (CTAC), lauric acid (LAc), myristic acid (MAc), palmitic acid (PAc), and lauryl alcohol (LOH), rendering either high or low complex interfacial dilatational moduli E^*. (adapted from (Denkov et al., 2009))

Characterization of foam rheology

The foam rheological parameters may be accessed experimentally using rotational rheometry. Either a torque is applied onto the foam sample and the angular displacement is measured or vice versa. The torque M and the angular displacement Φ are proportional to the stress and the strain, respectively, with pre-factors depending on the geometry of the sample fixture. Commonly, for low viscosity fluids concentric cylinders are used, which consist of a cylindrical bob centered in a cup that contains the fluid and either the bob rotates (Searle method) or the cup rotates (Coutte method) while the counter part is fixed. The gap width is usually not bigger than 3% of the cup radius R_{cup}, to be able to assume a constant shear rate across the gap. However, it must be not smaller than ten times the size of the dispersed phase in order that the system can be treated as continuum.

The stress in such a geometry, displayed in Fig.1.19A, with a rotating bob with radius R_B and length L is

$$\tau=(2\pi R_B^2 L)^{-1}M \quad (1.29)$$

and needs to be corrected for the contribution of the front face at the bottom of the bob. The strain rate is $\dot{\gamma}=2R_{cup}^2/(R_{cup}^2-R_{vane}^2)\omega$ (1.30)

and the viscosity $\eta=\tau(\dot{\gamma})/\dot{\gamma}$ can be calculated.

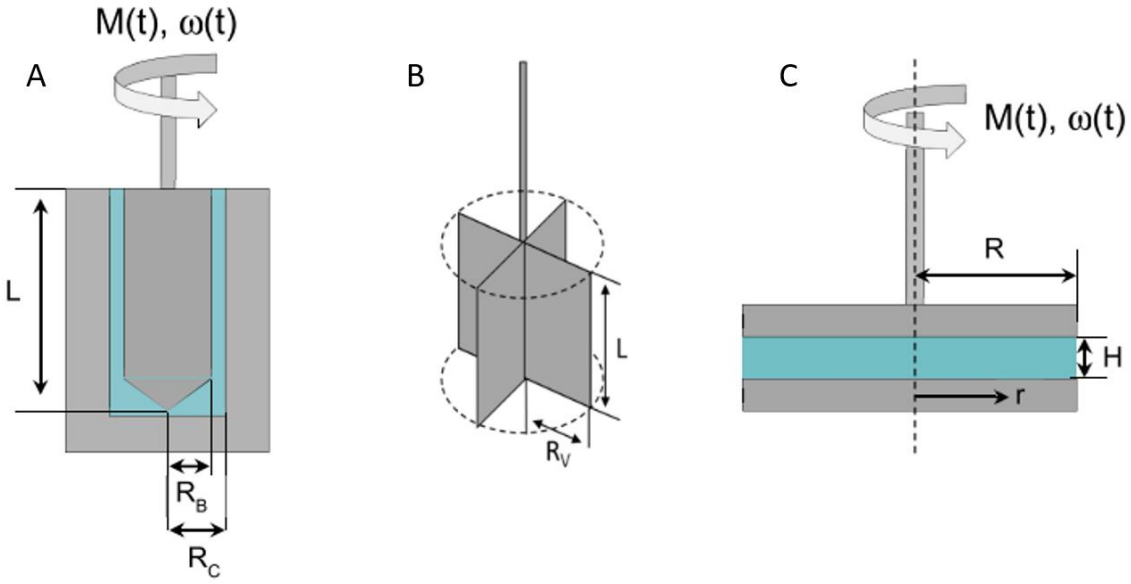

Figure 1.19: Schematic illustration of rotational rheometry probes: (A) concentric cylinder (B) vane measuring system (C) plate/plate (Lexis and Willenbacher, 2018)

To avoid wall-slip, the bob may be replaced by a vane rotor for yield stress measurements, as the one shown in Fig.1.19B. It also is less invasive than a full cylinder during sample loading. For a vane rotor with four blades of height L the shear stress at the surface defined by the vane radius R_{vane} is given as:

$$\tau=(2\pi R_{vane}^2 L+\pi R_{vane}^3)^{-1}M \quad (1.31)$$

and the apparent strain in the gap reads:

$$\gamma=2R_{cup}^2/(R_{cup}^2-R_{vane}^2)\Phi. \quad (1.32)$$

The yield stress is determined in a creep test: the sample is loaded with a certain stress, and if the stress is below the yield stress, a constant equilibrium strain establishes with time, as illustrated in Fig.1.20A. If the stress exceeds the yield stress, the strain increases with time and a constant shear rate establishes.

These stress loads can be applied in a series of stepwise increasing stresses and the onset of the vane rotation clearly indicates the structural changes when exceeding the yields stress. The resulting strain curve $\gamma(\tau) \sim \tau^n$ is illustrated in Fig.1.20B and exhibits an elastic regime where $n=1$ at low stresses and a second regime at higher stresses where $n>1$. The stress at the intersection point of the tangent in both regimes marks the yield stress τ_y. Another method to determine the yield stress is to measure the stress upon quasi-static shear start-up (see Fig.1.20C). The stress overshoots at the onset of bubble rearrangements before a constant steady state value is reached, and this stress maxima characterizes the static yield stress, as visualized in Fig.1.20D. (Cullen et al., 2003)

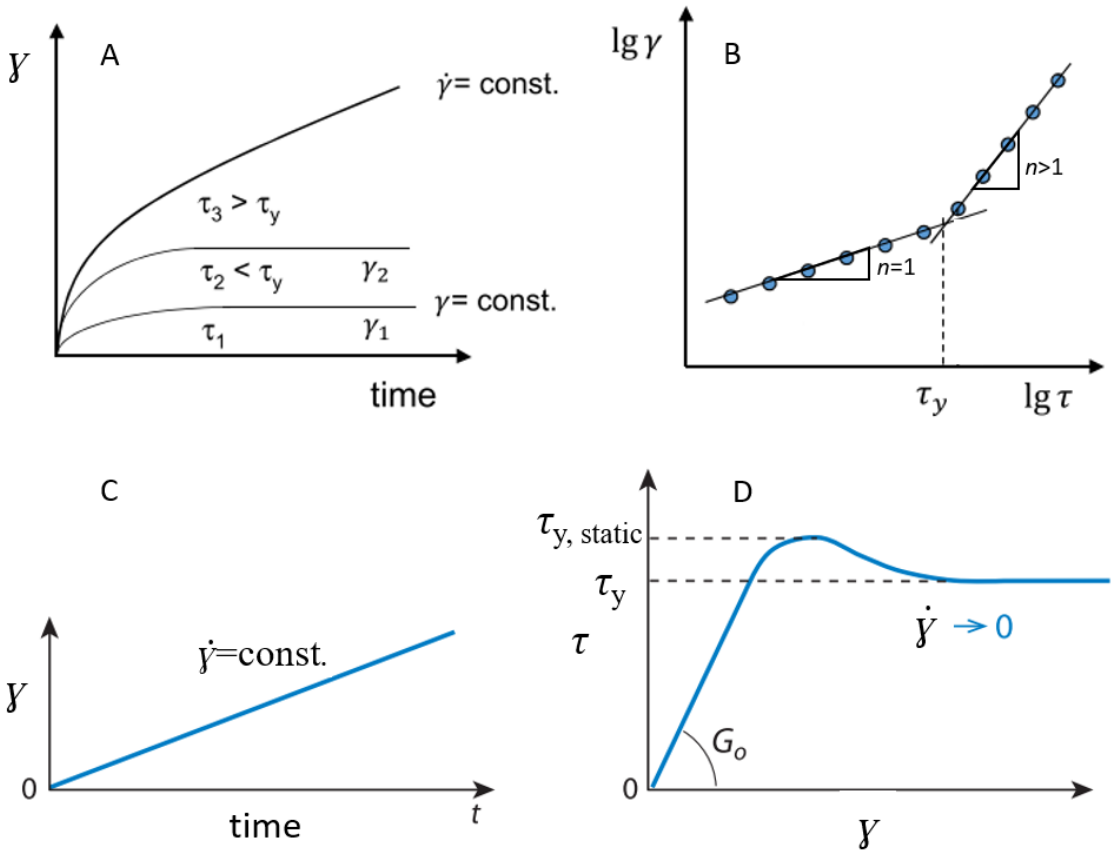

Figure 1.20: Two methods for determination of yield stress in rotational rheometry: (A) Creep tests: sample is loaded with a constant stress. A constant strain establishes with time. If the stress exceeds the yield stress, the strain increases with time with a constant shear rate. (B) Series of stepwise increasing stress results in a strain curve with two regimes ($n=1$ and $n>1$). The stress at the intersection point of the tangents in both regimes mark the yield stress. (adapted from (Lexis and Willenbacher, 2018)) (C) Quasi-static shear start-up experiment: A shear strain with a low shear rate is applied to a sample. (D) The stress measured as a function of strain reaches a maximum value marked as the static yield stress and then decreases toward its steady-state limit yield stress. (adapted from (Cohen-Addad et al., 2013))

For oscillatory shear measurements, the foam sample is probed in between two circular parallel plates of radius R_{plate} of which one plate rotates and one is fixed, as illustrated in Fig.1.19C. The gap width H is adjustable to ten times the size of the dispersed phase, making the system suitable for foams with large bubbles. The stress is

$$\tau=3/(2\pi R_{plate}^3)(1+1/3d\ln(M)/d\ln(\dot{\gamma}))M \quad (1.33)$$

and the strain

$$\gamma=r/H\Phi \quad (1.34)$$

varies with the distance from the rotational axis r. The viscoelasticity is probed at fixed stress amplitude with varying oscillation frequency or fixed frequency with varying stress amplitude and the complex shear modulus is determined as described in Chapter 1.2.4.1.

Accurate determination of yield stress, shear modulus and viscosity in foams are often perturbed by wall-slip, shear localization or shear banding, and changes in foam structure due to temporal instabilities or shear induced coalescence. Wall-slip is successfully prevented with rough probe surfaces with cavities of the size of the dispersed phase. The temporal instability of foams requires short measuring times and their fragility especially at high gas volume fractions sets a need for minimizing the invasiveness of the probe and sample loading process. An approach for in-situ characterization of foam yield stress is presented in Chapter 3.

1.3 Interfaces

The interface between immiscible fluids, as gas and aqueous solution in liquid foams, exhibits a tension deriving from attractive forces between the water molecules inwards and tangential to the interface. The interfacial tension results in a tendency to minimize the interfacial area, which drives the instability of bubbles and foams, and bestows the foam with elasticity. Surface active species in an aqueous solution adsorb to the interface due to their amphiphilic character and reduce the interfacial tension, stabilizing any area excess above the minimal interfacial area. Adsorption and surface tension dynamics play a role in foam formation, when fresh interfaces are created and in foams at rest when the interfacial area changes, as it is the case during growth and shrinkage of bubbles, or rupture of lamellae. The adsorbed surface-active molecules may also interact tangential to the interface and form layers with distinct interfacial rheology. As discussed above in terms of rigid and mobile interfaces, the interfacial rheology severely influences the stability of the foam structure and is also shown to contribute to the foam bulk rheology in Chapter 5.

1.3.1 Interfacial tension

The surface tension σ of aqueous surfactant solutions is subject to the dynamics of bulk diffusion and often bulk convection, as well as to the dynamics of interfacial adsorption and desorption, which in turn depends on the concentration and state of the surface-active species in the bulk. The tension of a freshly created surface exhibits a fast decrease with time and eventually reaches an equilibrium value when the interfacial concentration is saturated. The equilibrium interfacial tension decreases with increasing bulk concentration c until the critical micelle concentration is reached. Above that concentration the equilibrium interfacial tension remains essentially constant and further addition of surfactant may lead to formation of micelles or other forms of aggregates in the bulk. The relation between interfacial tension and surface concentration Γ below the critical micelle concentration is described in the equation of state $\sigma(\Gamma)$.

For interfaces at equilibrium state, covered with a single species of monomeric surfactants that reversibly adsorb, Γ is given by the Gibbs adsorption equation

$$\Gamma = -(\mathrm{d}\sigma/\mathrm{dln}c)\ 1/(nR_\mathrm{g}T) \tag{1.35}$$

where R_g is the gas constant, T is the temperature, and n is a constant accounting for the number of species constituting the surfactant. It requires that the surface excess, i.e. the difference between bulk and interfacial concentration, is approximately equal to the interfacial concentration, which is only applicable for dilute solutions and highly surface-active species. The dependence of Γ on the bulk concentration is commonly approximated by the Langmiur isotherm

$$\Gamma = \Gamma_\mathrm{max}K_\mathrm{L}c/(1+K_\mathrm{L}c), \tag{1.36}$$

where Γ_max is the maximum interfacial concentration and K_L is the equilibrium Langmuir adsorption constant. At low concentrations or $K_\mathrm{L}c<<1$, it reduces to the Henry isotherm $\Gamma=\Gamma_\mathrm{max}K_\mathrm{L}c=K_\mathrm{H}c$ with the equilibrium Henry adsorption constant K_H.

From these equations above, the interfacial equation of state, i.e. the Szyzkowski equation, can be derived

$$\Pi=\sigma_0-\sigma=nR_gT\Gamma_\mathrm{max}\ln(1+K_\mathrm{L}c), \tag{1.37}$$

where Π is the surface pressure and σ_0 is the interfacial tension of pure water. However, it is applicable for ideally dilute solutions with an interfacial monolayer of surfactants exhibiting no molecular interaction. The adsorption isotherm differs significantly, in case of surfactant mixtures, with competitive adsorption behavior, irreversible adsorption, as exhibited by proteins that unfold upon adsorption at the interface, and interfacial or bulk aggregation.

1.3.2 Interfacial Rheology

The interfacial rheology is a two-dimensional equivalent to bulk rheology with elasticity and viscosity in shear (constant area, but changing shape, see Fig.1.21A) and dilation (constant shape, but changing area, see Fig.1.21B) being the main mechanical quantities. Interfaces covered with surface active species exhibit nonlinear rheology and complex relations between interfacial deformation and interfacial stress caused by lateral molecular interactions.

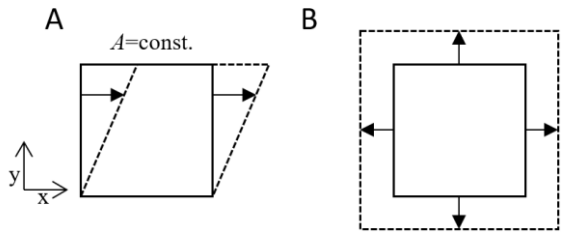

Figure 1.21: Schematic illustration of interfacial deformation in (A) shear with constant interfacial area but changing shape and in (B) dilation with constant shape but changing interfacial area.

Analog to the oscillatory bulk rheology, the response of viscoelastic interfacial layers to periodic shear deformations are thus described by the complex interfacial modulus

$$G_i^* = G_i(\omega) + i\omega\eta_{interface}(\omega) \quad (1.38)$$

with the oscillation frequency $\omega = 2\pi f$ and the interfacial shear viscosity $\eta_{interface}$. (Krägel et al., 2008)

As the interfacial area and hence the interfacial concentration is constant in interfacial shear rheology, it provides a suitable method to study interfacial structures (Miller et al., 2010). At sufficiently high shear stresses, the interfacial structures rupture leading to a measurable abrupt increase in deformation. This provides insights, analog to a bulk yield stress, into the strength of an interfacial intermolecular network.

Dilatational rheology describes the response in terms of interfacial tension $\sigma(t)$ on changes of interfacial area $A(t)$. For interfaces, which do not respond purely elastic, the change in interfacial tension follows the area change with a certain delay due to relaxation processes. Typically, the interfacial rheology is probed with oscillatory deformation. At small amplitudes of interfacial area variations $A(\omega)$-A_{eq} and an angular frequency $\omega = 2\pi f$, the complex interfacial elasticity is defined as

$$E^*(\omega) = d\sigma(i\omega)/d(\ln A(i\omega)) = E'(\omega) + iE''(\omega), \quad (1.39)$$

with $d(\ln A(i\omega)) \approx (A(i\omega) - A_{eq})/ A_{eq}$.

It consists of a real part $E'(\omega)$, giving the interfacial dilatational elasticity, and an imaginary part $iE''(\omega)$, yielding the interfacial dilatational viscosity

$$\eta_{interface}=E''(\omega)/\omega. \quad (1.40)$$

In the case of a single surfactant layer with diffusion controlled interfacial adsorption, the frequency dependence of the interfacial elasticity is given by

$$E(i\omega)=E_\infty\,(1-(1-i)(\omega_D/\omega)^{1/2})^{-1}, \quad (1.41)$$

with the interfacial elasticity in the high frequency limit $E_\infty=-d\sigma/d\ln\Gamma$ and the characteristic frequency $\omega_D=D/2(dc/d\Gamma)^2$ given by the adsorption isotherm Γ as a function of the surfactant bulk concentration c. (Miller et al., 2010)

In order to determine the interfacial rheological characteristics a viscometric flow field is required and one must account for the coupling between interfacial and bulk flows. Also, gradients of the interfacial concentration of surface-active species perturb the interfacial rheology measurement, particularly in dilation at low oscillatory frequencies and high strains. The concentration gradients cause surface tension gradients, and herby stresses, leading to convective motion in the interface called Marangoni flow. The mobility of the interface is restricted by Marangoni stresses resisting the surface tension gradient and range between the limiting cases of surfactants forming mobile interfaces free of tangential stresses and those forming immobile, rigid interfaces (Cohen-Addad et al., 2013).

Bulk-interface interactions and Marangoni flows also occur in foams subject to drainage and are made responsible for the slow drainage in foams stabilized by surfactants forming rigid interfaces. The gravity driven liquid flow in Plateau channels is thinning the channel but also causing a drag on the channels' interface. This drag is thinning down the interfacial coverage causing a gradient in surface tension, as schematically visualized in Fig.1.22. An upwards liquid flow arises in the interface that counteracts this gradient and the drainage of the Plateau channel (Durand and Langevin, 2002).

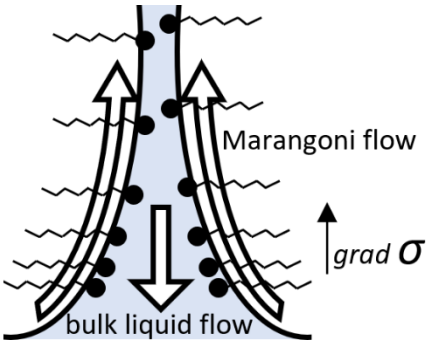

Figure 1.22: Schematic visualization of Marangoni flows occurring in liquid films and channels, due to surfactant concentration variations in the interfaces.

The Marangoni flow results from the interfacial elasticity due to surface tension gradients, generally referred to as Gibbs elasticity. Correlations between the interfacial elasticity and the foam and foam film drainage rate were found by several groups (Bhamla et al., 2014; Golemanov et al., 2008; Koehler et al., 2000; Saint-Jalmes et al., 2004) but also refuted experimentally by others (Frostad et al., 2016; Lin et al., 2018). The latter claim that one must consider not only Marangoni stresses in the absorbed layer but also its structure, which can be characterized using different interfacial rheological methods (Lin et al., 2018). For instance, solutions of small molecular weight surfactants exhibit no measurable interfacial viscoelasticity in shear and small elasticities in interfacial dilation, solely associated with the Gibbs elasticity. Proteins in contrast, can form far more complex interfacial layers with strong intermolecular interactions and considerable interfacial viscoelasticity in shear and high elasticity in dilation. Their viscoelasticity exceeds strongly the extent of the Gibbs-Marangoni effect (Lin et al., 2018). The strong variation in interfacial elasticity between different surface-active species is also addressed in Chapter 5.

The impact of interfacial rheological properties exceeds the microscopic range captured by interfaces and foam films and reflects in the rheology of the foam created with the particular surfactant system (Cohen-Addad and Höhler, 2014). Interfacial rheology studies generally consider monolayers of surface-active species on a large bulk solution reservoir, providing defined viscometric flow fields. For foaming, solutions exceeding several times the critical micelle concentration are required to stabilize the enormous interfacial area in foams, and the interface to bulk solution ratio is quite distinct. Accessing the interfacial surfactant concentration of the bubbles, which is subject to temporal and spacial variations inside the foam, is not feasible. However, experimentally correlations between foam elasticity and yield stress and the apparent interfacial elasticity of solutions at concentrations suitable for foaming were found for a vast variety of foaming systems. This topic is further addressed in Chapter 5.

Determination of interfacial rheology

For measuring interfacial shear rheology, the contribution of the interface to the force acting onto the probe should dominate over the contribution from the bulk. For viscoelastic interfaces the ratio between those contributions is given by following version of the Boussinesq number

$$Bq(\omega) = \eta_{\text{interface}}/(\eta L) \tag{1.42}$$

with the interfacial shear viscosity η_i, the subphase viscosity η, and a characteristic length scale L (Vandebril et al., 2010). $Bq >> 1$ is required to accurately calculate the interfacial rheological properties from the measurement (Vandebril et al., 2010). Several probes were developed minimizing the characteristic length in the Bq number by reducing the probes size or maximizing the contact perimeter between probe and interface, while keeping the contact area to the subphase small. With a magnetic rod interfacial shear rheometer, an interfacial shear flow is set between a rod, that is set in motion using a magnetic field, and the walls of a channel in which the rod is placed.

The velocity profile between the rod and the walls is linear for narrow channels and high interfacial viscosities. For sensitive rotational rheometers, 2D equivalents of the Couette geometry, as the bicone, and the double wall Couette geometry, as the double wall ring, are available to determine interfacial shear moduli. Both geometries in their measuring position on the interface are presented in Fig.1.23. The material functions need to be calculated in an iterative process to eliminate the bulk contribution and the double wall ring beats the bicone due to smaller *Bq* numbers. Data on interfacial shear elasticity acquainted with a double wall ring probe are presented in Chapter 5, however the investigated systems do not represent surfactant mono layers. Active and passive microrheological methods, i.e. tracking the forced or the Brownian motion of one or more colloidal probes at the interface, may be used to determine the rheological response as well as its spatial heterogeneity. However, interfacial macro- and microrheological data frequently differ by multiple orders of magnitude and further theoretical work is needed, considering local Marangoni flows and compressibility of the interfacial layer (Samaniuk and Vermant, 2014).

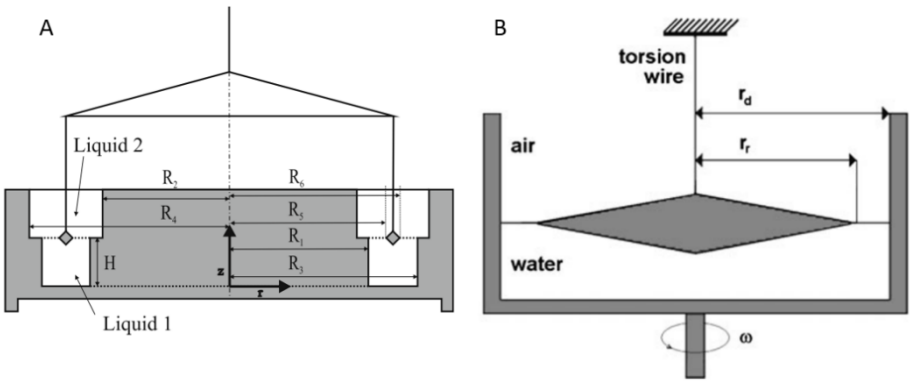

Figure 1.23: Schematic illustration of (A) a double wall ring geometry (Vandebril et al., 2010) and (B) a biconus for measurements of interfacial shear rheology using rotational rheometers (Miller et al., 2010)

The dilatational interfacial rheology is commonly determined using oscillating pendant drop or rising bubble tensiometers. Either the drop shape or the capillary pressure inside the drop is recorded during changes of the interfacial area. The oscillating drop methods was applied in the studies presented in Chapter 3, 4 and 5. The interfacial tension is often acquired using the Young-Laplace law which may not hold for all types of complex interfaces and the maximum frequency is restricted to several Hz. Limited to even lower frequencies is the longitudinal compression of planar interfaces in Langmiur-Pockls troughs, where shear and dilatation superimpose. For viscoelastic interfaces shear and dilatational contributions can be separated under some conditions by using two Wilhelmy plates. Transverse wave damping techniques, as the capillary wave method, use the dispersion relation and the power spectrum correlating with the damping to determine the rheology of the interface. (Fuller and Vermant, 2012)

2 High throughput object recognition and sizing in disperse systems

Full title: High throughput object recognition and sizing in disperse systems using an image processing tool based on template matching

Authors: Annika Ricarda Völp, Felix Fessler, Jasmin Reiner, Norbert Willenbacher

Status: published

Bibliografic data: Chemical Engineering & Technology, 2020, 43. Jg., Nr. 9, S. 1897-1902.

DOI: 10.1002/ceat.201900494

Size and shape of dispersed objects defines properties of suspensions, emulsions, and foams, such as stability, texture, and flow. Accordingly, a rational product design requires reliable size distribution analysis. This is particularly challenging in dense foams. An endoscopic setup was optimized for bubble imaging minimizing light re- flections, uneven illumination, and foam distortion. A software tool was developed detecting large quantities of foam bubbles at dispersed phase fractions up to 93% from images with spatially varying contrast within minutes based on the template matching algorithm. Reliability of the method is also illustrated for a bimodal glass bead mixture, anisotropic nanocrystals, and emulsion droplets during freezing.

2.1 Introduction

The analysis of the size distribution of objects in disperse systems is of particular interest e.g. for prediction of dispersion stability, texture and flow. The size distribution of the particles, gas bubbles or liquid droplets, can often be accessed by imaging technics, such as microscopy or endoscopy. Further analysis of size and shape requires fast and reliable detection of high quantities of particles on the images. Endoscopy combined with automated image analysis is well established for emulsions or bubbles produced in stirred vessels, the dispersed volume fraction in these studies, however, was below 45 % (Abidin et al., 2013; Bothe et al., 2017; Panckow et al., 2013, 2017). In foams, endoscopy is also appropriate for bubble size distribution analysis (Lexis and Willenbacher, 2014a; Xia et al., 2013), because it allows for in-situ observation of fragile foam structures and overcomes drawbacks of bubble observation through the container wall, e.g. capturing bubbles sheared or distorted at the wall. In food or personal care foams, however, the gas volume fraction is often higher than the maximum packing fraction of spheres (≈64 vol%), and spatially varying contrast, light reflections and bubble overlap on the images challenge automated bubble detection, especially when fast transient phenomena need to be monitored. Here we present an approach to determine the bubble size distribution inside densely packed foams combining endoscopic imaging and template matching image analysis. The endoscopic setup is optimized for imaging foams in backlight illumination with no need of filtering or post-processing if the template matching technique as described by Hofmann (Hofmann et al., 2015) and Zabulis (Zabulis et al., 2007) is used for particle detection and subsequent size distribution analysis. This technique has been implemented in a customized software tool and consists of the selection of a template inhering similarity with the particles on the image, screening of the image for sections with high similarity to the template (calculated using a zero normalized cross correlation (ZNCC)) and subsequent validation of the matches, as illustrated in Fig.2.1.

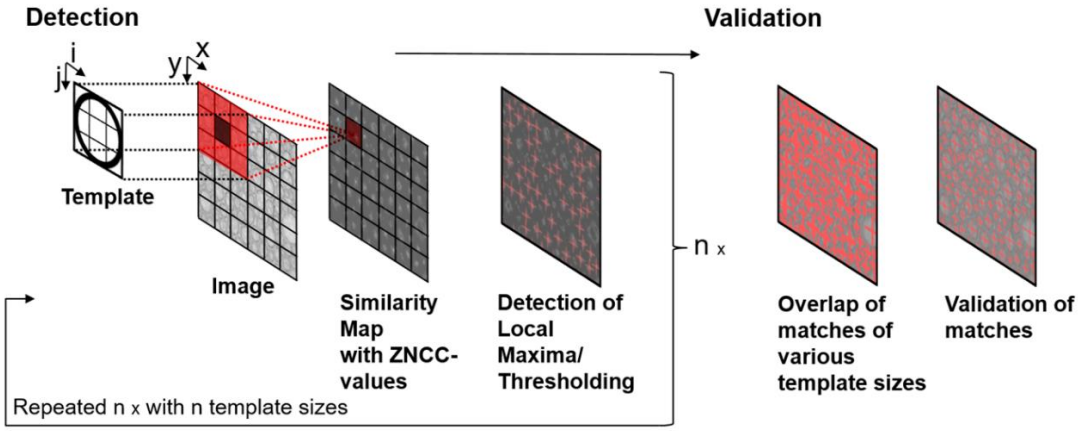

Figure 2.1: Scheme of template matching comprising detection and subsequent validation. A template is centered at each pixel position on an image and its similarity (zero normalized cross correlation value) stored in a similarity map. Local maxima on the similarity map are detected, filtered with a threshold, and positions and template size are stored in a matrix. This detection step is repeated for *n* template sizes. The validation step compares the matrices of all detections and filters for highest similarity values.

We illustrate the feasibility of the method, its reliability and accuracy analyzing the size distribution of two glass bead fractions and their bimodal mixture, selectively determining the size and number of crystalline and amorphous emulsion droplets during freezing, and analyzing the length and width distribution of rod-shaped nanocrystals on microscopic images, respectively. From endoscopic images, we finally record the time evolution of the average bubble size and size distribution width of a protein foam during drainage and aging.

2.2 Material and Methods

2.2.1 Image capturing

Fractions of glass beads (Spheriglass® 3000 and Spheriglass® 5000, Potters Industries LLC, Augusta, USA, fractionated in a customized up-current classifier) of 5 to 20 µm and 10 to 35 µm in diameter, respectively, as well as a 1:1 mixture of them were dispersed in acetone (20 wt% glass beads) and spread onto cover slips. After acetone evaporation, images of the particles on the cover slip were taken with an inverted bright field light microscope (Axio Observer D1, Carl Zeiss, Oberkochen, Germany) under 40fold magnification (Objective A-PLAN 40x /0.65, Carl Zeiss). Images of each glass bead fraction (depicting over 1000 beads) as well as an image of their mixture (depicting 440 beads) were analyzed. In parallel, both glass bead fractions and their mixture were diluted $1{:}10^5$ in 0.9 % sodium chloride solution and the size distributions were analyzed using Coulter counting (Coulter® Multisizer II, Beckman Coulter, Brea, USA).

Additionally, the size distributions of the particles were analyzed using laser diffraction (Helos, Sympatek, Clausthal-Zellerfeld, Germany) combined with a dry dispersion unit (Rodos, Sympatek).

An emulsion of 1 wt% hexadecane (Sigma-Aldrich, St. Louis, MO, USA) as dispersed phase, 1 wt% Tween® 20 (Carl-Roth, Karlsruhe, Germany) and 98 wt% Milli-Q water as continuous phase was prepared using a tooth-rim dispersing machine (IKA® T25 digital, ULTRA-TURRAX®, Staufen im Breisgau, Germany) at 2.2 m/s tangential speed (3200 rpm, 13 mm rotor diameter) at 28 °C for 10 min.

Emulsion imaging was performed using a customized polarizing microscope (Eclipse Ci-L, Nikon, Shinagawa, Tokyo, Japan) equipped with a temperature-controlled stage (LTS 420, Linkam Scientific, Tadworth, UK), 25 µl of emulsion were pipetted between two microscope cover slips placed on a tempered microscope object slide using a tempered pipette, then covered with a third cover slip and sealed at 28 °C. Droplet clusters were focused to depict as many droplets as possible. The sample was cooled from 28° to 0°C with a cooling rate of 10 K/min.

Images of the emulsion were recorded at 20°, 12°, 9°, 7.6°, 5° and 0°C and the size of liquid and crystalline drops was analyzed separately. Droplet size distribution was determined at T = 28°C, i.e. above the melting point of hexadecane, using a laser diffraction particle size analyzer (HORIBA LA-940, Retsch Technology, Haan, Germany) without further dilution of the emulsion.

Images of foam bubbles were captured using a non-flexible 295 mm long endoscope (TVS80.280.BF6.AD10.2x-Zoom, Visitool, Maulbronn, Germany) covered by an outer metal tube, 300 mm in length and 8.5 mm in diameter, closed with an optical glass disk (custom-made product, Visitool, Maulbronn, Germany). It was inserted into the foam prepared from 40 ml of 1 wt% bovine serum albumin solution which was foamed in a filter funnel (VitraPOR® glass filter Por.4, ROBU Glasfilter-Geraete GmbH, Hattert, Germany) purged with nitrogen. The endoscope was connected to a USB camera (Lumenera LU 160, Teledyne Lumenera, Ottawa, Kanada). Illumination was provided by a gooseneck light (KL 1500 LCD, Schott, Mainz, Germany) placed on the outside of the filter funnel wall. Three image sequences with a frame rate of 0.1 s^{-1} were recorded in freshly prepared foam and bubble size distributions were analyzed for each image, respectively.

2.2.2 Image analysis

Images of dispersed objects were analyzed with a software tool written in Matlab® (MathWorks®, Natick, USA). The scaling factor relating pixel number and dimension was determined manually by drawing a line along a defined distance on the images, i.e. a scaling bar, within the software tool. The ratio between the number of pixels spanned by that line and the defined distance was calculated. A binary, circular pixel pattern with a ring thickness of 10 % of its radius and a filled circle was generated within the software tool serving as screening templates for foam bubbles and emulsion droplets, respectively. Images of glass beads were screened using a similar template with a ring thickness of 20 %.

An image of rod-shaped nanocrystals was screened using an image section depicting a single crystal. The single crystal template was rotated in steps of 30° to cover the different orientations of the crystals on the image. The size range of the objects on the images was measured manually by drawing a line across the diameter of the biggest and the smallest glass bead, bubble or droplet respectively, within the software tool. The obtained limits were extended by 10 % to improve reliability. For the rod-shaped nanocrystals biggest and smallest diameter and length were measured likewise. The number of template sizes used for screening was chosen between 20 and 30 logarithmically distributed within the respective size range. The template was rescaled by the software as many times as chosen. The template of each size ($M \times N$ pixels) was then centered once at every pixel position (x,y) of the image ($P \times Q$ pixels) to be screened and the similarity between the pixel pattern of the template and the respective image section was calculated with the normalized cross correlation function

$$\boldsymbol{ZNCC}(\boldsymbol{x},\boldsymbol{y}) = \frac{\sum_{i}^{M-1}\sum_{j}^{N-1}[\boldsymbol{Template}(\boldsymbol{i},\boldsymbol{j})-\bar{\boldsymbol{T}}]*[\boldsymbol{Image}(\boldsymbol{x}-\boldsymbol{i},\boldsymbol{y}-\boldsymbol{j})-\bar{\boldsymbol{I}}_{\boldsymbol{x},\boldsymbol{y}}]}{\sqrt{\sum_{i}^{M-1}\sum_{j}^{N-1}[\boldsymbol{Template}(\boldsymbol{i},\boldsymbol{j})-\bar{\boldsymbol{T}}]^2 * \sum_{i}^{M-1}\sum_{j}^{N-1}[\boldsymbol{Image}(\boldsymbol{x}-\boldsymbol{i},\boldsymbol{y}-\boldsymbol{j})-\bar{\boldsymbol{I}}_{\boldsymbol{x},\boldsymbol{y}}]^2}}, \begin{matrix}-(\boldsymbol{P}-\boldsymbol{1}) \le \boldsymbol{x} \le \boldsymbol{M}-\boldsymbol{1} \\ -(\boldsymbol{Q}-\boldsymbol{1}) \le \boldsymbol{y} \le \boldsymbol{N}-\boldsymbol{1}\end{matrix} \quad (2.1)$$

where $Template(i,j)$ is the grey scale of template at position (i,j), $\bar{T}$ is the mean grey scale of the template, $Image(x-i, y-j)$ is the grey scale of image beneath the template position (i, j), and $\bar{I}_{x,y}$ is the mean grey scale of the image section beneath the template centered at (x,y). The zero mean normalized cross correlation is normalized to the range [-1; 1]. The value 0 corresponds to a complete mismatch, the value 1 to a perfect match and negative values correspond to an opposed match (negative of the template and image show the same pattern) (Diamond, 2011; Lewis, 1995).

The similarity value at each template position was stored in a matrix called similarity map. The detection step iteratively repeats with the selected number of templates. As a result, a stack of similarity maps was generated. Each similarity map was screened for local maxima (surpassing a specified threshold) using the LocalMaximaFinder Toolbox (FileExchange, Mathworks, Natick, USA). The positions of these local maxima in the similarity map corresponded to the positions in the image, where the algorithm detected an object.

After the detection step was completed for all template sizes a validation to filter overlapping detections was done. If the Euclidian distance between the centers of two matches was shorter than 80 % of the sum of their radii, the algorithm retained the location and template size of that showing the higher similarity value (Hofmann et al., 2015).

The results were presented as histograms and cumulative distributions of counts (q_0, Q_0), area (q_2, Q_2) and volume (q_3, Q_3), and characteristics as Sauter diameter d_{32}, median d_{50}, and

$$span=(d_{90}-d_{10})/d_{50}. \quad (2.2)$$

2.3 Results and Discussion

2.3.1 Bimodal size distribution of glass spheres

Fig.2.2 shows results of the size distribution analysis conducted for a mixture of spherical glass beads of two different sizes. The same analysis was conducted separately for both individual bead fractions. The distributions were compared to those obtained using Coulter counting (measuring objects sizes by changes of electric resistance when passing through a channel). Volume distributions obtained by both methods exhibit similar size ranges: from 5 to 20 µm and from 10 to 35 µm. The corresponding d_{50} values differ by max. 15 % (10.67 ±0.14 µm and 23.21 ±0.14 µm from Coulter counting, 9.9 ±0.1 µm and 23.0 ±0.1 µm from laser diffraction, as well as 9.4 ±1.6 µm and 19.7 ±4.2 µm from template matching). The bimodality is clearly visible in the volume distribution of the glass bead mixture with two peaks at 9.4 µm and 17.9 µm. Note, the Coulter counting method required a 1:10^{-5} dilution of of the suspension.

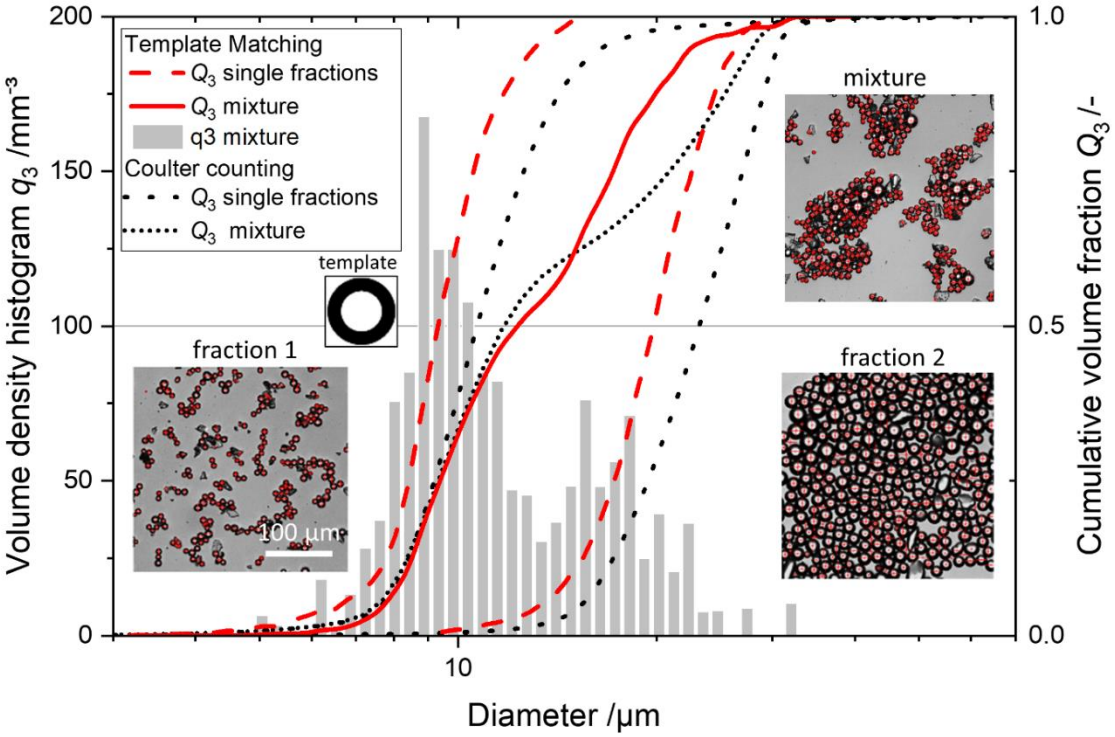

Figure 2.2: Volume density histogram q_3 (bars) and cumulative share Q_3 of a bimodal glass bead mixture analyzed using template matching (solid line) and cumulative share of the small (5-20 µm) and the big (10-35 µm) glass bead fraction combined in the mixture analyzed using template matching (dashed lines) and Coulter counting (dotted lines). Insets show analyzed micrographs of the small and the big glass bead fraction, as well as their mixture, and the template used for the analysis. Red crosses mark the glass bead detections.

2.3.2 Size distribution analysis of anisotropic nanocrystals

Fig.2.3A shows a transmission electron microscopy image of rod-shaped CdSe nanocrystals (Palencia et al., 2014) which was screened using template matching with an image section depicting a single nanocrystal (see inset). Red crosses show 850 detections of which only 9 are false. The detected length and width distributions of the crystals are shown in Fig.2.3B. The medians of 5.3 ±0.2 nm in width and 10.0 ±0.2 nm in length are in excellent agreement with the values 4.3 ±0.5 nm and 11.8 ±1.3 nm, respectively, stated in the image source and obtained via manual sizing. In this case commonly used laser diffraction (Merkus, 2009) or Coulter counting would only yield an equivalent sphere diameter strongly depending on the aspect ratio of the analyzed particles, which is only accessible from direct imaging.

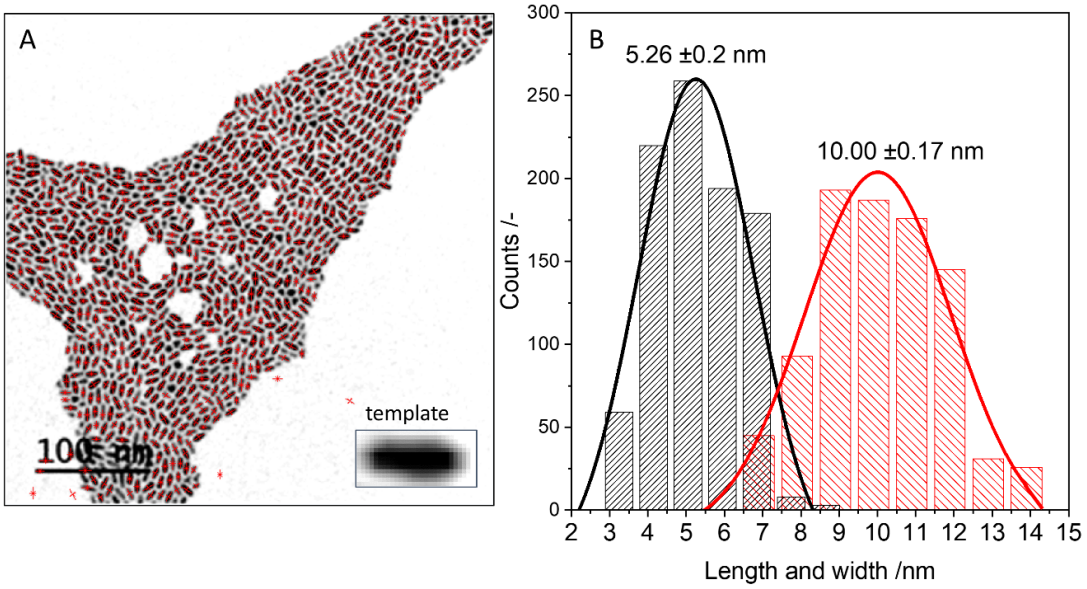

Figure 2.3: (A) Transmission electron micrograph of rod-like CdSe nanocrystals (image from Palencia et al. (Palencia et al., 2014) used under https://creativecommons.org/licenses/by/3.0/legalcode, contrast enhanced) analyzed using template matching with an image section used as template (inset). Red crosses show the detections. (B) Frequency distribution of diameter and length of CdSe nanocrystals in (A). Solid lines are Gaussian fits to the data.

2.3.3 Selective size distribution analysis of emulsion droplets during freezing

In this case, Coulter counting, diffraction or scattering experiments are not suitable because liquid and crystalline droplets cannot be distinguished, and furthermore the required dilution of the emulsion would affect the crystallization process (change in heat transfer and droplet collision frequency). However, in hexadecane/water emulsion, crystalline droplets can be distinguished from liquid droplets by their color in polarized light micrographs, as depicted in Fig.2.4A.

The crystalline droplets in the emulsion appear as closed black circles after blue filtration of the micrographs and were selectively detected with such a template, whereas the transparent liquid droplets match an empty circle. Red crosses in the blue filtered micrographs mark the detections and show the high selectivity of the template matching method. Fig.2.4B displays the fraction of crystalline droplet counts as a function of temperature obtained from the micrographs of a hexadecane/water emulsion during cooling down from 20°C to 0°C. Fig.2.4C shows the median volume weighted diameter d_{50} of liquid droplets and crystalline droplets, selectively, during this cooling process. The median diameter at 20°C obtained from template matching is 20.6 ±1.5 µm and agrees well with 20.5 ±0.2 µm from laser diffraction measurements. The median diameter decreases during cooling down from 20°C to 7.6°C. The crystallization starts at 12°C in droplets which are about 10 % bigger than the mean droplet size.

Droplets that stayed liquid down to 7.6°C are 10 % smaller than the average. Half of the droplets were crystallized at 8.7°C. Our image analysis tool allows for an in-situ monitoring of the crystallization kinetics in the dense emulsions.

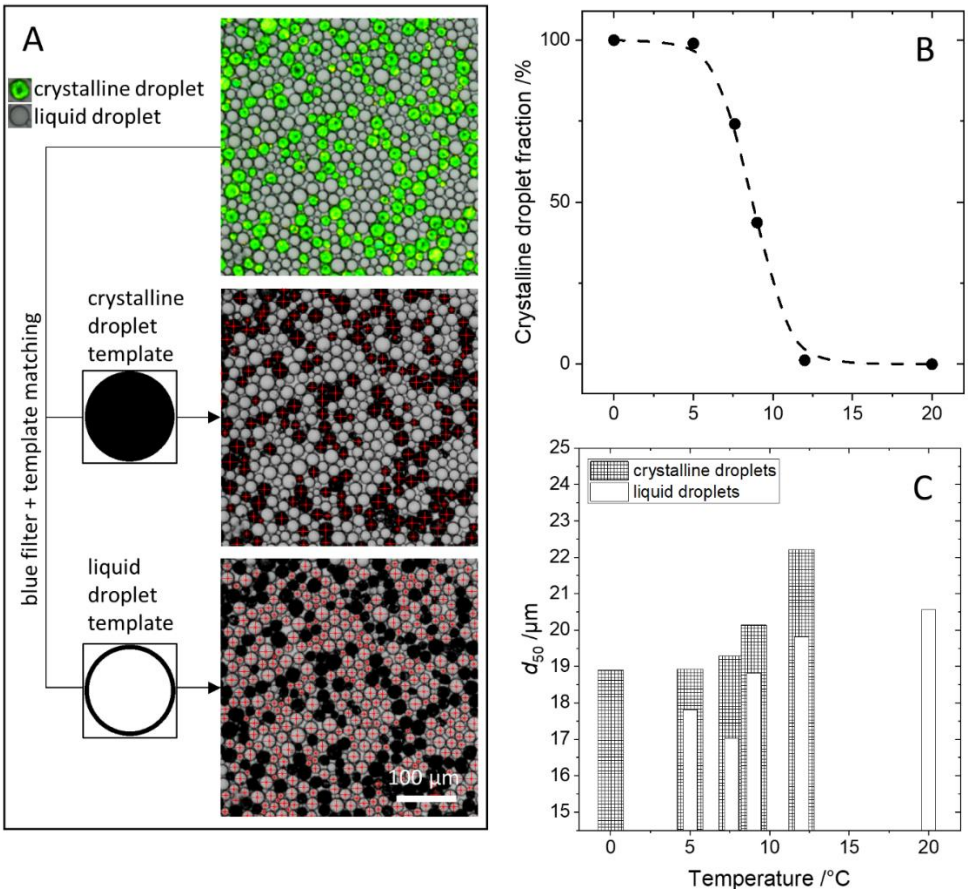

Figure 2.4: (A) Micrograph of a hexadecane/water emulsion under polarized light at 9°C and blue filtered copies after template matching analysis with a black circle template and a ring template. Red crosses mark detected droplets. (B) Crystalline droplet fraction versus temperature. (C) Median d_{50} of the volume distribution of crystalline droplets (shaded bars) and liquid emulsion droplets (hollow bars) versus temperature.

2.3.4 Bubble size distribution in foams

In this case the endoscopic images suffer from spatially varying brightness and contrast. The volume weighted density distribution q_3 and cumulative share Q_3 of bubbles in protein foams after 10 s and 400 s of drainage are shown in Fig.2.5A. Insets show endoscopic images of the foam which were analyzed manually by three individuals as well as by automated template matching with the depicted template. Red crosses mark the template matches and show high precision and yield of the detection. The distributions of the cumulative volume fraction acquired using template matching agree very well to those obtained manually. The temporal evolution of the mean Sauter diameter d_{32} and the distribution width characterized by the span of the bubble size distribution are shown in Fig.2.5B with a temporal resolution of 0.1 /s. The mean and standard deviation were derived from the analysis of three independently acquired image sequences of freshly prepared foam.

The Sauter diameter and the distribution span increase approximately linearly within the time range of 10 minutes after foam creation with an average standard deviation of 8 % and 17 %, respectively. Insets show sections of a bubble image captured at 200 s foam age analyzed using template matching (top) as well as Canny edge detection and subsequent Hough transformation (bottom) (Cao et al., 2008). Red crosses mark the detection and emphasize that more bubbles were detected with a higher accuracy using template matching without preprocessing of the heterogeneously illuminated image.

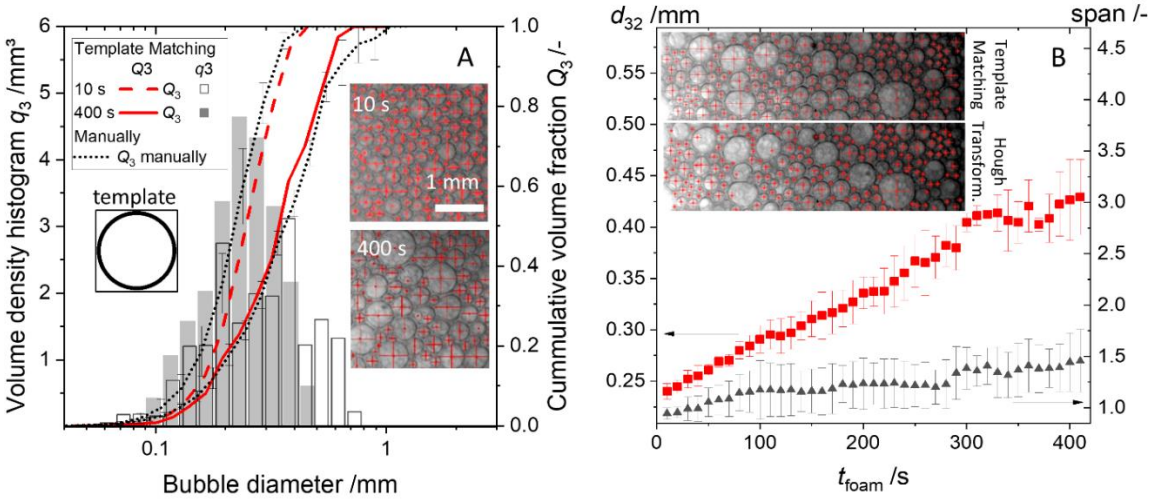

Figure 2.5: (A) Volume density histogram q_3 (bars) and cumulative share Q_3 analyzed manually (dotted lines) as well as by applying template matching on bubble images of protein foam after 10 s (dashed line) and 400 s (solid line) of free drainage, respectively. Insets show corresponding bubble images and the template used for template matching analysis. Red crosses mark the bubble detections. (B) Mean Sauter bubble diameter d_{32} (squares) and q_3 distribution span $(d_{90}-d_{10})/d_{50}$ (triangles) versus age of protein foam t_{foam}. Insets show image sections depicting bubbles after 200 s foam aging analyzed using template matching and Canny edge detection combined with Hough transformation with red crosses marking the detections, respectively.

2.4 Conclusion

We have applied simple ZNCC-based template matching in a software tool for high throughput size distribution analysis of bubbles, captured with an in-situ endoscopic setup in foams at dispersed volume fractions up to 90%. It provides fast detection of large quantities of particles, i.e. approx. 500 per minute, with high geometric selectivity without previous image processing. We have demonstrated that the results of the software tool can compete with time and cost consumptive methods such as manual counting, Coulter counting or laser diffraction and sizes particles, droplets and bubbles in micro- or endoscopic images with great accuracy. The method does not require dilution and can be used to distinguish between different particle types, and it allows for size detection of anisotropic particles in two dimensions. The template matching approach is especially useful for analysis of endoscopic images with poor and heterogeneous contrast where thresholding, edge detection and Hough transformation fails. The high time resolution of the size distribution analysis using template matching is particularly suitable for capturing fast transient phenomena in situ.

3 In-situ characterization of milk foams in a commercial foaming device

Full title: In-situ rheological and structural characterization of milk foams in a commercial foaming device

Authors: Annika Ricarda Völp, Jan Engmann, Deniz Zeynel Gunes, Cécile Gehin-Deval, Norbert Willenbacher

Status: published

Bibliografic data: Journal of Food Engineering 290 (2021): 110150.

DOI: 10.1016/j.jfoodeng.2020.110150

Processing, stability and sensorial perception of food foams are tightly related to their microstructure and flow behavior. Characterization of corresponding physical parameters is central for product development and quality control. An experimental setup enabling in-situ characterization of yield stress, gas volume fraction and bubble size distribution at different heights within a foam column created in a commercial whipping device is presented. Reliable determination of these quantities is shown. Foams made from regular and reconstituted milk have been investigated. Gas volume fraction and bubble size increase monotonically during free drainage. Related to the changes in these parameters, the yield stress increases strongly during initial drainage and weaker in mature foams. Gradients of the structural and rheological parameters along the direction of gravity increase over time. Yield stresses in these milk foams are significantly higher than predicted from phenomenological modelling including the above parameters and we attribute this to interfacial elasticity contributions.

3.1 Introduction

Coffee is the most popular hot beverage among Europeans, who consume about 2.5 million kg coffee beans annually (ICO, n.d.). Milk foam is added to every second coffee served in German and Austrian gastronomy (AMA Marketing, n.d.; Statista, n.d.). Latte and cappuccino varieties are also the most popular coffee products purchased in the UK (Worldpanel, n.d.). The variety of coffee specialties based on milk foams has long gone beyond cappuccino and latte macchiato, and new coffee trends for instance in latte art, the creation of decorative patterns by pouring microfoam into coffee, push the development of foaming devices and recipes for foaming solutions based on dairy products or vegan replacements. Milk based food foam products with a broad range of rheological behavior are available serving manifold applications and ideally providing pleasant texture perception. Tailoring their stability and flow behavior remains a challenge for the food industry (Gunes D. Z., Engmann J., Gehin-Deval C., Schmitt C., 2018). The flow behavior is strongly related to micro-structural properties, mainly bubble size distribution and gas volume fraction, which are often subject to local inhomogeneity within a foam column and difficult to predict for complex food systems.

In foams under gravity, a vertical gradient in gas volume fraction develops due to drainage of the liquid fraction. The gas volume fraction can range between almost 100 % at the foam top and less than 64 % at the foam bottom. The latter is the critical gas volume fraction of random close packing of monodisperse, spherical bubbles. For polydisperse bubble size distributions, this critical gas volume fraction is higher (Farr and Groot, 2009; Lexis and Willenbacher, 2014a). Below the critical packing fraction, foams behave like purely viscous fluids unless there are attractive interactions among the species stabilizing the bubble interfaces (Cohen-Addad and Höhler, 2014; Saint-Jalmes and Durian, 1999). Foams with gas volume fraction exceeding the critical volume fraction exhibit elastic behavior under small shear stresses and a critical stress, also termed yield stress, at which bubble rearrangements enable onset of foam flow. For complex fluids such as milk foams, the true deformation field within a sample is often not known. The critical stress at which the apparent deformation or flow rate in a rheometer increases drastically is called apparent yield stress.

The elastic modulus and the yield stress scale with the “Laplace pressure” inside the bubbles, given by the ratio between surface tension and the Sauter bubble radius, the foams gas volume fraction and the maximum packing fraction referring to the particular bubble size distribution (Marze et al., 2005; Mason et al., 1996). A vertical gradient in gas volume fraction develops with foam age and as a consequence, coalescence and hence the bubble size distribution alters along the vertical axis. These structural changes also result in a gradient of foam rheological properties within the foam column. To characterize the spatial and temporal changes of foam structure and rheology, a methodology allowing for unperturbed foam aging and in-situ characterization is needed.

We have developed an experimental setup, which allows for the characterization of milk foam rheological and micro-structural properties at different heights along a foam column within a commercial whipper. The cylindrical container with eccentric whipping coil and heating plate at the bottom is built into a rotational rheometer.

Yield stresses are measured with a vane rotor at regular intervals along the rotational axis of the container. Bubble size distributions are analyzed via endoscopic imaging and automated bubble detection at the same heights with temporal resolution on the order of seconds. Gas volume fractions are obtained from electrical conductivity measurements. Brass rings at the inner container wall and a height adjustable ring submerged into the foam serve as electrodes to detect the conductivity at intervals along the vertical axis.

Results presented for different types of milk foams confirm the feasibility of the device, provide some new insight regarding micro-structure and flow of such foams and may contribute to design optimization of commercial food foaming devices.

3.2 Materials and Methods

3.2.1 Modification of the foaming device

Fig.3.1 shows the setup developed for the in-situ characterization of the milk foams. It consists of a modified commercial milk foamer (Nespresso Aeroccino 4, Nespresso S.A., Lausanne, Switzerland), an acrylic glass tube fitted with conductivity electrodes, an endoscope and a vane rotor.

The top of a commercial milk foamer consisting of a pourer and a handle was replaced by an acrylic glass tube (Evonik Plexiglass, 100 mm height, 80 mm outer diameter, 74 mm inner diameter). Customized brass rings (1 mm height, 76 mm outer diameter, 74 mm inner diameter) were flush-mounted to the inner wall of the acrylic glass tube at 28, 38, 48 and 58 mm height (with respective 1 mm holes for electrode connections at each height). Another customized brass ring (1 mm height, 69 mm outer diameter, 67 mm inner diameter) was fixed to a tripod holder (3D printed, 100 mm height, 73 mm outer diameter, 67 mm inner diameter, co-polyester based material: Colorfab xt, Belfeld, Netherlands). The tripod holder was designed to place the brass ring at the heights of 28, 38, 48 and 58 mm, opposite to the brass rings mounted in the acrylic glass tube. This allowed for measuring the foam conductivity at four different heights inside the foamer. To conduct the rheometric measurements, the foamer was centered into a rheometer mounting plate using an annular spring clamp (Ringfeder, RfN 8006, 8 cm inner diameter). A four bladed vane of 36 mm in diameter and 9 mm in height, was manufactured for measuring foam yield stress.

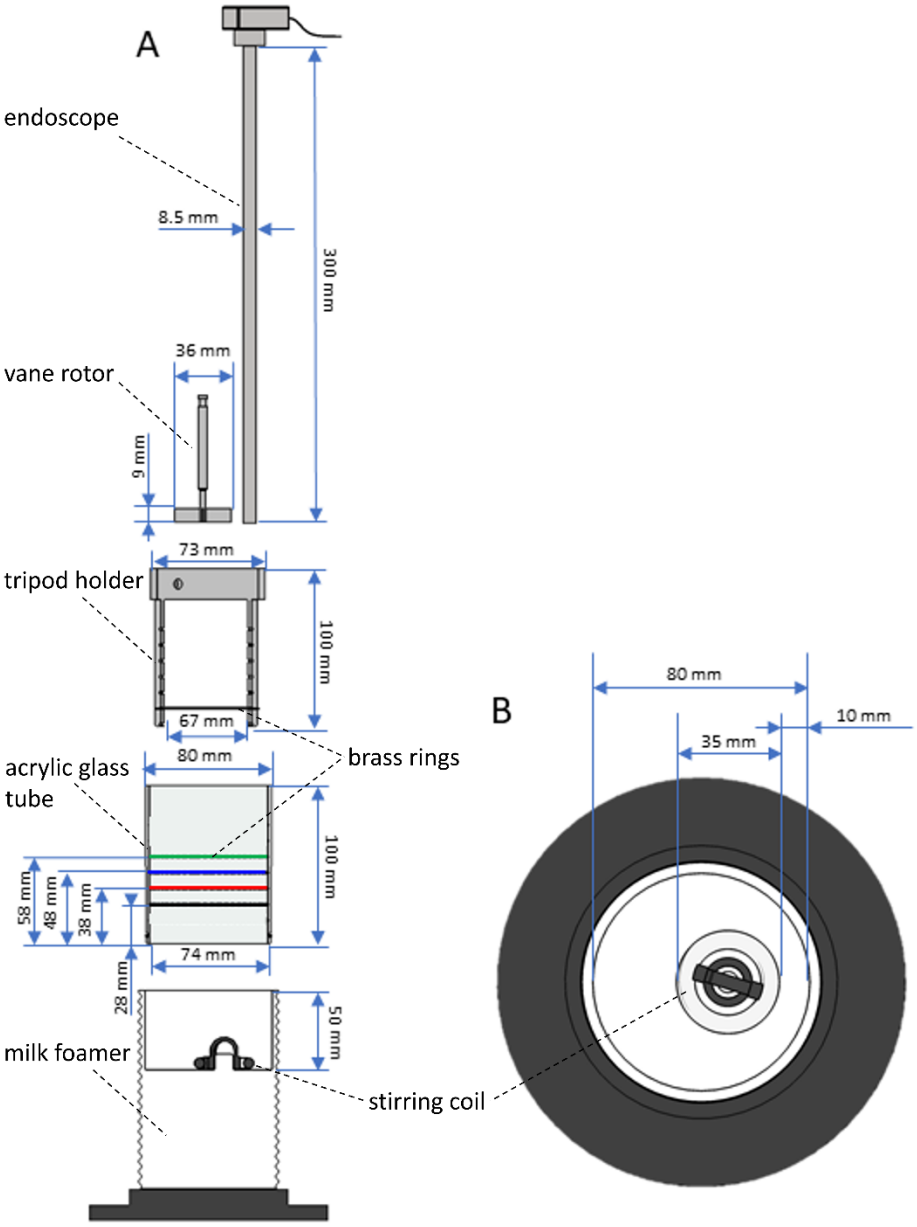

Figure 3.1: Modified commercial milk foamer (Nespresso Aeroccino4) for in-situ determination of gas volume fraction, yield stress and bubble size at various foam heights in side view (A) and top view (B) of the foamer.

3.2.2 Sample preparation

Reconstituted milk was prepared by dispersing 15 g of a commercial produced milk powder (provided via Nestlé Research, Switzerland) in 120 ml of mineral water (Vittel® containing 255.7 mg/L monovalent ions and 234 mg/L divalent ions, Nestlé, Switzerland) during stirring for 70 to 80 seconds. An amount of 120 ml of either ultra-high temperature processed (UHT) whole milk (Alpenmich, haltbar, 3.5 % Fett, Alnatura, Bickenbach, Germany), fat reduced UHT milk (Alpenmich, haltbar, 1.5 % Fett, Alnatura, Bickenbach, Germany) or reconstituted milk at room temperature was filled into the foamer. The milk was whipped using the stirring coil eccentrically placed at the bottom of the foamer as depicted in Fig.3.1B. During whipping, the temperature was increased with a rate of 0.6 °C/s via heating through the bottom of the foamer's cell.

The foaming process stopped after approximately 70 seconds when the temperature of the milk at the bottom had reached 60 °C. All measurements started after the foaming process had stopped. The nutrition information of the UHT milk and the solution of 12.5 % milk powder, as specified by the manufacturer, and the surface tension measured as described in section 2.3 are given in Table 3.1.

Table 3.1: Compositional information (in weight %) and surface tension of whole milk, fat reduced milk and reconstituted milk made of 12.5 % milk powder

	UHT whole milk	UHT fat reduces milk	12.5 % reconstituted milk
Fat	3.6 %	1.6 %	3.6 %
Carbohydrates	5 %	5.1 %	3.2 %
Proteins	3.3 %	3.4 %	3.4 %
Salt	0.11 %	0.11 %	-
Surface tension	45.3 ±0.1 mN/m	45.5 ±0.2 mN/m	45.8 ±0.6 mN/m

3.2.3 Surface tension determined using de Noüy ring

The surface tension σ of the milk samples was determined using a tensiometer (DCAT11, DataPhysics Instruments) equipped with a platinum de Noüy ring (RG 11 - Du Noüy ring, DataPhysics Instruments, Filderstadt, Germany) with 25 mm height, 18.7 mm diameter and, 0.37 mm wire thickness (Lykema, J., Fleer, G. J., Kleijn, J. M., Leermakers, F. A. M., Norde, W., & Van Vliet, 2000).

3.2.4 Bubble size distribution determined using endoscopy

A non-flexible 295 mm long endoscope (TVS80.280.BF6.AD10.2x-Zoom, Visitool, Maulbronn, Germany) with a diameter of 8 mm was covered by an outer metal tube, 300 mm in length and 8.5 mm in diameter, closed with an optical glass disk (custom-made product, Visitool, Maulbronn, Germany) and was connected to a USB camera (Lumenera LU 160, Teledyne Lumenera, Ottawa, Kanada). The size to pixel ratio was determined by scaling the image of millimeter scaling paper held flat onto the glass disk of the endoscope covering tube. Subsequently, the endoscope was placed into the foamer with a distance to the bottom wall of 28, 38, 48 or 58 mm. The light outlets of a two-branched gooseneck lamp (KL 1500 LCD, Schott, Mainz, Germany) were placed inside the foamer pointing from opposite sites into the direction of the endoscope tip. The foamer was filled with 120 ml of sample and the foaming process was started. Once the foam covered the endoscope tip, the light intensity was adjusted between 0 and 600 lm to obtain even illumination of the foam. Images were recorded every 10 seconds starting immediately after the foaming process stopped. The images were analyzed using a template matching tool written in MATLAB® (Mathworks, Natick, USA) with 25 circular templates differing in diameter as described elsewhere (Völp et al., 2020a). The diameters were logarithmically distributed in the range between 10 and 250 pixels. The frequency density distribution histogram and the cumulative distribution of the bubble diameter counts and volumes were calculated from the obtained bubble size lists based on the 25 size classes. The span of the count distribution $(d_{90}-d_{10})/d_{50}$ and the Sauter radius R_{32} were calculated from the size distribution. All measurements were repeated at least three times with freshly prepared foams. The average and standard deviation of the counts and volumes for each size class, the span and the Sauter radius were calculated from bubble sizes lists deriving from three images of independently prepared foams at the same age. For validation of the automated bubble detection, the sum of all bubbles in three images of independently created foams, recorded after 300 seconds of drainage were additionally analyzed manually by three individuals who measured the bubble diameters. The bubble diameter counts and volumes for the same 25 size classes as above were obtained and their average and standard deviation referring to the analysis of the three individuals were calculated.

3.2.5 Gas volume fraction determined using electrical conductivity measurements

The conductivity κ of the foams between brass rings at the inner wall of the foamer with a distance to the bottom of 28, 38, 48 and 58 mm and the height adjustable ring with 5 mm smaller radius was measured and recorded using an LCR meter (U1733C 20,000-Count-Display Handheld LCR Meter, Keysight Technologies, Santa Rosa, USA) with a test frequency set to 1 kHz. Beforehand, the setup was calibrated using potassium chloride solutions with conductivities between 10 and 10 000 µS/cm at 20°C. A cell-constant of 0.07 /cm was determined.

Using this cell-constant, the conductivities of potassium chloride solutions between 10^{-4} and 0.1 mol/l a measured with the ring setup agreed reasonably with the conductivities measured using a commercial conductivity meter (S230 seven compact, Mettler Toledo, Schwerzenbach, Schweiz) equipped with a four-electrode conductivity sensor (Inlab® 738 ISM, Mettler Toledo, Schwerzenbach, Schweiz), as shown in Fig.3.A1.

Before foaming, the inner ring was placed at the height of interest opposite the outer ring and the LCR meter was connected to the copper cables attached to the brass rings. The foamer was filled with 120 ml of sample and the foaming process was started. The conductivity was measured immediately after the foaming process stopped and repeated at least three times with independently produced foam samples. For comparison, the conductivity was measured using the commercial conductivity probe equipped with a temperature sensor. The conductivity sensor of the commercial probe was placed in the foamer with a distance to the bottom wall of 28, 38, 48 and 58 cm, respectively. Conductivity and temperature were recorded every 10 seconds.

The foam gas volume fraction φ was calculated using following empirical correlation (Feitosa et al., 2005a): $\varphi = 1 - (3\,\kappa_{rel.} + 33\,\kappa_{rel}) / (1 + 25\,\kappa_{rel} + 10\,\kappa_{rel}^2)$ (3.1)

where κ_{rel} is the foam conductivity relative to the milk conductivity at 25°C, respectively

$$\kappa_{rel.} = \kappa_{foam}(25°C) / \kappa_{milk}(25°C) \quad (3.2)$$

Beforehand, the foam conductivity at 25°C, $\kappa_{foam}(25°C)$, was calculated from the conductivity measured at temperature T using a linear temperature correction (Zhang, 2007):

$$\kappa(25°C) = \kappa_{foam}(T) / (1 - \alpha(25° - T)) \quad (3.3)$$

where $\kappa_{foam}(T)$ is the foam conductivity at the foam temperature T and α is the temperature correction factor. The conductivity and temperature of the milk sample was measured during temperature decay to room temperature to obtain α from the slope of the milk conductivity versus temperature $\Delta\kappa_{milk}/\Delta T$ and the milk conductivity at 25°C, $\kappa_{milk}(25°C)$:

$$\alpha = (\Delta\kappa_{milk}/\Delta T) / \kappa_{milk}(25°C) \quad (3.4)$$

For comparison, the gas volume fraction was also determined from volumetric measurements. The entire content of the foamer was poured into a measuring cylinder of 250 ml capacity directly after foaming 120 ml of milk. The volume of the foam V_{foam} and the drained milk V_{milk} was captured at 15, 30, 60, 120, 180, 240, 300 and 600 seconds of foam age. The gas volume fraction was calculated as follows:

$$\varphi = 1 - (120\ ml - V_{milk}) / V_{foam} \quad (3.5)$$

3.2.6 Foams' yield stress determined using a vane rheometer

A rotational rheometer (Mars II, Haake Thermo Fisher Scientific, Karlsruhe, Germany) with an in-house manufactured, four bladed vane rotor (36 mm diameter, 9 mm height) and the foamer built into the rheometer as measuring cup was used. For yield stress measurements, the foam samples were prepared in the foamer. Then the vane geometry was lowered to the measuring position in the foam. The measurement was started when the foam reached the desired foam age. For reference, a rotational rheometer (Rheoscope1, Haake Thermo Fisher Scientific, Karlsruhe, Germany) and a plate-plate geometry 60 mm in diameter was used. Bottom plate and rotor plate were covered with sandpaper (grit 40, average particle diameter 269 µm) to reduce wall slip effects. The required foam volume was approximately 20 ml. The gap height was set to 6 mm. A foam sample was prepared inside the foamer. A scoop of foam was withdrawn from the foamer using a spoon and was put onto the bottom plate 20 seconds before it reached the desired foam age and the measurement was immediately started. The device set the gap automatically within 20 seconds.

In both cases, shear stress σ was increased from 0.1 to 50 Pa in 12 logarithmically distributed steps during a total measuring time of 60 s. The measurement was repeated at least three times with freshly prepared foam samples. The recorded deformation γ was plotted versus shear stress logarithmically and the yield stress τ_y was determined using the tangent intersection point method as described elsewhere (Lexis and Willenbacher, 2018).

For validation of the measurements using the in-house manufactured vane, the yield stresses of commercial o/w- and w/o- emulsion (Nivea Soft and Nivea Body Milk, Beiersdorf, Hamburg, Germany) were measured with the vane geometry and with a plate-plate geometry (60 mm in diameter covered with sand paper and 5 mm gap height). After the measuring positions of the vane rotor or upper plate was set, samples were left to rest for at least 15 min before measurements started. Shear stress was increased stepwise between 5 and 500 Pa in 20 logarithmically distributed steps for the o/w-emulsion and between 1 and 20 Pa in 15 logarithmically distributed steps for the w/o-emulsion solution. Measurements were repeated three times with every emulsion, respectively.

3.3 Results and discussion

3.3.1 Validation and performance of the foam characterization methods

Endoscopic foam images were analyzed to obtain the bubble size distribution. The images were acquired in the center of the milk foamer to avoid capturing bubbles distorted at the container wall. To validate the automated bubble size distribution approach, images of three milk foams at 85 % gas volume fraction were recorded and analyzed both manually and using the template matching tool. During the manual data evaluation, approximately 700 bubbles in three images were analyzed by three individuals. Then, each image was analyzed using template matching. Fig.3.2 shows an exemplary endoscopic image of the foam, wherein red crosses highlight the automatically detected bubbles. Fig.3.2 also shows a comparison of the frequency density histograms and cumulative volume distributions obtained from manual analysis and template matching method, respectively. The automated analysis delivers the same results as the manual analysis up to a cumulative volume of 90 %. The deviation above this value is caused by the fact that bubbles with diameters above 680 µm were not detected using the template matching method because of their lack in sphericity. These bubbles, however, were included in the manual analysis.

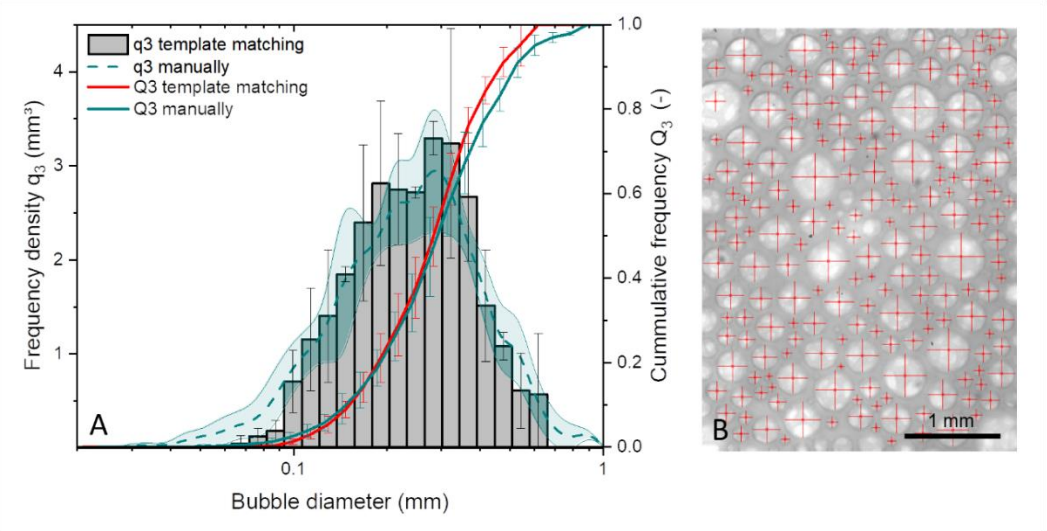

Figure 3.2: Bubble size frequency density histogram and cumulative frequency distribution of bubble volumes analyzed using an automated template matching code (grey bars and solid red line) and manually by three individuals (dashed and solid green line) in endoscopic images of 12.5 % reconstituted milk foam at 85 % gas volume fraction (A). Red crosses mark the automatically detected bubble diameters in one of three images analyzed (B).

In-situ electrical conductivity measurements were performed at different heights within the foaming cell using brass ring electrodes as described above. Fig.3.3 shows the time evolution of the gas volume fraction of a milk foam determined from conductivity measurements at different heights and compares them to those measured using a commercial conductivity sensor positioned at the same height. The foam gas volume fraction obtained with the ring electrodes are shifted to slightly lower values than obtained using the commercial conductivity sensor at 38 mm and 58 mm height inside the foamer. This systematic deviation is somewhat more pronounced at the height of 28 mm since it increases with increasing absolute value of conductivity and it is also found in simple salt solutions (Fig.3.A1). Despite the systematic deviations regarding the absolute gas volume fraction values, the time evolution captured with both methods is similar at all investigated foam heights. In the upper foam regions, drainage results in a monotonic increase of the gas volume fraction over time. However, close to the foam bottom at a height of 28 mm, the gas volume fraction goes through a maximum and then drastically decreases because of accumulation of drained liquid. The conductivity obtained with the commercial conductivity sensor tends to scatter in the dry limit of the foam resulting in unsteady gas volume fraction as seen for instance at the foam top, at 58 mm height, after 300 seconds foam age. Because of a ten times higher gap volume, the developed ring electrode setup seems to provide more robust conductivity measurements and hence more reliable gas volume fraction data. Finally, Fig.3.3 also shows the time dependence of the volumetrically determined average gas volume fraction. These values lie in the same range as the in situ determined values in the middle of the foam column and exhibit the expected drainage-induced monotonic increase of the gas volume fraction over time.

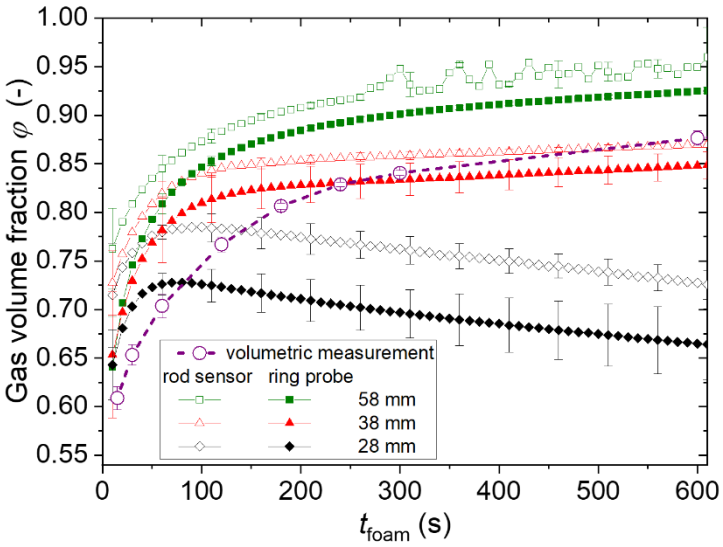

Figure 3.3: Gas volume fraction φ versus foam age t_{foam} for 3.6 % fat UHT milk foam measured in situ with commercial conductivity sensor (empty symbols) and brass ring electrodes (filled symbols) at three different heights inside the foaming device. Gas volume fraction of the entire foam, determined measuring ex-situ volumes of foam and drained milk, are also shown for comparison (open circles).

Yield stresses τ_y of commercial o/w- and w/o- emulsions (Nivea Soft and Nivea Body Milk, Beiersdorf, Hamburg, Germany) measured with our customized vane geometry were validated using a rheometer equipped with a plate-plate geometry. Comparison of the corresponding data given in Table 3.2 demonstrates that the yield stress values measured using the short vane customized for in-situ foam characterization agree very well with those determined using the plate-plate geometry as well as with literature data.

Table 3.2: Yield stress values of commercial emulsions obtained from vane and plate-plate rheometry, and literature

Yield stress from	Vane	Plate-plate	Literature (Martinie et al., 2013)
o/w-emulsion Nivea Body Milk	10.9 ± 0.5 Pa	12.2 ± 0.7 Pa	8 Pa
w/o-emulsion Nivea Soft	91.0 ± 9 Pa	98.0 ± 18 Pa	91 Pa

The in-situ method allows the foams' yield stress to be measured along the vertical axis of the foamer with a resolution of 1 cm. Fig.3.4 shows the time evolution of the yield stress during aging measured in situ at different heights directly inside the foamer and corresponding ex-situ values obtained using the plate-plate geometry. For all heights, the yield stress increases within the first 300 seconds and levels off to plateaus later on. The plateau value increases with height inside the foam column. These measurements exhibit a relative standard deviation of maximum 10 %. Thus, the yield stress gradient within the foam can be well resolved using the in-situ measurement with the vane rotor. For measuring the yield stress ex situ with plate-plate geometry, as described earlier (Lexis and Willenbacher, 2014a), approx. 20 ml of foam were transferred from the foamer into the fixture. As can be seen from Fig.3.4, the value obtained for the yield stress from plate-plate rheometry agrees with data obtained in situ using the vane geometry only for young foams within the first minutes after their preparation. For older foams, yield stress values obtained using plate-plate geometry are at least three times higher than those determined in situ.

Since deviations between yield stress data obtained using the customized short vane geometry and the commercial plate-plate fixture occur only in foams and not in commercial o/w- and w/o-emulsions (Table 3.2), we conclude that the latter data have a significant systematic error and we attribute this to the compression of the foam during gap setting. In young foams with low gas volume fraction, the compression does not lead to a significant change in bubble packing, presumably due to its narrow size distribution. Hence, no increase of the yield stress compared to the values obtained with the less invasive vane rotor were observed.

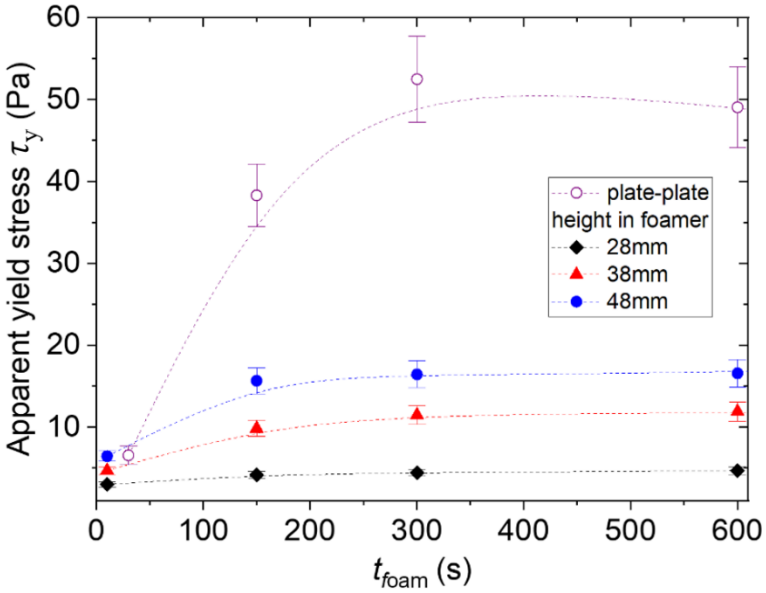

Figure 3.4: Apparent yield stress τ_y versus foam age t_{foam} for 3.6% fat UHT milk foam measured ex situ with a plate-plate rheometer (empty symbols) and in situ with a vane rotor at three different heights inside the foaming device (filled symbols). Lines guide the eye.

3.3.2 Structure and rheology of milk foams

We have used the experimental setup described and validated above to investigate the time evolution of the yield stress, gas volume fraction and bubble size distribution at different heights within the foam column created using the commercial whipper with its defined coil rotational speed and heating profile. Measurements have been performed for UHT whole milk, UHT fat reduced and reconstituted milk (see Chapter 3.2.1).

The time evolution of levels of the milk/ foam- interface (filled symbols) and the foam/ air-interface (open symbols) inside the foamer for reconstituted and for UHT milk with 1.6 % fat and 3.6 % fat is shown in Fig.3.5. The foam volume is specific to the respective milk types and the foaming device used here, and was smallest in the case of 1.6% fat UHT milk. The foam collapse rates, seen in the decay of the upper foam limit, are similar for all foams investigated. The volume of non-foamed milk below the foam layer is initially highest after whipping 1.6% fat UHT milk and lowest after whipping 3.6 % fat UHT milk. With ongoing drainage, the height of non-foamed milk approaches 25 mm inside the foamer (corresponding to a volume of 100 ml) in all cases. Measurements in the foam were restricted to a maximum foam age at which the upper or lower limit of foam height still exceeded the fixed measurement heights. Furthermore, the distance between the fixed measuring positions and the milk/ foam- and foam/ air- interface is not constant. In the following, the temporal and spatial changes of structural characteristic as well as rheological foam properties obtained for reconstituted milk will be discussed.

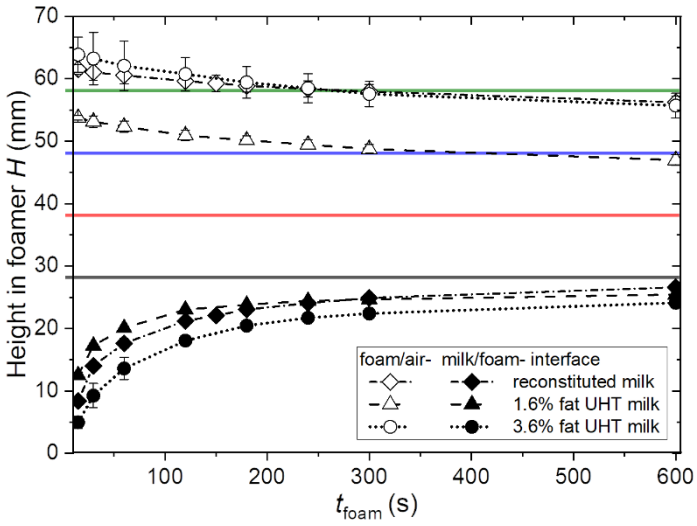

Figure 3.5: Levels of milk/ foam- interface (filled symbols) and foam/ air- interface (open symbols) inside the foamer after whipping of reconstituted milk (diamonds), 1.6 % fat UHT milk (triangles) and 3.6 % UHT milk (circles) versus foam age t_{foam}. Dotted and dashed lines guide the eye. Positions of the measuring probes are displayed as solid lines.

The mean radius R_{32} (Fig.3.6A) varies initially between 200 µm and 300 µm, about double the bubble size of foams produced by steam injection (Jimenez-Junca et al., 2015, 2011), and monotonically increases over time. The average bubble size in foams was found to scale with the square root of foam age in previous studies (Durian et al., 1991; Lambert et al., 2010) as expected considering coarsening as a result of statistically-independent bubble coalescence events preserving the fractal structure of the foam. However, a linear increase of bubble size with the foam age, as seen here for milk foams, had been reported also for foams from β-lactoglobulin solutions (Rami-shojaei et al., 2009). The increase in mean radius is more pronounced in the upper regions of the foam in the present study and the slope dR_{32}/dt_{foam} varies between 3.7 µm/min at the bottom and 22 µm/min at the top of the foam. This difference may be attributed to more frequent bubble coalescence and enhanced Ostwald ripening due to thinner foam lamellae in the upper foam regions. Note, that no R_{32} data are available for the upper foam regions for long aging times due to an overall shrinkage of foam volume. Fig.3.6B displays the change of R_{32} in axial direction. Bubble size always increases with increasing height in foam and this gradient increases over foam age, which is in good agreement with the bubble size growth versus height and time previously found in free drainage experiments (Vera and Durian, 2002).

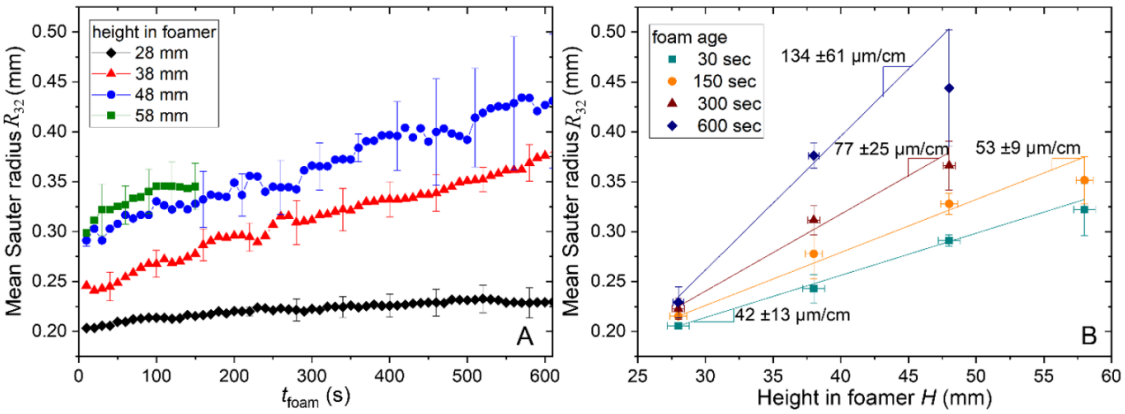

Figure 3.6 : Mean Sauter radius R_{32} of reconstituted milk foam versus foam age t_{foam} measured at four different heights inside the foaming device (A) and versus height inside the foam H at four different foam ages (B). Lines in B are linear fits to the data.

As shown in Fig.3.7, the width of the bubble size distribution as characterized by the span = $(d_{90}-d_{10})/d_{50}$ increases during foam aging, similar as the mean radius R_{32}. But no difference in span along the foam column height was observed above 28 mm height within the foamer. The spatial and temporal changes in bubble size documented here mainly characterize the coalescence process of a foam created from a certain type of milk using this particular whipping device.

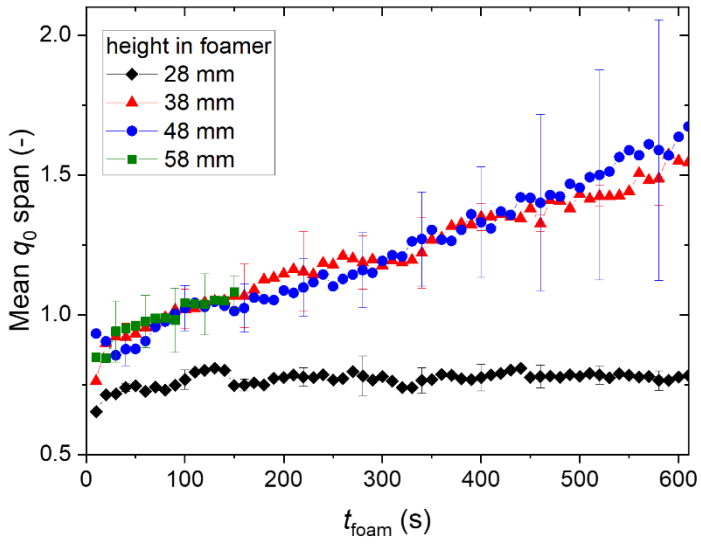

Figure 3.7: Mean span $(d_{90}-d_{10})/d_{50}$ of the q_0 bubble size distribution of reconstituted milk foam versus foam age t_{foam} measured at four different heights inside the foaming device.

Fig.3.8A shows the evolution of the gas volume fraction φ at different heights within the column during foam aging. At all heights, a strong initial growth of φ is observed. In the upper regions of the foam, this turns into a weak linear increase at longer times. However, close to the bottom of the foam, $\varphi(t_{foam})$ goes through a maximum and then decreases and, at all times, the gas volume fraction remains below the critical gas volume fraction φ_c at which the maximum packing fraction of spherical bubbles is reached and they start to deform. For randomly packed monodisperse spheres φ_c = 0.635. This is a consequence of a rising liquid level underneath the foam due to drainage as schematically depicted in Fig.3.5. As a consequence, the lowest measuring height in our setup here corresponds to the transition region between liquid and foam at long aging times.

For the reconstituted milk foam investigated here, liquid fraction versus drainage time followed a power law $(1\text{-}\varphi) \propto t^n$ and the exponent n increases from -0.1 at 38 mm to -1.2 at 58 mm height within the foamer (data not shown). This latter result is in excellent agreement with earlier findings in free drainage experiments (Koehler et al., 2000) also reporting an exponent n=- 1.2 at the foam top.

At any time, the gas volume fraction φ increases linearly with the height within the foamer H (Fig.3.8B) and the gradient tends to increase with increasing foam age, i.e. the relative, drainage-induced change of gas volume fraction is more pronounced in the upper regions of the foam. Qualitatively, these results can be attributed to foam drainage. The quantitative changes of φ with time and/or height within the foam column characterize the drainage process in a foam created from this type of milk using this particular whipping device. Regimes of linear dependency of liquid fraction $(1\text{-}\varphi)$ on height within foams had been found previously in free drainage experiments (Saint-Jalmes and Langevin, 2002) in accordance with the solution of a simplified version of the free drainage differential equation (Verbist et al., 1996).

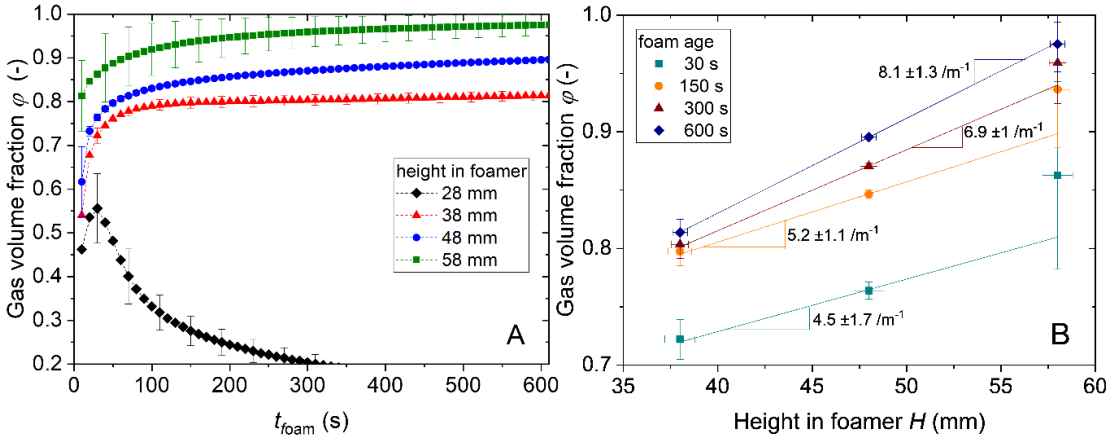

Figure 3.8: Gas volume fraction φ of reconstituted milk foams versus foam age t_{foam} measured at different heights inside the foamer as well as determined volumetrically (A) and versus height inside the foamer H at different foam ages (B). Lines in B are linear fits to the data.

The yield stress of foams τ_y in general scales linearly within the Laplace pressure inside the bubbles σ/R_{32} (Princen and Kiss, 1989) and quadratically with φ (Mason et al., 1996). yielding the following empirical model:

$$\tau_y = k\,\sigma/R_{32}\,(\varphi-\varphi_c)^2 \qquad (3.6)$$

When φ_c is exceeded, gas bubbles start to deform and a yield stress emerges. Mason et al. (Mason et al., 1996) found a numerical pre-factor $k = 0.51$. The temporal and spatial changes in τ_y for the investigated foam from reconstituted milk are shown in Fig.3.9A and B. The yield stress monotonically increases over time and absolute values between 1 and 15 Pa were obtained. Similar yield stress increase between 5 to 10 Pa had been reported for milk foam produced with steam injection (Jimenez-Junca et al., 2015). The initial increase in τ_y is less pronounced than expected from the increase in φ since the increase of τ_y with φ is partly compensated by the increasing R_{32}. At least qualitatively, the observed changes in τ_y correspond to the changes in φ and R_{32} discussed above. The increase of yield stress τ_y with the height in the foamer H is linear within the range of vertical distance investigated here. The increase of yield stress gradient with foam age is a consequence of the increasing gradient in φ.

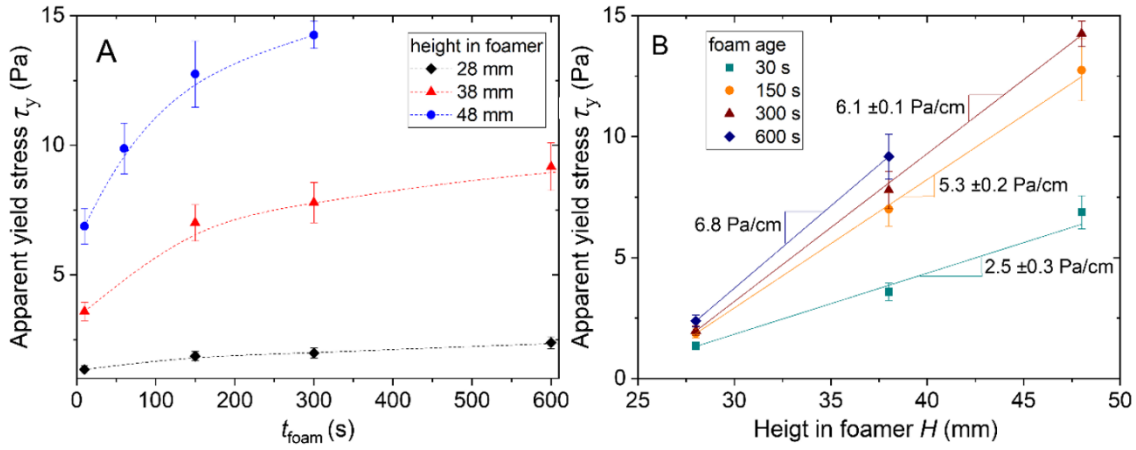

Figure 3.9: Apparent yield stress τ_y of reconstituted milk foams versus foam age t_{foam} measured at different heights inside the foamer (A) and versus height inside the foam at different foam ages (B). Lines in A guide the eye. Lines in B are linear fits to the data.

Rheological and microstructural results obtained in situ for different types of milk are compared in terms of the time dependence of the R_{32}, φ and τ_y gradients along the vertical axis as shown in Figs.3.10A-C. The change in R_{32} along the foam column axis (Fig.3.10A) exhibits a similar linear increase with aging time t_{foam} for all three milk types. The absolute value of the gradient for the foam made from reconstituted milk seems to be systematically higher than for the other foams. The differences among the different milk types, however, are less pronounced than the changes over time. The gradient in gas volume fraction φ is significantly higher for the reconstituted milk than for the UHT milk types (Fig.3.10B), which both exhibit similar gradients irrespective of foam age. It should be noted that this gradient refers to the upper part of the foam, the gas volume fraction at the lowest measuring position were mostly below φ_c, and thus not included in the gradient calculations.

This gradient increases approximately linearly with foam age t_{foam} and the slopes are similar for all investigated foams. Such an increase of the gas volume fraction gradient with time at the lower end of a foam column is also predicted from free drainage theory (Verbist et al., 1996). The larger heterogeneity of bubble size and gas volume fraction in the foam from the reconstituted milk might be due to incomplete protein solubilization and thus lower availability for stabilization of foam lamellae during air entrainment. Foams consisting of larger bubbles possess lower interfacial area to be stabilized. If the protein concentration does not provide saturation of the interfacial area in a foam consisting of small bubbles, bubbles quickly coalesce and the average size increases (Lech et al., 2016). Subsequently, the coupling of bubble size and drainage velocity leads to the stronger gradients in the direction of gravity. Enhancing the protein solubilization by adding a second heating and mixing cycle during preparation of the reconstituted milk consequently led to 20% smaller initial mean bubble radius in the foams (data not shown).

The time evolution of the yield stress gradient along the vertical axis of the foam columns of different milk types is shown in Fig.3.10C. This gradient increases monotonically over time and the increase is most pronounced within the first three minutes of foam age similar for all milk types.
Consistent with the finding that the gradients in φ and R_{32} are similar for the foams made from 1.6% and 3.6% fat milk we find similar absolute values for the yield stress gradient in these foams. For the reconstituted milk the different gradients in φ and R_{32} compensate and consistently the yield stress gradient is similar to that of the other two types of milk foam.

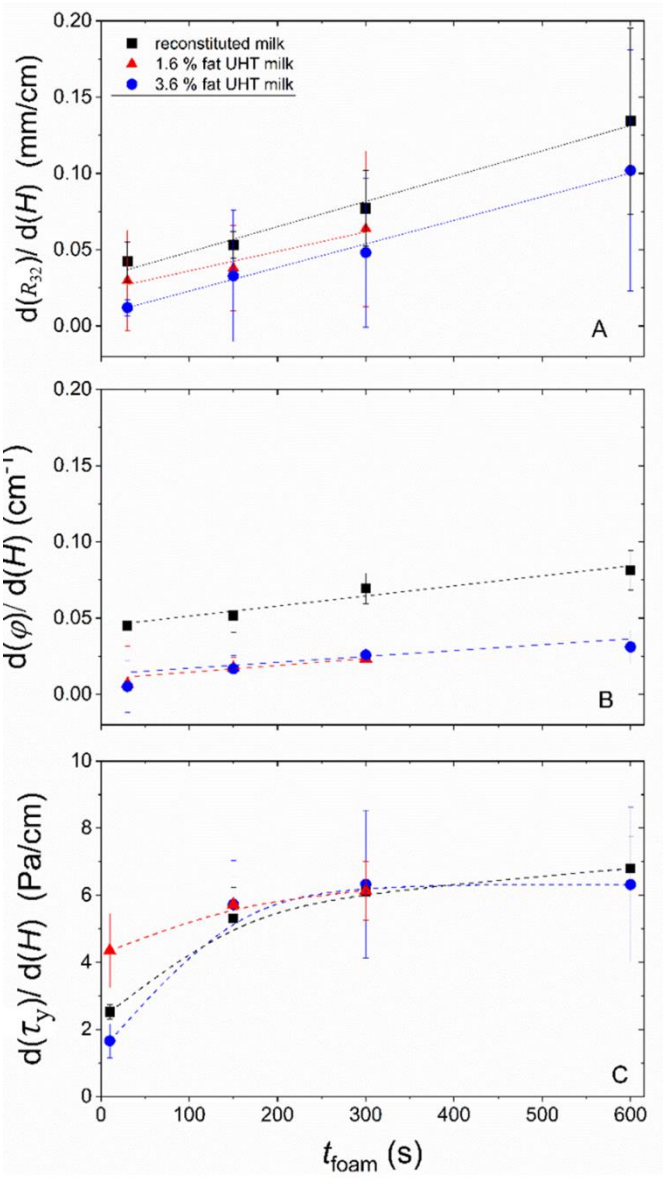

Figure 3.10: Vertical gradient of Sauter radius $d(R_{32})/d(H)$ (A), gas volume fraction $d(\varphi)/d(H)$ (B) and yield stress $d(\tau_y)/d(H)$ (C) of foams made from 1.6 % and 3.6 % fat UHT milk, and reconstituted milk versus foam age t_{foam}. Lines in A and B are linear fits to the data. Lines in C guide the eye.

We have analyzed all τ_y data obtained at different times, positions within the foams, and milk types in terms of the scaling suggested in Eq.3.6. The σ, R_{32} and φ data were directly taken from the corresponding measurements described above. The critical gas volume fraction φ_c was set to 0.635.

Fig.3.11 shows the scaling of $\tau_y/\sigma/R_{32}$ with $(\varphi-\varphi_c)^2$ for all collected data. Despite some scatter in the experimental data, Eq.6 describes the yielding of the foam types investigated here very well.

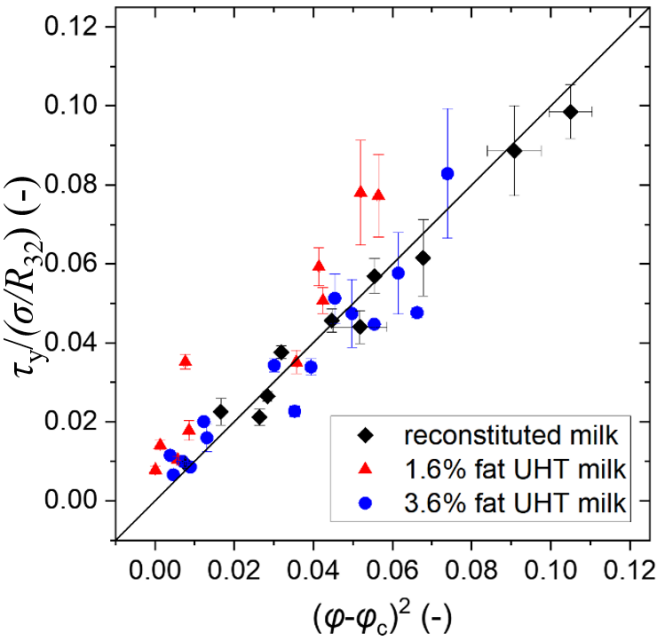

Figure 3.11: Yield stress τ_y normalized by Laplace pressure σ/R_{32} versus $(\varphi-\varphi_c)^2$ where φ_c is the critical packing fraction at which gas bubbles start to deform, here set to 0.635 corresponding to the random close packing of monodisperse spheres. Data are shown for foams of UHT milk with 3.6 % and 1.6 % fat, respectively, and reconstituted milk. Line shows the identity function.

3.4 Conclusion

Here we presented the first apparatus combining foam generation and in-situ characterization of bubble size distribution and yield stress with simultaneous gas volume fraction measurement. The endoscopic setup and the fast, automated bubble size distribution analysis enable data collection with a spatial resolution on the order of millimeters and temporal resolution on the order of seconds. The temporal and spatial resolution of the yield stress measurement is restricted by a measuring time of 60 seconds and the vane rotor height of 9 mm. The gas volume fraction measurement follows the spatial resolution of the vane rotor. The apparatus was proven to resolve significant differences between foams from milk types that underwent different processing.

For the first time, yield stress profiles along the direction of drainage in foams were resolved. The yield stress increased with the height in the foam column as well as with ongoing foam drainage due to the increase in gas volume fraction, which was partially compensated by the bubble growth. The obtained milk foam yield stress values τ_y were found to scale with the product $\sigma/R_{32}\,(\varphi-\varphi_c)^2$ as suggested by the phenomenological model of Mason et al. (Mason et al., 1996), emphasizing the reliability of the measurement setup.

The new device allows for systematic studies regarding the effect of foaming parameters such as heating rate, temperature distribution within the cell or coil dimensions and speed on rheology and microstructure of created foams. Moreover, it offers new opportunities for fast characterization of new foam formulations, e.g. based on dairy products or milk substitutes, and their evaluation in comparison to regular milk foam.

3.5 Appendix

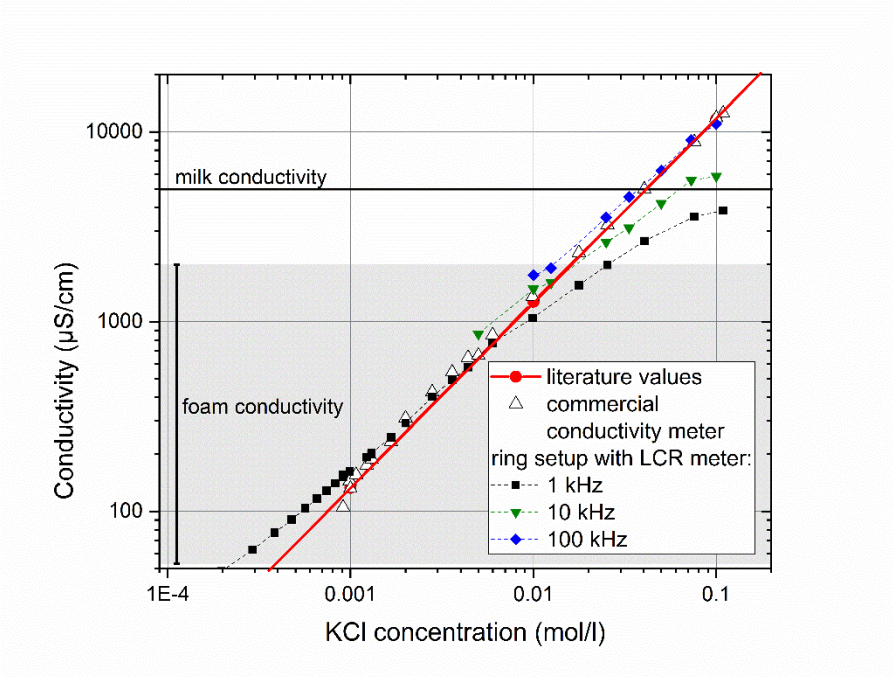

Fig.3.A1: Conductivity of potassium chloride solutions versus salt concentration measured with a commercial rod electrode connected to a conductivity meter (Inlab® 738 ISM and S230 seven compact, Mettler Toledo, Schwerzenbach, Schweiz) (hollow triangles) and brass ring electrodes inside the foamer connected to an LCR meter (U1733C 20,000-Count-Display Handheld LCR Meter, Keysight Technologies, Santa Rosa, USA) at frequencies of 1 Hz (black squares), 10 kHz (green triangles) and 100 kHz (blue diamonds). Solid red line shows the linear fit to the literature values (Pratt et al., 2001)

4 Foams stabilized by lupin protein isolate of *Lupinus.angustifolius*

Full title: Structure and rheology of foams stabilized by lupin protein isolate of *Lupinus.angustifolius*

Authors: Annika Ricarda Völp, Jonas Seitz, Norbert Willenbacher

Status: published

Bibliografic data: Food Hydrocolloids, 2021, S. 106919.

DOI: 10.1016/j.foodhyd.2021.106919

Plant-based protein sources play an important role in sustainable human nutrition but often lack in attractivity compared to animal-derived food products. Aerating is commonly used to increase the appeal of foods and may also improve acceptance for plant-based proteins in consumers' diets. We investigated structure and rheology of foams made from lupin protein isolate. Foamability and foam stability were determined from manual shaking tests. Gas volume fraction, bubble size, yield stress and shear modulus of the foams were determined during aging of pneumatically created foams. The impact of temperature pretreatment, pH and ionic strength on protein size distribution and conformation as well as surface activity in the aqueous solutions was characterized, and its effect on foaming behavior and foam properties is discussed. All foams were stable for at least one hour. Heat induced denaturation of proteins did not alter foam characteristics much. Foaming capacity, however, strongly increased with increasing pH or ionic strength, but again gas volume fraction and bubble size were hardly affected. Foam rheology was shown to correlate not only to gas volume fraction, bubble size, and interfacial tension but also to the protein solutions' interfacial elasticity. Protein aggregation decreased foamability but reduced drainage and hence increased foam stability. Blocking of drainage pathways by precipitated aggregates trapped in Plateau channel nodes was evidenced in endoscopic video observations. A "plant milk" made from lupin protein isolate, carboxymethyl cellulose as thickener, and emulsified sunflower oil yielded similar foam volume and texture as cow milk when prepared in a commercial whipper.

4.1 Introduction

The challenge to feed the growing world population sets a need for sustainably produced, plant-based protein sources in food (Gorissen et al., 2018; Hartmann and Siegrist, 2017; Kinsella, 1981; Neacsu et al., 2017). Legumes are rich in protein and the world health organization predicts them to play a key role in future healthy and sustainable diets (World Health Organization, 2018). Soybeans followed by lupins obtain the highest protein contents among legumes, with up to 48% in soybeans (Friedman and Brandon, 2001) and 33 to 47% in lupin seeds (Sujak et al., 2006). Lupins are tolerant to abiotic stresses and capable of nitrogen fixation making them suitable for recovery of poor and contaminated soils (Böhme et al., 2016). But little effort has been made in breeding to enhance grain yield and giving economic incentives for cultivation of lupins in Europe. Hence, 70% of the European protein demand is covered by soybean imports while native lupins play only a minor role (Lucas et al., 2015). Soy production was increased tenfold during the last 50 years, demanding conversion of vast areas, among others rainforest and savanna in South America, into acreage and 75% of it flow into production of feed for livestock (Aiking, 2011; FAO, 2020; Stabile et al., 2020). To replace soy imports as well as proteins of animal origin in food by plant based, locally produced protein sources, progress in lupin cultivation as well as advances in production of attractive food based on lupin proteins is required.

Aerating may increase the appeal of food by bestowing pleasant textural sensation and visual appearance, and intensifying flavors transmitted via the enlarged interface. Marketing also exploits foamed foods' benefits of increased volume and reduced energy density for low calorie products. Bubbles in liquid food foams are commonly stabilized by egg-white or milk proteins.

These proteins adsorb to air/water interfaces where they partially unfold exposing hydrophobic molecule regions into the gaseous phase and reduce the interfacial tension that counteracts the surface increase involved in foam formation. Intermolecular hydrogen bonds, disulfide bridges and hydrophilic/hydrophobic interactions between the amino acids of unfold protein strands may develop, providing the interface with elasticity which equilibrates local protein concentration thinning that would promote bubble rupture (Gurkov et al., 2007; Petkov et al., 2000). The physico-chemical properties of proteins, set by their content and location of amino acids, size, shape conformation, charge and intermolecular interaction, define their capability to adsorb onto the interface fast enough to prevent coalescence of newly formed bubbles and subsequently stabilize the bubbles by formation of an elastic film that prevents thinning and rupture of the lamellae between neighboring bubbles (Cantat et al., 2013; Kinsella, 1981; Rouimi et al., 2005). The combination of both mechanisms is crucial for the ability of a protein solution to form considerable volumes of foam and to stabilize them against drainage, coalescence and disproportion of bubbles. The potential for replacement of egg-white or milk proteins as food foaming agents by lupin protein isolates has been proven in previous studies. Several studies present the foaming capacity and foam stability of solutions of protein isolated of *Lupinus.albus, Lupinus.campestris, Lupinus.angustifolius,* and *Lupinus.luteus* partially at different protein concentration, pH or ionic strength (Jayasena et al., 2010; Monteiro et al., 2020; Rodríguez-Ambriz et al., 2005; Sathe et al., 1982; Vogelsang-O'Dwyer et al., 2020; Wäsche et al., 2001; Wong et al., 2013).

In a more extensive study, the effect of thermal treatment, acylation, enzymatic hydrolysis and a series of thickener in solutions of protein isolate from *Lupinus.ablus* on the foaming capacity and foam stability, and the stiffness of cooked foams were evaluated (Raymundo et al., 1998). However, these studies are limited to findings on foaming capacity and stability regardless of the foam structure and rheological behaviour, although these characteristics are decesive for consumers perception as well as processability of foams.

We investigated foaming capacity and foam stability for aqueous solutions of protein isolates of *Lupinus.angustifolius* based on manual shaking tests. Pneumatically created foams made from solutions of various composition differing in heat pretreatment of protein, pH, ionic strength, added sodium carboxymethyl cellulose (CMC) and oil were investigated with respect to bubble size, gas volume fraction and rheology and the change of these properties during aging. We determined the interfacial tension and elasticity of those protein solutions and correlate the results to foam structure, and foam rheology, in terms of yield stress τ_y and elastic modulus G_0. These rheological parameters scale with the bubbles Laplace pressure (Princen and Kiss, 1986), given by the ratio between the interfacial tension σ and the Sauter bubble radius R_{32}, the foam's gas volume fraction φ, the critical packing fraction φ_c of the particular bubble size distribution, the solutions viscosity η_l normalized to the solvent viscosity, here the viscosity of water η_w, and empirical, foaming system specific constants, k and a, according to following phenomenological models (Lexis and Willenbacher, 2014a; Marze et al., 2009; Mason et al., 1996):

$$\tau_y = k\,\sigma/R_{32}\,(\varphi-\varphi_c)^2(\eta_l/\,\eta_w)^{0.3} \qquad (4.1)$$

$$G_0 = a\,\sigma/R_{32}\,\varphi(\varphi-\varphi_c) \qquad (4.2)$$

The commercial protein isolate of *Lupinus.angustifolius* used in this study was of German origin. According to the manufacturer the isolate was produced by protein extraction from the seeds in aqueous phase at neutral pH and subsequent spray drying. After that processing, approximately a third of the isolated protein mass consists of albumins, i.e. water-soluble proteins at ambient temperature and neutral pH. The native proteins' structure is unknown and might have been changed during spray drying. However, heat treatment of the protein, changes in pH and ionic strength of the protein solution changes the proteins' conformation and solubility (Kinsella, 1981). This is also evidenced for the proteins used in this study based on the changes of the proteins' Fourier-transform infrared spectra and protein size distribution. We investigated the impact of the changes in protein structure and solubility on the interfacial and foaming properties of the solutions. In food foams, the interactions among proteins, water, lipids and other components determine the foams' overall behavior (Kinsella, 1981).

In view of an application of the protein isolates in foods, addition of sodium carboxymethyl cellulose (CMC), a food grade thickener consisting of simple linear polymers, and emulsification of sunflower seed oil on the above-mentioned foam characteristics was tested. A lupin protein "plant milk" was formulated and the foaming capacity obtained whipping it in a commercial milk whipper was compared to that of bovine whole milk.

Protein aggregates form due to temperature denaturation or at the isoelectric point of the proteins and act like particles that enhance foam stability when they adsorb onto the interfaces. Rigid films along the bubbles' interfaces form, as evidenced by an increased interfacial elasticity, making the bubbles stable against coalescence and disproportionation (Binks and Murakami, 2006; Lazidis et al., 2017). When the aggregates surface activity is too weak, due to slowed down diffusion at increased aggregate size or low hydrophobicity, they remain in the continuous phase where they may create a percolating network or may block the foams' Plateau channels hereby reducing the gravity driven liquid drainage (Binks and Murakami, 2006; Lazidis et al., 2017). Generally, we separated the insoluble fraction of protein isolate before foaming. In order to examine the role of protein aggregates > 1 µm in the foam, foams made from protein isolate solutions before separation of those protein precipitates, as well as solutions with protein aggregates produced by isoelectric precipitation were additionally characterized. We evidenced the blocking of plateau channels in endoscopic video observation for the first time using a stained drainage liquid. Also, the aggregates' impact on foam yield stress and elasticity with increasing gas volume fraction was elucidated, supporting the hypothesis of aggregate network formation.

4.2 Materials and Methods

4.2.1 Sample preparation

Lupin protein isolate from Lupinus.angustifolius, aqueously extracted and spray dried, was purchased from Prolupin GmbH (Grimmen, Germany). This product consists of 87 to 95% proteins, 7% ash, 3% fat, and 1.5% fibers, according to the product data sheet. Solutions, were prepared stirring 5% protein isolate into ultrapure water for 30 min at room temperature using a magnetic stirrer. The sample preparation process is illustrated in Fig.4.1. The solution was either stirred at ambient temperature or simultaneously heated up to 50°C, 70°C and 90°C on a heating plate or to 100°C in a thermostat (LAUDA Dr. R. Wobser, Lauda-Königshofen, Germany), respectively. The respective temperature was kept constant for at least 30 min. The solutions were then cooled down to room temperature in a water bath. The temperature profiles to which the solutions were exposed are shown in Fig.4.A1A. Evaporated liquid was replaced by ultrapure water after cooling down. Subsequently, 40 ml aliquots of the solutions were filled into centrifuge tubes (Zellstar Test Tubes, Greiner Bio-One, Kremsmünster, Austria) and centrifuged for 20 minutes at approx. 9000 relative centrifugal force in a tabletop centrifuge (Hettich Universal 320, Tuttlingen, Germany;) in order to separate the protein precipitates. The supernatants were collected and the respective protein concertation, shown in Fig.4.A1B, determined as described in 2.2. An aliquot of 5% protein isolate solution heat treated at 50°C was kept with precipitates (see Fig.4.1: 50°C + precipit.). Subsequently, the supernatants were diluted to a protein concentration of 10 g/l (see Fig.1: 20°C pH 6.8, 50°C, 70°C, 90°C, 100°C).

An aliquot of the supernatant of the solution heat treated at 50°C was used undiluted (see Fig.4.1: 50°C 20g/l). Additionally, an aliquot of the undiluted supernatant prepared at 20°C was set to the isoelectric point (pH 4) using hydrochloric acid (Carl Roth GmbH, Karlsruhe Germany) (see Fig.4.1. pH 4 + precipit.), which led to aggregation of proteins. The isoelectric point was determined beforehand, by stepwise acidifying the supernatant of the protein solution prepared at room temperature and measuring the respective zeta potential (Zetasizer Nano, Malvern Panalytical, Kassel, Germany). An aliquot of the sample with pH 4 was separated from precipitated proteins by an additional centrifugation step as described above (see Fig.4.1: pH 4).

A protein concentration of 20 g/l in this sample was determined as described in 2.2. Aliquots of the sample dissolved at 20°C and diluted to 10 g/l (see Fig.4.1: 20°C pH 6.8) were further modified by adjusting to pH 10 using sodium hydroxide (see Fig.4.1: pH 10), dissolving 10 and 50 mmol/l sodium chloride (see Fig.4.1: 10 mM NaCl, 50 mM NaCl), dispersing respectively 0.01, 0.075, and 0.1 vol% of sodium carboxymethyl cellulose (weight average molecular weight Mw =700 kg/mol, Merck, Darmstadt, Germany) (see Fig.4.1: CMC), or emulsifying 3% sunflower seed oil into it (see Fig.4.1: 3% oil), respectively. The CMC dispersion was prepared mixing the CMC powder with stepwise addition of the protein solution in a beaker on a magnetic stirrer. The emulsion was prepared adding 55 g of oil and protein solution into a 100 ml glass beaker and pulsing the mixture at 50% amplitude with cycles of 3 s pulse followed by 1 s pause for 5 min with a 1.27 cm diameter disruptor horn connected to a Sonifier Model 250 (both, Branson Ultrasonics Corportaion, Danbury, USA). The emulsion was stirred during the process with a magnetic stirrer and the temperature was kept constant at 20°C ±0.5°C by cooling the beaker in a water bath connected to a thermostat.

A “plant milk” was produced from the undiluted supernatant of the solution heat treated at 50°C (see Fig.4.1: 50°C 20 g/l) by dispersing 0.01 vol% sodium carboxymethyl cellulose and emulsifying 3% sunflower oil into it, as described above (see Fig.4.1: 0.01 vol% CMC + 3% oil). All characterizations had been done within 24 hours after sample preparation.

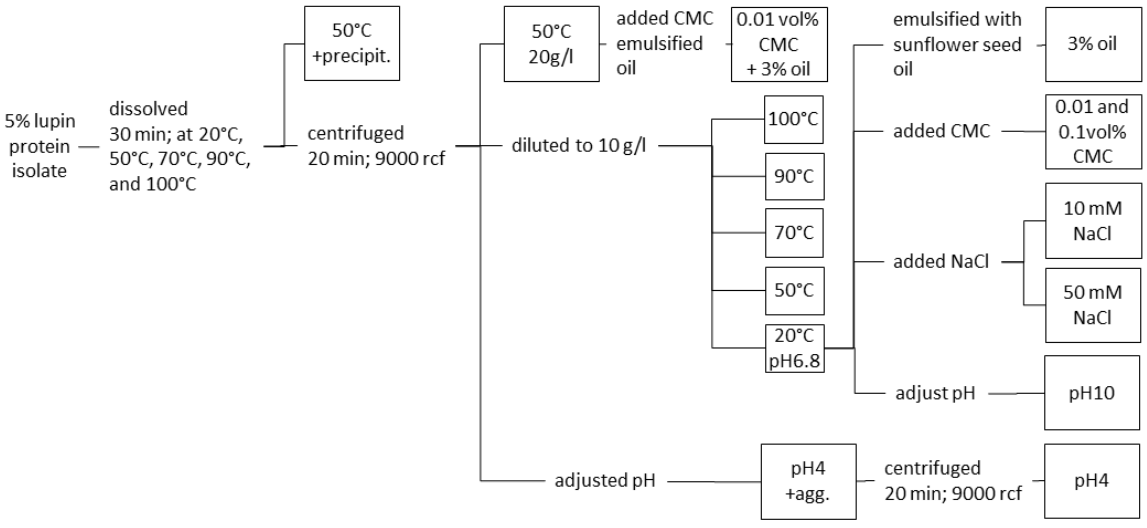

Figure 4.1 Sample preparation process

4.2.2 Protein concentration determination

The protein concentration in dilutions of the supernatants with ultrapure water (1:10, 1:30, 1:150) was determined from their optical densities, measured in a 96 well plate with 10 mm path length using a photometer (Infinite M200, Männedorf, Switzerland) at 280 nm wavelength. The optical densities were multiplied with the extinction coefficient of the protein solution to obtain the protein concentrations in the diluted supernatants. The extinction coefficient of 0.73 ± 0.01 $(mg/ml)^{-1}cm^{-1}$ was determined by correlating optical densities of protein solutions with their respective protein concentration determined in a BCA Protein Assay (Thermo Fisher Scientific, Massachusetts, United States).

4.2.3 Protein aggregate size determined using dynamic light scattering

The aggregate size distribution in the protein solutions was determined using dynamic light scattering (Zetasizer Nano, Malvern Panalytical, Kassel, Germany) in 173° angle backscattering. The measurement was conducted in disposable micro UV cuvettes with 10 mm path length and filled with 100 µl protein solution. The measurement was performed three times for each solution.

4.2.4 Protein conformational changes determined using Fourier-transform infrared spectroscopy

The FTIR spectra of the protein solutions was recorded using a spectrometer with BioATRII measurement accessory (Tensor27 Bruker Optics, Ettlingen, Germany) at 20°C. Spectra were recorded at wavelengths from 3500 cm^{-1} to 900 cm^{-1} with a resolution of 4 cm^{-1} and a scanner velocity of 160 kHz. Spectra of 64 scans were averaged. The background, measured in distilled water, was subtracted from the signals.

4.2.5 Solution viscosity determined using rotational rheometry

The viscosity of the protein solutions was measured using a rotational rheometer equipped with a concentric cylinder measuring system (Physica MCR 501 and CC27, Anton Paar, Graz, Austria) at shear rates increasing in 10 steps per decade from 1 s^{-1} to 200 s^{-1}. The solutions exhibited Newtonian behavior within the tested shear rate range and the average viscosity was calculated from the values obtained between 5 s^{-1} and 50 s^{-1}. The measurement was repeated three times and the protein solution in the measuring cup was replaced after each measurement.

4.2.6 Interfacial tension and elasticity determined using pendant drop method

The interfacial tension of all solutions was determined using a pendant drop tensiometer (PAT1, Sinterface, Berlin, Germany). A drop of the respective protein solution with a surface area of 30 mm^2 was produced from a cannula with 1 mm inner diameter. The interfacial tension was calculated from the drop shape over a period of 3 h maintaining a constant surface area. The surface area was then dilated in oscillation for at least 10 cycles with an amplitude of 3 mm^2, followed by 15 minutes maintaining constant surface area. The oscillation frequencies were 0.05, 0.1, 0.33, 0.5 and 0.67 Hz, three oscillations were performed at each frequency. The interfacial tension and elasticity were determined as described elsewhere (Pandolfini et al., 2011). The respective mean values and deviations were calculated from two measurements with independently prepared solutions. The interfacial elasticity E' at the maximum frequency and the equilibrium interfacial tension σ after 1 h drop age were extracted, respectively.

4.2.7 Foamability and foaming capacity determined by shaking

The development of the foaming capacities over time was determined in a manual shaking test. Five cylindrical 40 ml screw cap glasses were filled with 10 to 12 ml of protein solution and set side by side into an acrylic glass box with scaling paper on the back. The solutions in the box were shaken by hand for 30 seconds. The box was turned horizontally by 180° and immediately shaken again for 30 seconds. The volumes of foam V_{foam} and liquid V_{liquid} were obtained from the liquid and foam heights in the glasses. The foaming capacity was calculated as follows:

$$FC\ (\%) = 100(V_{liquid} + V_{foam} - V_{liquid\ before\ foaming}) / V_{liquid\ before\ foaming} \quad (4.3)$$

The average and standard deviation of the foaming capacities was calculated for the five foam columns in the box.

4.2.8 Pneumatic foam preparation

A filter funnel (ROBU VitraPoR, Hattert, Germany; 125 ml, pore size 4) containing a glass membrane with pore size 9-16 µm was filled with 50 ml foaming solution. The solution was foamed purging the glass membrane with nitrogen at a volumetric flow rate of 60 ml/min through the funnel outlet. Once the filter cup was completely filled with foam, the nitrogen supply was stopped and recording of the foam aging started. (Lexis and Willenbacher, 2014a)

4.2.9 Bubble size distribution determined using endoscopy

A straight, rigid 285 mm long endoscope (VH-B55, Keyence Osaka, Japan) with a diameter of 5.5 mm was covered by an outer metal tube, 295 mm in length and 6 mm in diameter, and equipped with a 90° angle mirror was connected to a CMOS camera (VHX-950F, Keyence Osaka, Japan). The endoscope was inserted into a customized optical glass cuvette. The size to pixel ratio was determined using millimeter scaling paper. Subsequently, the endoscope was placed into the filter funnel with a distance to the bottom glass membrane of 30 mm. An LED spotlight with 2500 lm luminous power was placed at the outside of the filter funnel wall. The filter funnel was filled with 50 ml of sample and the foaming process was started. Images were recorded every 15 seconds starting immediately after the foaming process stopped. The images were analyzed using a template matching tool written in MATLAB® (Mathworks, Natick, USA) with 25 circular templates differing in diameter from10 to 200 pixels, as described elsewhere (Völp et al., 2020a). The frequency density distribution histogram and the cumulative distribution of the bubble diameter counts and volumes were calculated from the obtained bubble size lists based on the 25 size classes. The span of the count distribution $(r_{90}-r_{10})/r_{50}$ and the Sauter radius R_{32} were calculated from these data. All measurements were repeated at least three times with freshly prepared foams.

4.2.10 Drainage pathway visualization using Aggregate staining

A 50 ml aliquot of the supernatant of protein isolate solution with a protein concentration of 17.6 g/l was mixed with 1 mL of red dye (Diffusions-Rot USR, Helmut Klumpf Techn. Chemie KG, Herten, Germany). Subsequently, pH4 was adjusted in the stained protein solution adding hydrochloric acid to obtain red protein precipitates. Foam was prepared from the solution containing stained precipitated aggregates, as described in 2.8. Endoscopic images of the bubbles inside the foam were recorded with a framerate of 15 s^{-1} using the endoscopic setup described in 2.9, while approx. 1 ml of blue dye (Coomassie brilliant blue R-250, Bio Rad, Hercules, USA) was pipetted onto the foam. The image recording was stopped once the blue dye had permeated the foam.

4.2.11 Gas volume fraction determined using electrical conductivity measurements

The conductivities of the foams κ_{foam} and the protein solutions $\kappa_{solution}$ were measured and recorded using a commercial conductivity meter equipped with a four-electrode conductivity sensor (Inlab® 738 ISM, Mettler Toledo, Schwerzenbach, Schweiz). The electrode was mounted into the filter funnel with a distance to the bottom glass membrane of 30 mm.

The conductivity measurement was started immediately after the foaming process stopped and data was recorded every 15 seconds for 20 min. The foam gas volume fraction φ was calculated using the following empirical correlation (Feitosa et al., 2005):

$$\varphi = 1 - (3\,\kappa_{rel.} + 33\,\kappa_{rel}) / (1 + 25\,\kappa_{rel} + 10\,\kappa_{rel}^{2}) \quad (4.4)$$

where κ_{rel} is the foam conductivity divided by the solution conductivity. The measurement was repeated at least three times with independently produced foam samples.

4.2.12 Foams' yield stress and shear modulus determined using rotational rheometry

For yield stress measurements, a rotational rheometer (Mars II, Haake Thermo Fisher Scientific, Karlsruhe, Germany) with an in-house manufactured, four bladed vane rotor (36 mm diameter, 9 mm height) and the filter funnel described in 2.8 built into the rheometer as measuring cup was used. The vane geometry was lowered to the measuring position in the foam 30 mm above the bottom glass membrane within 20 s and the measurement was started when the foam reached the desired foam age. The shear stress σ was increased from 0.5 to 20 Pa in 12 steps equally distributed on a logarithmic scale during a total measuring time of 60 s. The measurement was repeated at least three times with freshly prepared foam samples. The recorded deformation was plotted versus shear stress and the yield stress τ_y was determined using the tangent intersection point method as described elsewhere (Willenbacher and Lexis, 2018).

For shear modulus measurements, a rotational rheometer (Rheoscope1, Haake Thermo Fisher Scientific, Karlsruhe, Germany) and a plate-plate geometry 60 mm in diameter was used. Bottom plate and rotor plate were covered with sandpaper (grit 40, average particle diameter 269 µm) to reduce wall slip. Approx. 20 ml of foam was withdrawn from the filter funnel using a spoon and was put onto the bottom plate 20 seconds before it reached the desired foam age, the gap height was set to 6 mm within 20 seconds and the measurement was immediately started. The foams were sheared in oscillation with a fixed frequency of 1 Hz while the stress amplitude increased stepwise from 0.1 to 400 Pa in 12 steps equally distributed on a logarithmic scale. The real part G' and the imaginary part G'' of the complex shear modulus was calculated as described elsewhere (Khan et al., 1988). The constant value of G' in the linear viscoelastic regime was termed shear modulus G_0 since the measuring frequency was between 0.01 and 10 Hz, which is typically the frequency independent regime of the shear moduli in foams (Marze et al., 2009). Measurements were repeated at least three times with freshly produced foam.

4.2.13 Foam preparation in commercial milk whipper and foaming capacity determination

A commercial milk whipper (Nespresso Aeroccino 4, Nespresso S.A., Lausanne, Switzerland) was filled with 120 ml ultra-high temperature (UHT) whole milk (Alpenmich, haltbar, 3.5% Fett, Alnatura, Bickenbach, Germany) or lupin protein "plant milk", prepared as described in 2.1, at room temperature, respectively. The whipper whipped the milk with a stirring coil at the bottom of its container and simultaneously heated it for approximately 70 s until the milk at the bottom had reached 60°C. Foam and remaining milk was poured from the whipper into a measuring cylinder directly after the foaming process stopped and volumes of foam V_{foam} and drained milk V_{milk} were recorded for 15 minutes. The foam's gas volume fraction was calculated as follows:

$$\varphi = 1 - (120\ ml - V_{milk})/V_{foam} \quad (4.5)$$

The Sauter bubble radius was determined in the foam which was poured into a glass beaker with similar diameter as the whipper directly after foaming at 35 mm height as described above (Chapter 4.2.9). The foam yield stress was measured in-situ at 35 mm height inside the whipper 300 s after the foaming process had stopped as described above (Chapter 4.2.12). All measurement was repeated three times with fresh milk.

4.3 Results and discussion

The interfacial activity of the lupin protein is evaluated in Chapter 4.3.1, the foam capacity and stability are presented in the context of protein structure in Chapter 4.3.2. The foam structure in terms of bubble sizes and gas volume fraction are targeted in Chapter 4.3.3 and used to normalize the foam rheological data in Chapter 4.3.4. In Chapter 4.3.5, the foam rheology is correlated with the interfacial elasticity of the foamed solution and the effect of protein aggregation is addressed. In Chapter 4.3.6, the foam properties of a lupin milk formulation are demonstrated to evaluate the protein's potential for application in foaming plant-milks. The results shown in the subsequent sections were determined from at least three measurements with fresh samples if not stated otherwise, the displayed data are average values and the standard deviations are shown as error bars, error propagation was considered where applicable.

4.3.1 Interfacial tension of protein solution

Heat pretreatment of the protein solution, changes in ionic strength, increasing the pH of the protein solution or addition of CMC had minor effects on the surface activity of the proteins, as shown by the dynamic interfacial tension in Fig.4.A2. The equilibrium interfacial tension was reached within about 3000 s and its absolute value varied in a small range between 42 and 44 mN/m (Fig.4.A2). The equilibrium interfacial tension was scarcely reduced to 41 mN/m in a solution with doubled protein concentration, i.e. 20 g/l protein, indicating that the interface is almost saturated at 10 g/l protein. Drastic changes in dynamic interfacial tension were observed only upon acidification of the solution to pH 4 (see Fig.4.A2B) and addition of sunflower seed oil (Fig.4.A2D). In both cases, the interfacial tension rapidly decreased within the first minute after formation of the interface. However, the equilibrium interfacial tension remained relatively high, i.e. at 47±1 mN/m, for both samples. When sunflower seed oil was added, this is presumably due to a partial adsorption of proteins at the surface of the oil droplets thus no longer available for the stabilization of the air/liquid interface. At pH4, the equilibrium interfacial tension remained high, because a large fraction of aggregates > 0.1 µm was formed (see Fig.4.A3B), too big to display surface activity. For samples containing protein precipitates, interfacial tension measurements were inhibited by the presence of protein aggregates > 1 µm. But as they are not surface-active, the interfacial tension of protein solution was expected to be the same as for the centrifuged protein solutions.

4.3.2 Foaming capacity and foam stability

In Fig.4.2A, the foaming capacity of manually shaken protein solutions is depicted as a function of pretreatment temperature. Obviously, heat treatment of lupin protein did not affect its foaming capacity significantly, despite its distinct effect on protein denaturation confirmed by the vanishing minima in the second derivate FTIR spectra at resonance frequencies of ß-sheets and α-helixes with increasing pretreatment temperature (Fig.4.A4). The denaturation temperature of protein isolate of *lupinus.angustifolius* is approx. 70°C, as determined from differential scanning calorimetry (Bader et al., 2011; Sirtori et al., 2010). However, changes in the FTIR spectra and protein agglomeration were observed also for the protein solution heat-treated at 50°C. The proteins in the native protein solutions prepared at 20°C exhibited a median hydrodynamic diameter around 8 nm, similar as previously reported for *Lupinus.angustifolius* proteins ((Vogelsang-O'Dwyer et al., 2020). The heat induced protein unfolding, however, resulted in aggregation and broadening of the protein size distribution. The volume fraction of proteins bigger than 100 nm increased with increasing temperature (Fig.4.A3A). While these aggregates apparently have little effect on foam formation, the foaming solution pretreated at 50°C containing 20 g/l dissolved proteins and 30 g/l precipitated protein aggregates > 1 µm exhibited 30% lower foaming capacity (Fig.4.2A grey circle).

As shown in Fig.4.2B, the foaming capacity increased linearly with increasing pH of the corresponding protein solution and almost doubled when pH was increased from 4 to 10. An increasing foaming capacity and foam stability of lupin protein solutions with increasing pH were reported earlier and attributed to the improved solubility of the proteins with increasing pH (Jayasena et al., 2010; Piornos et al., 2015; Rodríguez-Ambriz et al., 2005). However, protein size distribution is essentially the same at pH10 as well as pH 6.8 (Fig.4.A3B) and the secondary structures remained intact confirmed by the unchanged FTIR spectrograms (Fig.4.A4), i.e. the reason for the huge difference in foaming capacity observed at pH 6.8 and pH 10 remains elusive. Only at pH 4, the isoelectric point of the lupin proteins, unfolding of secondary structures was found as indicated by the shifted or weakened minima in the second derivative of the FTIR spectrogram at resonance frequencies corresponding to the ß-sheet and α-helical structures (Fig.4.A4) and this resulted in large protein aggregates bigger than 200 µm (Fig.4.A3B). The large protein aggregates diffuse slowly and exhibit poor surface activity. Consequently, less bubbles can be stabilized when shaking the solution and foaming capacity is lower. The presence of additional 8 g/l protein aggregates > 1 µm in the solution with pH 4 further reduced the foaming capacity to half the volume of the foam made at native pH (Fig.4.2B grey circle).

As shown in Fig.4.2C, foaming capacity significantly increased with increasing ionic strength of the foaming solution, similar as previously reported (Piornos et al., 2015; Sathe et al., 1982). The increase of ionic strength caused a shift in the protein size distribution peak from 8 nm to 10 nm and 12 nm, respectively, when adding 10 and 50 mmol/l sodium chloride to the protein solution, respectively (Fig.4.A3C). In the latter case, additionally a small fraction of aggregates between 40 nm and 200 nm in diameter was found. The viscosity of the solutions dropped by 10% to 20% after addition of sodium chloride (TableA1), also indicating a reduced protein solubility. The FTIR spectra of the proteins dissolved in 50 mmol/l NaCl solution (Fig.4.A4) exhibited a reduced minimum of the second derivative of the infrared absorption at a resonance frequency typical for α-helical structures, suggesting that secondary structures of the proteins are partially unwound. This promotes intermolecular binding but also increases proteins' surface activity because hydrophobic regions originally tucked in the native protein conformation become accessible. Apparently, the higher surface activity of partially unfolded proteins prevailed the foamability reducing effect of protein aggregation which was still moderate at ionic strengths applied here.

Fig.4.2D shows that the foaming capacity decreased linearly with CMC concentration and dropped to half the value obtained with the native solution when 0.1 vol% CMC was added. This loss in foaming capacity is attributed to the reduced mobility of the proteins because of increased viscosity of the continuous phase (TableA1).

Fig.4.2E displays the foaming capacity of emulsions of lupin protein solution and various amounts of sunflower seed oil. The emulsions of 3% sunflower seed oil in 10 g/l lupin protein solution were produced using ultrasonic dispersing and resulted in a median droplet size of 1.5 µm and a droplet size distribution stable for three weeks. The foaming capacity was drastically reduced from 120% to 25% when adding 1% oil. This is attributed to a partial adsorption of proteins at the surface of the oil droplets thus no longer available for the stabilization of the air/liquid interface in the foam as also indicated by the higher interfacial tension of the emulsion compared to the pure protein solution (see Fig.4.A2D).

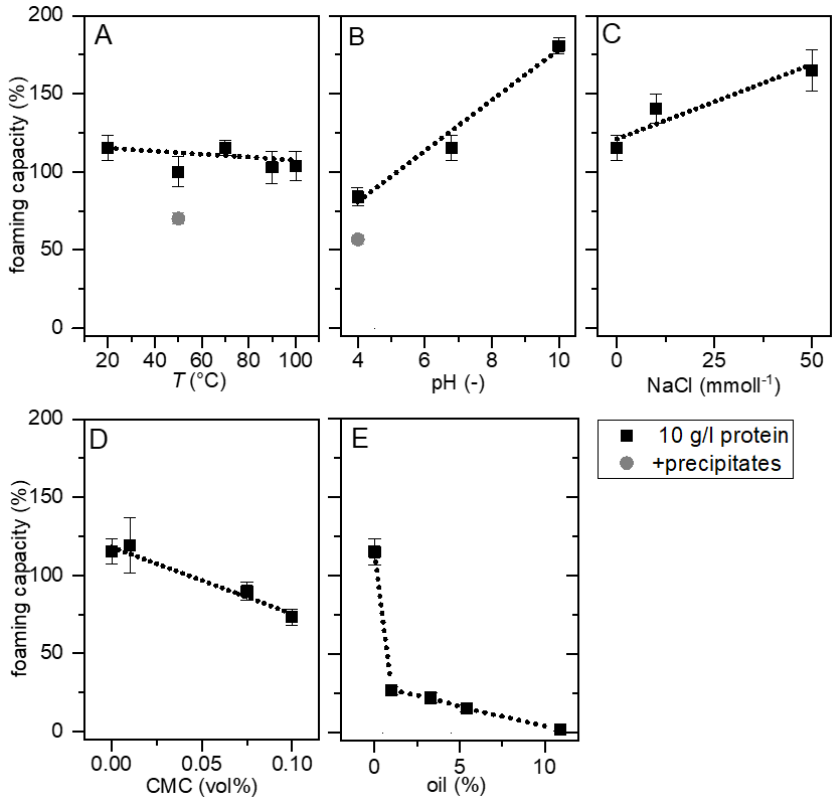

Figure 4.2: Initial foaming capacity of lupin protein solution foamed by manual shaking versus (A) pretreatment temperature, (B) solution pH, (C) sodium chloride concentration, (D) sodium carboxymethyl cellulose (CMC) concentration, and (E) sunflower seed oil concentration. The solutions' protein concentration is 10 g/l, except for samples containing additional protein precipitates (grey circles). Lines are to guide the eye.

The evolution of the foam volume, normalized by the volume of foaming solution, over time during free drainage of the lupin protein foams is displayed in Fig.4.3. With increasing foam age, the foam volume decays due to drainage and bubble rupture. Although starting at different foam volume levels as discussed above, all foams exhibited a fast decay in volume within 10-15 min of aging and then remained fairly stable for about 1 h until they almost completely decayed within 10 h. The foams made from protein solution pretreated at 100°C and from solution at pH4 with added protein precipitates (= aggregates > 1 μm) did not completely decay within 10 h and we attribute this to the presence of aggregated proteins (Fig.4.A3). In a previous study, the stability of ß-lactoglobulin stabilized foam was also found to increase with the size of protein aggregates (Dombrowski et al., 2016). These findings support the hypothesis that big aggregates promote foam stability by blocking the plateau channels for drainage and/or preventing coalescence due to interlamellar structure formation (see also Chapter 3.3.).

The foam volume produced from the protein solution with 50 mmol/l added sodium chloride decreased most abruptly down to 10% of the initial foam volume between 1 and 3 h foam age.

At increased ionic strength, the electrostatic repulsion between the protein layers adjacent to interfaces of neighboring bubbles is reduced and presumably allows for faster thinning and rupture of the lamellae.

Also, the addition of 0.01 vol% CMC to the protein solution enhanced foam collapse, the foam volume decreased by 85% between 2 h and 4 h. It should be noted that the addition of CMC does not alter the ionic strength of the protein solutions as confirmed by electrical conductivity data (Table A1).

The foamed emulsion with 3% sunflower seed oil exhibits no decrease in foam volume. Similar to solid particles, the emulsion droplets were found to accumulate within the foam Plateau borders and inhibit foam drainage in a previous study (Koczo et al., 1992).

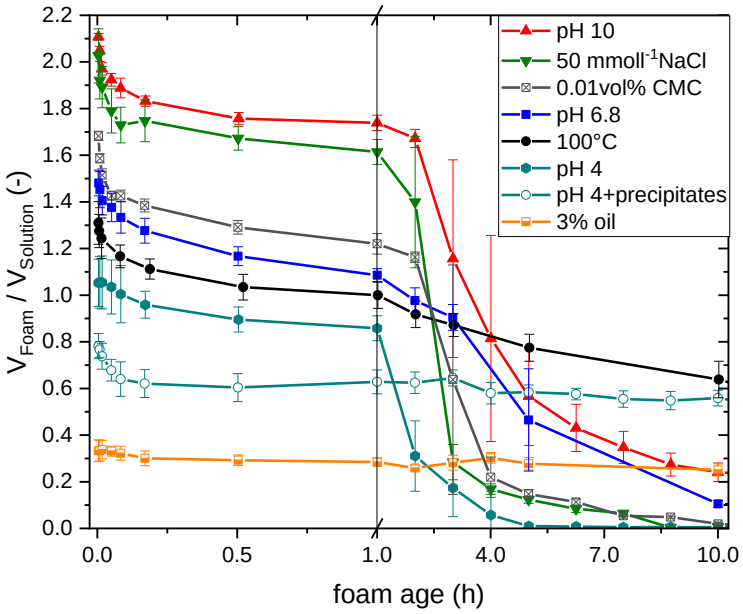

Figure 4.3 Foam volume relative to volume of foamed 10 g/l lupin protein solutions versus foam age at various pH, at IEP with additional 8 g/l protein precipitates, after heat treatment of the solution, with additional 50 $mmoll^{-1}$ sodium chloride, with 0.01 vol% CMC, and 3% sunflower seed oil in emulsion, respectively.

4.3.3 Foam gas volume fraction and bubble size distribution

In order to study the structure and rheology of foams made from lupin protein solutions we used a pneumatic device to purge nitrogen through a glass membrane with narrow pore size at a constant flow rate similar as described in (Lexis and Willenbacher, 2014a). This preparation method provides little energy input and uniform foaming conditions. It has been used previously in various studies on foams made from β-lactoglobulin (Bals and Kulozik, 2003a; Engelhardt et al., 2013).

In Figs.4A1 and A2, gas volume fraction and Sauter bubble radius of foams created pneumatically are displayed versus temperature of the protein pretreatment. The gas volume fraction of foams made from 10 g/l protein solutions seems to exhibit a weak maximum at 70°C corresponding to a maximum in interfacial elasticity (see Table 4.A1), but the variation is within experimental uncertainty. Foams produced from lupin protein isolate solution, pretreated at 50°C, exhibited lower gas volume fraction when protein concentration was doubled (Fig.4.4A black half-filled square) and gas volume fraction was further reduced when 30 g/l protein precipitates were present in the solution (Fig.4.4A1 red half-filled square). This is consistent with earlier studies pointing out, that protein agglomerates bigger than a few hundred nanometers play a role in foam stabilization as they can reduce drainage by blocking plateau channels (Fameau and Salonen, 2014; Lazidis et al., 2017). The Sauter radius of foam bubbles weakly increased when pretreating the solutions at temperatures ≥50°C leading to protein denaturation. Also, the presence of additional precipitates neither affected the Sauter radius nor the bubble size distribution.

The effect of pH on initial gas volume fraction and Sauter bubble radius is shown in Figs.4B1 and B2. These data indicate that both quantities are essentially independent of pH. In contrast to the manually shaken samples, the pneumatically produced foam made with solution at pH 4 started to collapse after 10 minutes. It was the only solution investigated in this study which did not fulfill Gibbs' stability criterion, stating that bubbles are stable to disproportionation when the interfacial elasticity is greater than half the interfacial tension (Lazidis et al., 2017). In contrast, the foam of a protein solution with pH 4 containing protein precipitates exhibited a lower gas volume fraction (Fig.4.4B1 blue square) but did not show bubble rupture during the observation time of 15 min.

Figs.4C1 and C2 show the initial gas volume fraction and Sauter bubble radius for foams made from protein solutions of different ionic strength. Whereas foaming capacity strongly increased with increasing salt concentration in the foaming solution, gas volume fraction was hardly affected and Sauter bubble radius seemed to drop only slightly.

Figs.4D1 and D2 displays the gas volume fraction and Sauter bubble radius of the foam versus the CMC concentration in the foaming solution. Whereas the added CMC induced only a weak increase of gas volume fraction, the higher CMC concentration corresponding to a tenfold increase in viscosity (see Tab.A1), however, resulted in almost a doubling of the Sauter bubble radius. The reason for this may be twofold. First, the diffusion of the protein to the interface is slowed down by the high viscosity of the continuous phase and bubbles coalesce directly after their formation before their interfaces are stabilized by proteins ((Bals and Kulozik, 2003b). Second, complex formation between CMC and proteins may reduce the effective, available protein concentration and consequently only a smaller interfacial area corresponding to a larger bubble size could be stabilized.

The foam produced from the emulsion including 3 wt% dispersed oil droplets exhibited similar gas volume fraction and Sauter bubble radius as the foam made from the protein solution without oil (Figs.4D1 and D2 crossed squares).

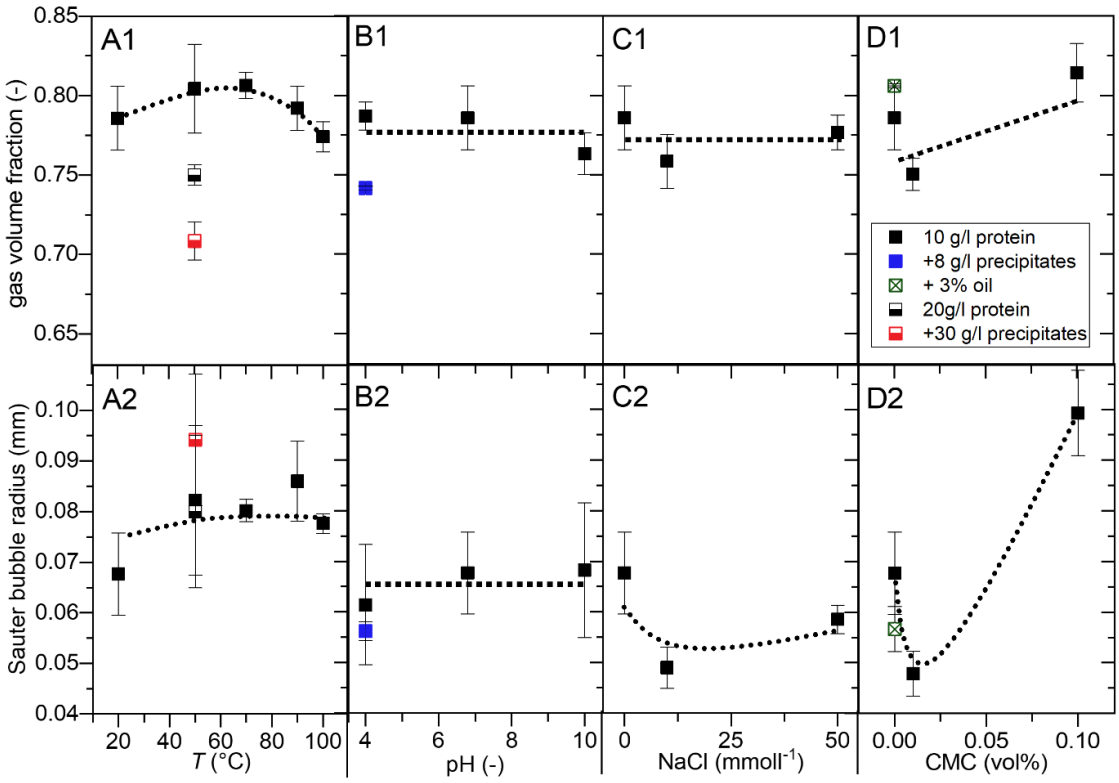

Figure 4.4: Initial gas volume fraction and Sauter bubble radius of foams made from lupin protein solutions versus (A) pretreatment temperature, (B) solution pH, (C) sodium chloride concentration, (D) sodium carboxymethyl cellulose (CMC) concentration Gas volume fraction and Sauter bubble radius of foams made 3 wt% sunflower seed oil emulsified in lupin protein solution are shown (crossed symbols in D). The solutions' protein concentration is 10 g/l, except for samples containing additional protein precipitates (colored symbols in A and B). Lines are to guide the eye.

The time evolution of the Sauter bubble radius and the gas volume fraction of foams are displayed in Figs.5A and Fig.4.5B, for different CMC concentrations in the protein solutions. The addition of 0.01 vol% CMC resulted in a slight reduction of the Sauter bubble radius and gas volume fraction, as shown above (Figs.4D1 and D2). However, the growth rates of both quantities up to 15 min foam age were not affected by the addition of 0.01 vol% CMC. When 0.1 vol% CMC was added to the protein solution, the initial Sauter radius was significantly increased (see also Fig.4.4D2), however, it hardly increased over time and the same is true for the gas volume fraction. At high CMC concentration, i.e. high solution viscosity (TableA1), the drainage is slowed down significantly, and the foam structure is more stable.

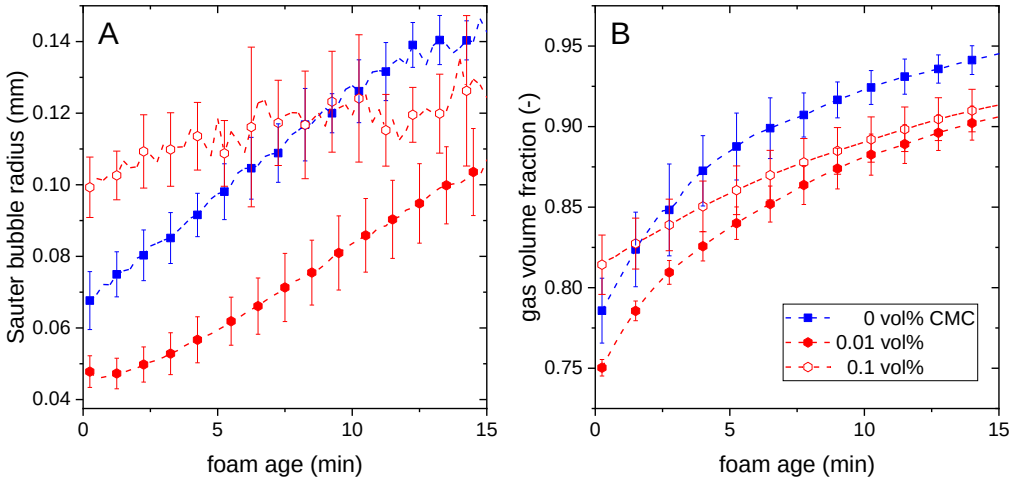

Figure 4.5: (A) Gas volume fraction and (B) Sauter bubble radius of foams made from lupin protein solutions with various sodium carboxymethyl cellulose (CMC) concentration versus foam age.

The volume-based bubble size distribution of foams made from lupin protein solutions pretreated at 50°C are shown in Fig.4.6A for 15 s and 10 min foam age. The foams were produced from solutions of lupin protein isolate before and after separation of protein precipitates with 20 g/l dissolved protein. At a given time, the cumulative distribution was the same for foams with and without protein precipitates. For the foam made from 20 g/l protein solution free of precipitated protein aggregates > 1 μm the density histogram is also shown in Fig.4.6A. A monomodal initial bubble size distribution which not only shifts to higher values but also proportionally broadens with increasing foam age is seen here. Such a monomodal initial size distribution and a subsequent broadening with constant span $(r_{90}\text{-}r_{10})/r_{50}$ of 1 ± 0.3 (see Chapter 2.9) was observed for all foams investigated in this study.

In Fig.4.6B, the gas volume fractions of foams made from lupin protein solutions pretreated at 50°C versus the foam age are shown. In the presence of aggregated protein precipitates, not only the initial gas volume fraction was decreased but also its growth rate was lower than in foams produced from the same solution after separation of the precipitates.

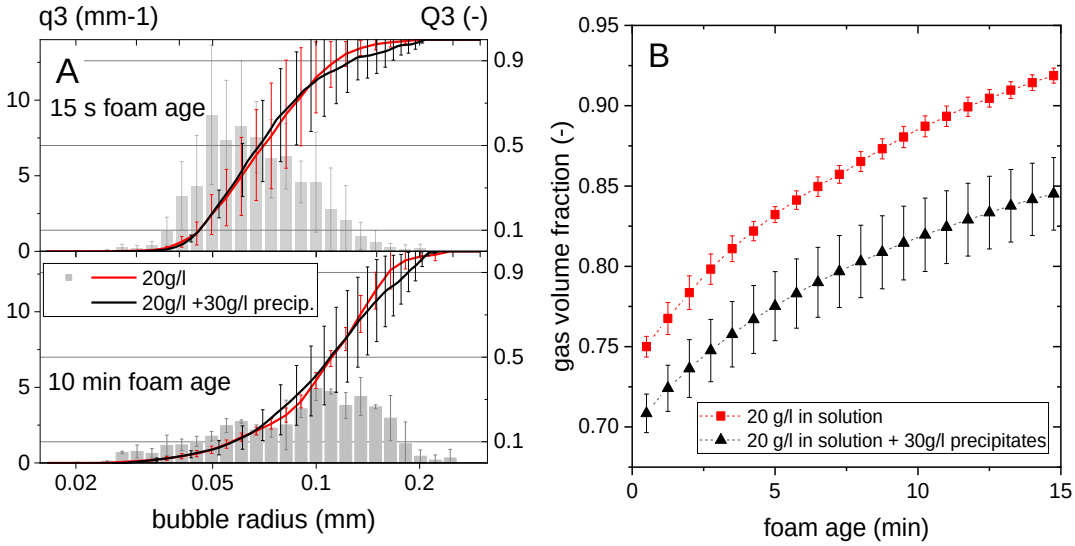

Figure 4.6: (A) The density histogram of the bubble sizes and the cumulative distribution at 15 s and 10 min foam age of foams made from supernatants of lupin protein isolate solutions with 20 g/l dissolved protein, centrifuged after pretreatment at 50°C, as well as cumulative bubble size distributions for a protein isolate solution, pretreated at 50°C, containing 20 g/l dissolved proteins and 30 g/l aggregated protein precipitates. (B) Gas volume fraction versus foam age of corresponding foams.

In Fig.4.7, an endoscopic image of a lupin protein stabilized foam is shown. This foam was made from a solution containing 10 g/l dissolved protein and 8 g/l protein precipitates stained in red. A Coomassie blue solution was dripped onto the foam top and drained through the foam in the direction of gravity. The stained draining liquid was evidently detained were protein precipitates blocked plateau channels. This observation provides direct proof of the hypothesis discussed above, that aggregates sufficiently big to hinder drainage by blocking plateau channels can stabilize protein foams significantly.

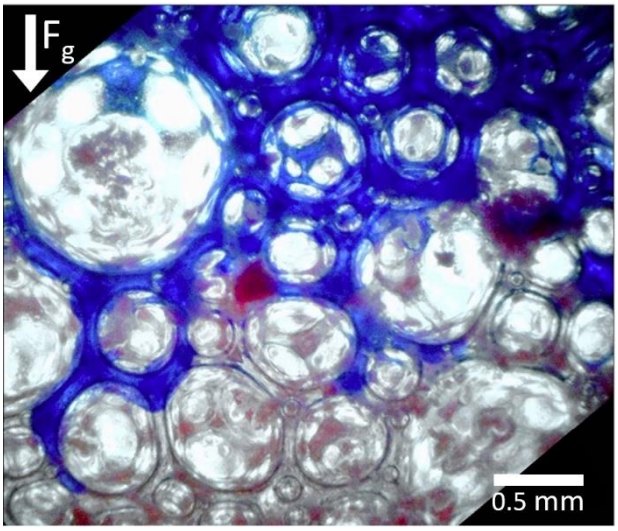

Figure 4.7: Endoscopic image of video observation (link to the video: endoscopic foam drainage observation) of foam produced from lupin protein solution with pH 4 with protein aggregates blocking plateau borders, stained in red. The solution drainage pathway is visualized with Coomassie blue solution dripped onto the foam.

4.3.4 Foam yield stress and elastic modulus

Figs.8A1 and A2 show yield stress and elastic modulus normalized to the Laplace pressure for foams produced from solutions with 10 g/l protein exposed to different heat pretreatment at 85% to 86% gas volume fraction. Both quantities seem to increase when the protein solution was exposed to temperatures greater 50°C. The differences were small though and the increase in yield stress and elastic modulus was significant only when comparing 20°C and 100°C pretreatment temperature. The normalized yield stress and elastic modulus of foams with 20 g/l protein as well as with additional 30 g/l precipitates are slightly decreased because they reach 85% gas volume fraction at higher foam ages corresponding to broader bubble size distribution (see Figs.8A1 and A2 half-filled squares). We assume the combination of proteins <10 nm, accessible for fast interfacial stabilization, and the highest fraction of aggregates greater 100 nm in the solution pre-treated at 100°C (see Fig.4.A3A) forming interlamellar structures promote the observed foam stiffness.

The normalized yield stress and elastic modulus of foams made from solutions of different pH are shown in Figs.8B1 and B2. The normalized foam elastic modulus was essentially independent of pH, whereas the normalized yield stress exhibited a maximum with pH 6.8 in the foaming solution. If protein precipitates were additionally present in the solution with pH4 the foam yield stress was as high as in foams made from protein solution at pH 6.8 and the elastic modulus was even higher (blue symbols in Figs.8B1 and B2). We attribute this to, protein aggregates big enough to form interlamellar structures that increase the foams' strength and yield stress by preventing bubbles from sliding past each other.

The normalized foam yield stress and elastic modulus versus the amount of sodium chloride added to the protein solution is depicted in Figs.8C1 and C2. The elastic modulus is essentially independent of the ionic strength of the foaming solution, whereas the yield stress is significantly increased upon addition of 50 mmol/l sodium chloride. The corresponding reduction in the range of electrostatic repulsion seems to result in a predominantly attractive interaction among adjacent protein layers finally resulting in an increased yield stress (Davis et al., 2004; Lexis and Willenbacher, 2014b; Razi et al., 2019)(Davis et al., 2004; Lexis and Willenbacher, 2014b; Razi et al., 2019).

The normalized foam elastic modulus and yield stress versus CMC concentration in the foaming solution is shown in Figs.8D1 and D2. Increasing the CMC concentration, i.e. increasing viscosity, led to a monotonic decrease of foam elastic modulus and yield stress. This is in contradiction to Eq.4.1 and Eq.4.2 predicting a weak increase in yield stress with increasing solution viscosity and a foam elastic modulus independent of solution viscosity. The normalized yield stress and elastic modulus of the foam made from emulsions of lupin protein solution with 3 wt% sunflower seed oil is also shown in Figs.8D1 and D2 (crossed square symbols). Adding the oil led to a drastic drop of both quantities. In both cases, when viscosity is increased by CMC or when oil droplets are present in the continuous phase, we assume the protein diffusion and thus stabilization of freshly created interfacial area is hindered. Also, the fraction of freely diffusing, surface-active proteins in the solution may be reduced due to adsorption of proteins at the surface of the oil droplets or due to the formation of protein/CMC complexes. These phenomena may promote bubble coalescence, and bubble rupture may occur when bubbles get deformed during rheological measurements. Thus, the gas volume fraction may quickly decrease from the initially set value in these systems and the measured yield stress and elastic modulus data seem to be lowered apparently for this highly shear sensitive foam.

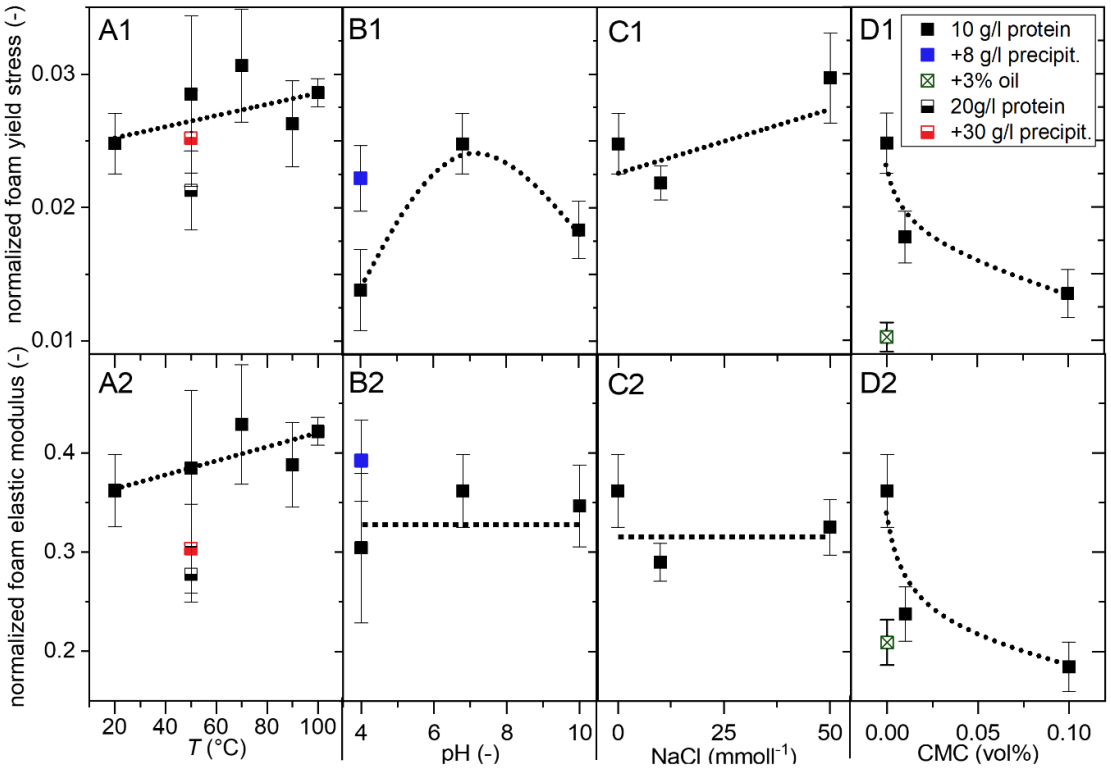

Figure 4.8: Yield stress and elastic modulus normalized by bubbles' Laplace pressure σ/R_{32} of foams at 85% to 86% gas volume fraction made from lupin protein solutions versus (A) pretreatment temperature, (B) solution pH, (C) sodium chloride concentration, (D) sodium carboxymethyl cellulose (CMC) concentration. Lines are to guide the eye.

Fig.4.9 shows the yield stress versus foam age of foams made from lupin protein solutions pretreated at 50°C before and after separation of protein precipitates. The yield stress of the foams exhibited an increase caused by the increasing gas volume fraction during foam drainage (see Fig.4.6B). The foam produced from the protein solution with additional protein precipitates had a lower initial yield stress in accordance to its lower gas volume fraction at the same foam age. The increase in yield stress was slowed down with growing foam age since the increase of the gas volume fraction was partially compensated by the increasing Sauter radius, cf. Eq.4.1 $\tau_y \sim \sigma/R_{32}$ $(\varphi-\varphi_c)^2$. Solid lines in Fig.4.9 display the evolution of yield stress calculated from the corresponding interfacial tension, Sauter bubble radius and gas volume fraction of the foams using Eq.4.1. The critical gas volume fraction was set to the volume fraction of randomly close packed monodisperse spheres of 0.635. With k set to 0.7, the calculated yield stress curve for foam produced from the protein solution with additional protein precipitates fits the measured data reasonably well. The yield stress curve for foam free of protein precipitates calculated with k=0.5, fits the measured yield stresses up to 7.5 min foam age. At higher foam ages the foam became too dry for rheological measurements and bubble rupture occurred when it was sheared.

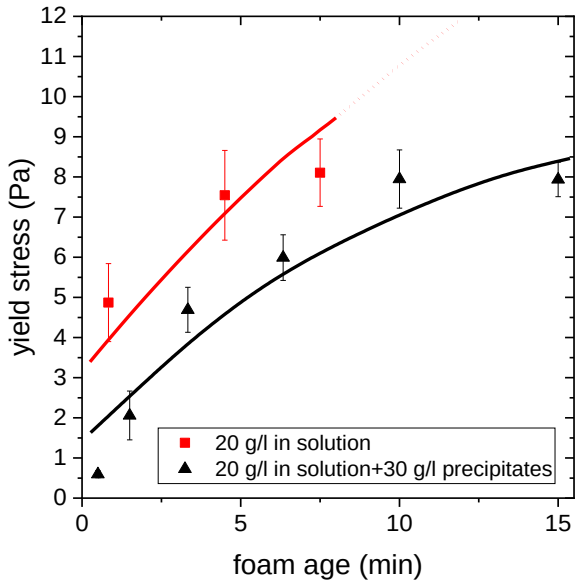

Figure 4.9: Foam yield stress foam versus foam age of foams made from supernatants of lupin protein isolate solutions with 20 g/l dissolved protein, centrifuged after pretreatment at 50°C, as well as a protein isolate solution, pretreated at 50°C, containing 20 g/l dissolved proteins and 30 g/l aggregated protein precipitates. Solid lines show the calculated yield stress according to Eq.4.1: $\tau_y = k\,\sigma/R_{32}\,(\varphi-\varphi_c)^2$, with k=0.5 for 20 g/l dissolved protein and k=0.7 for 20 g/l dissolved proteins and 30 g/l aggregated protein precipitates.

4.3.5 Effect of aggregates and interfacial elasticity on foam rheology

Fig.4.10A displays the yield stress normalized to the respective Laplace pressure inside the foam bubbles for all lupin protein foams investigated in this study versus $(\varphi-\varphi_c)^2$, as suggested by Eq.4.1. Fig.4.10B shows the normalized foams' elastic shear modulus versus $\varphi(\varphi-\varphi_c)$, as suggested by Eq.4.2. The critical gas volume φ_c fraction was set to 0.635, i.e. the volume fraction of randomly close packed monodisperse spheres. For surfactant stabilized emulsions and foams the pre-factors in Eq.4.1 and Eq.4.2 have been treated as numerical constants and values of $k\approx0.5$ and $a\approx1.5$ were reported in the literature (Marze et al., 2009; Mason et al., 1996, 1995). The absolute values of the data for the lupin protein foams lie in the range predicted by Eq.4.1 and Eq.4.2, respectively. The normalized elastic modulus values follow the $\varphi(\varphi-\varphi_c)$ scaling given in Eq.4.2 with $a\approx1.5$. The yield stress data follow the $(\varphi-\varphi_c)^2$-scaling predicted by Eq.4.1 with pre-factor $k\approx0.5$ reasonably well. The strong scatter in the data may be due to an additional contribution of interfacial elasticity to the foam yield stress as already observed for β-lactoglobulin foams (Lexis and Willenbacher, 2014b).

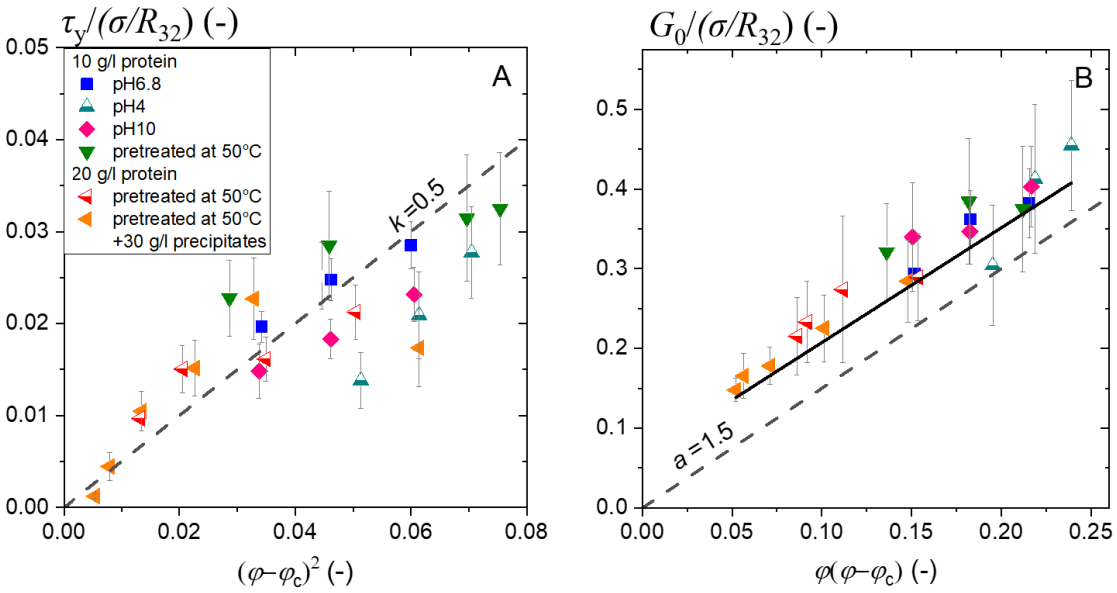

Figure 4.10: (A) Yield stress of foams made from lupin protein solutions and emulsion normalized to Laplace pressure σ/R_{32} versus $(\varphi-\varphi_c)^2$, with the gas volume fraction φ and the critical bubble packing fraction φ_c is set to 0.635. Dashed line shows the identity function times k, with k=0.5. Solid lines show linear fits to the data with $R^2 > 0.98$. (B) Plateau elastic modulus of foams made from lupin protein solutions and emulsion normalized to Laplace pressure σ/R_{32} versus $\varphi(\varphi-\varphi_c)$. Dashed line shows the identity function times a, with a=1.5. Solid line shows a linear fit to the data with R^2=0.92.

According to Eq.4.1 and Eq.4.2, the foams yield stress and elasticity should vanish at gas volume fractions close to the critical bubble packing fraction and foams behave like purely viscous fluids when bubble contacts become too few and no attractive interactions among bubbles are present forcing the formation of a sample spanning network (Saint-Jalmes and Durian, 1999). However, in Fig.4.10B the linear fit to the normalized modulus data suggests considerable elasticities at $\varphi-\varphi_c = 0$. We hypothesize that this apparently unphysical phenomenon is due to inadequate normalization of the elastic shear moduli by the static equilibrium interfacial tension. The interfacial tension present along the bubbles' interfaces may change when they are dilated and compressed in foams subject to shear and this interfacial tension change is characterized by the interfacial elasticity. As the protein solutions exhibited significant interfacial elasticity, we expect the latter to counteract bubble deformation and thus contribute to the yield stress and to the elastic shear moduli of the foams. This hypothesis is supported by the correlation between the normalized foam yield stress and elastic modulus data with the interfacial elastic modulus of the corresponding protein solutions (Table4.A1) shown in Fig.4.11. This is in line with previously investigations relating foam and interfacial rheological properties of various foaming solutions (Lexis and Willenbacher, 2014b; Völp et al., 2020b) covering a broad range of interfacial elastic modulus values. Although the absolute interfacial elastic modulus data are only half as high as reported for bovine milk proteins a clear correlation between E' and the foam yield stress τ_y is found. For the foam modulus G_0, however, this correlation is less obvious.

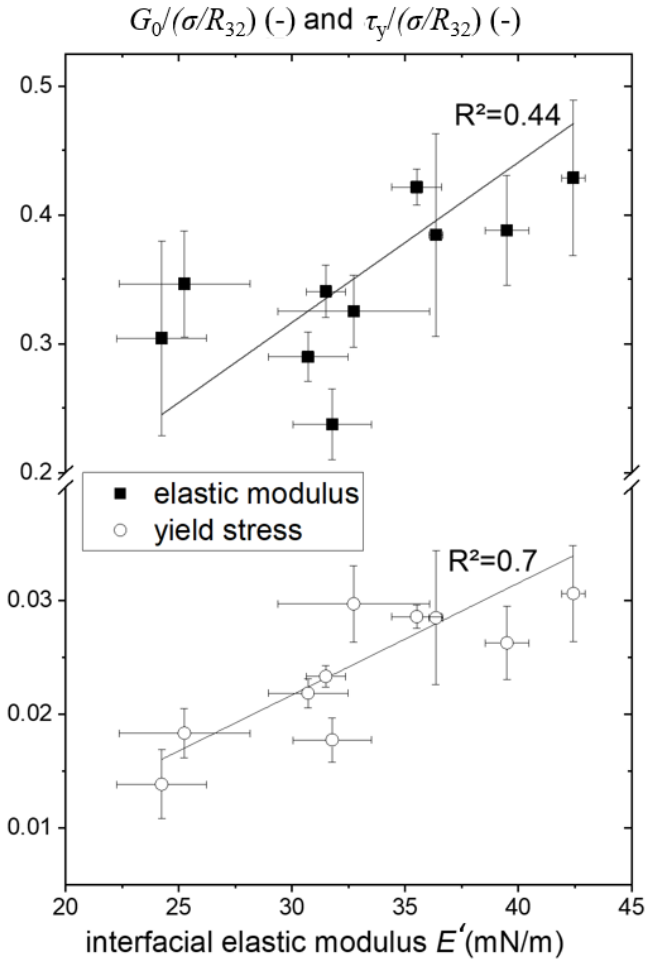

Figure 4.11: Yield stress τ_y and elastic modulus G_0 of foams at 85% to 86% gas volume fraction made from 1% lupin protein solutions normalized to bubbles' Laplace pressure σ/R_{32} versus interfacial elastic modulus *E'*. Displayed data for *E'* are average values and the error bars absolute deviations from two measurements with independently prepared solutions. Solid lines show linear fits to the data.

4.3.6 Lupine "plant milk" performance

We formulated a milk-like emulsion comprising 3 wt% oil, lupin protein solution prepared at 50°C, containing 20 g/l protein after separation of protein precipitates, and 0.1 vol% CMC. In contrast to the emulsion examined in shaking or pneumatic foaming experiments, the protein solution was not diluted to 10 g/l prior to emulsification because usually a higher protein content is set in milk like beverages. Foam was produced from this lupin "plant milk" in a commercial milk whipper (Nespresso Aeroccino 4, Nespresso S.A., Lausanne, Switzerland) as described in 2.13. Fig.4.12A clearly shows, that the time evolution of foaming capacity and gas volume fraction for this lupin "plant milk" is very similar to that of ultra-high temperature bovine milk with 3.6% fat and 33 g/l protein (Völp et al., 2020b).

Also, the foam stability did not differ during the observation time of 15 minutes. The yield stress and the bubble Sauter radius of both foams is displayed in Fig.4.12B. These data were obtained when the gas volume fraction had reached a quasi-stationary value at 300 s foam age. The yield stress of the lupin "plant-milk" foam was slightly higher than that of the bovine UHT milk foam. Consistent with the lower Sauter radii of the bubbles, the product $\tau_y R_{32} \approx 1.6$ is equal for both foams. Fig.4.12C shows the visual appearance of the "plant-milk" foam. The foam displays a smooth surface with bubbles smaller than the eye's resolution capacity (< 300 µm) and a strength that allows to form a foam pile. These preliminary results suggest that lupin proteins are a promising base for the formulation of vegan created food products. It should be noted that the foaming capacity achieved with this commercial whipper is much higher than 30% initial foaming capacity found in manual shaking tests due to the higher energy input. In contrast, pneumatic foaming yielded stable foams similar to those obtained in the commercial whipper. The Sauter bubble radius was 25% smaller for the pneumatically produced foams However, the foam yield stresses obtained with both foaming techniques at 85% to 87% gas volume fraction was similar. In contrast to the foam produced pneumatically at room temperature, the foam in the whipper has a temperature of 35°C. The increased temperature may lead to a higher interfacial tension, as previously observed for whey protein (Rosario Rodríguez Niño et al., 2001), compensating the bigger Sauter bubble radius.

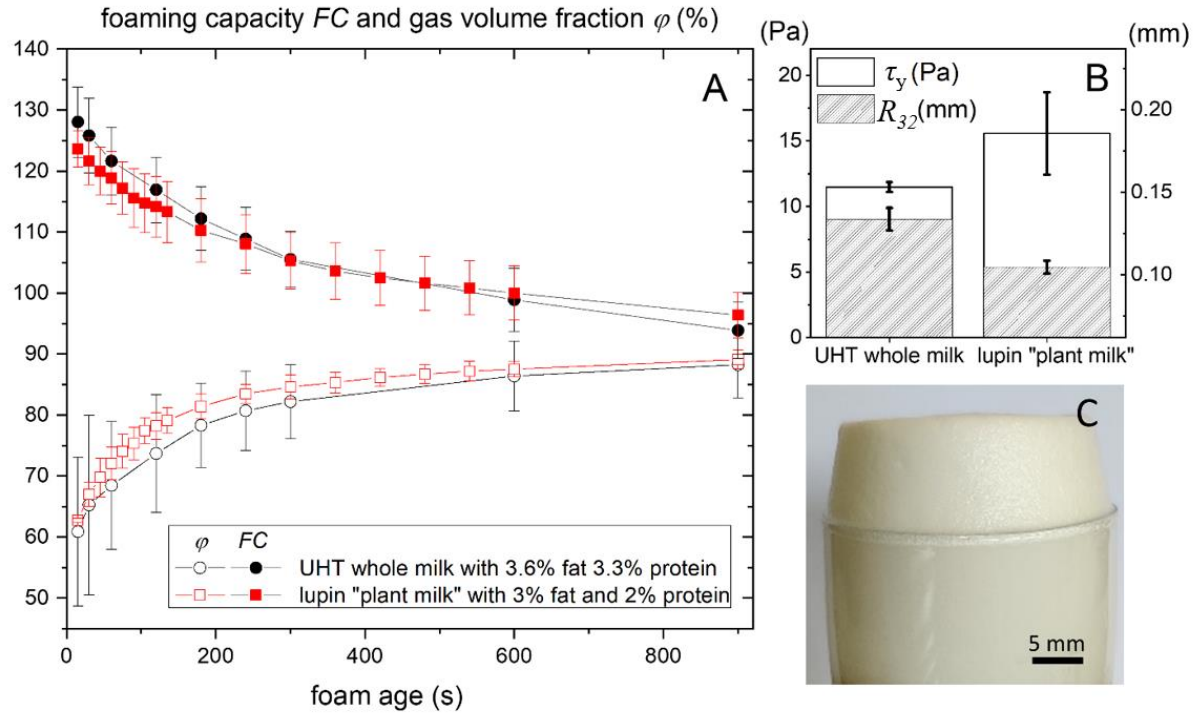

Figure 4.12: (A) Foaming capacity *FC* and gas volume fraction φ versus foam age of foams produced from 120 ml of bovine ultra-high temperature (UHT) whole milk and a "plant-milk" (3 wt% oil, 20 g/l lupin protein isolate, 0.01 vol% CMC) in a commercial milk whipper. (B) Foam yield stress and bubble Sauter radius measured at 300 s foam age at the same height inside the foams (i.e. 35 mm from the bottom of the milk whipper. (C) Image of lupin "plant-milk" foam. Data for bovine milk are taken from (Völp et al., 2020b).

4.4 Conclusion

The foamability of aqueous solutions of the water-soluble fraction of protein isolate from *Lupinus.angustifolius* seeds were investigated and the produced foams were characterized in terms of stability, gas volume fraction, bubble size distribution, as well as yield stress and elastic modulus. These foam characteristics were discussed in correlation to the interfacial tension and interfacial elastic modulus of corresponding protein solutions, also considering protein conformation and aggregation.

Interfacial tension of the lupin protein solutions varied in a narrow range irrespective of solution composition or heat treatment, and all lupin solutions exhibited a significant interfacial modulus. Our experiments indicate that the interfacial elasticity clearly has an effect on foam yield stress and elastic modulus. Similar findings have been previously reported for milk protein foams. The absolute interfacial elastic modulus values, however, here were only half as high as those reported for bovine milk protein solutions.

The structure and rheology of foams made from solutions of lupin protein isolate free of precipitates > 1 μm turned out to be surprisingly robust against temperature denaturation of the protein, although the protein conformation and size distribution were significantly affected by the denaturation temperature. Conformational changes in the protein were also induced by variation of pH. At pH4, which corresponds to the IEP, interfacial adsorption kinetics of the protein was accelerated but the equilibrium interfacial tension, was increased, due to protein aggregation in the bulk. Foaming capacity strongly increased with increasing pH, presumably due to partial unfolding of the proteins. Protein precipitates, e.g. forming at low pH, were shown to reduce the foam drainage and blocking of plateau borders was directly evidenced using optical microscopy.

Foaming capacity increased upon addition of sodium chloride, whereas the bubble size decreased. Substantially increasing the viscosity of the continuous phase by adding CMC, reduced foam drainage leading to more stable gas volume fraction and Sauter bubble radius in the foam, but it also reduced foamability. Stable emulsions of sunflower seed oil in lupin protein solution could be prepared but its foamability was quite poor and also foam yield stress and elastic modulus was low. Presumably, considerable amounts of lupin protein in the solution were consumed for oil droplet stabilization. Preparing a lupin protein “plant milk” with higher protein content and whipping it in a commercial milk foaming device, resulted in foaming capacity and foam texture similar to that of bovine whole milk.

In conclusion, our investigations demonstrate that lupin proteins may serve as a promising, robust base for the formulation of aerated vegan food products.

4.5 Appendix

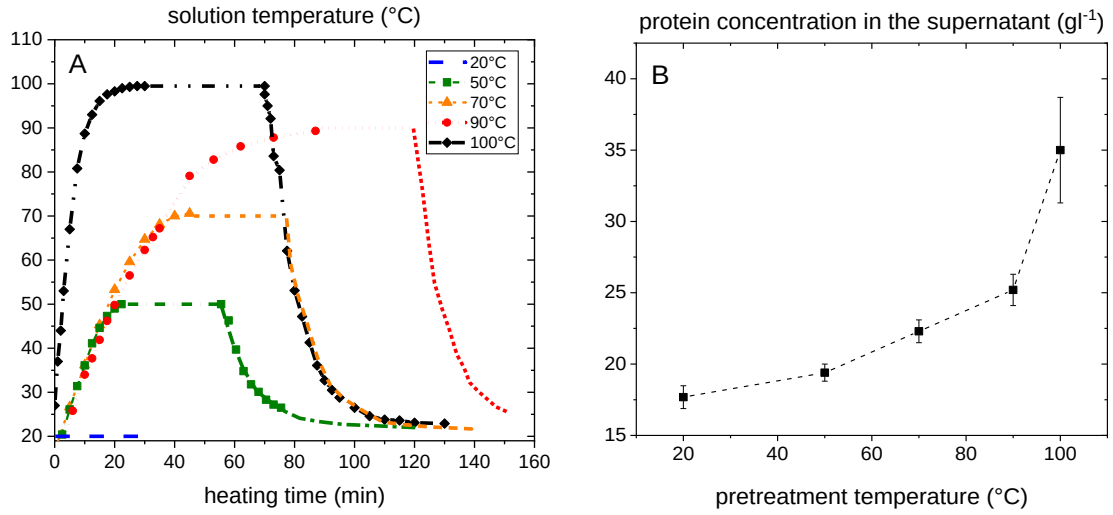

Figure 4.A1: (A) Temperature in lupin protein isolate solutions versus time during temperature treatment on a stirring plate (20°C blue dashed line, 50°C green squares, 70°C yellow triangles, 90°C red circles) or in a silicon oil bath (100°C black diamonds). Dashed lines show estimated temperatures. (B) Protein concentration in the supernatant of 5 % lupin protein isolate solutions versus maximum pretreatment temperature held for 30 min in the solutions prior to centrifugation at 8965 relative centrifugal force for 20 min.

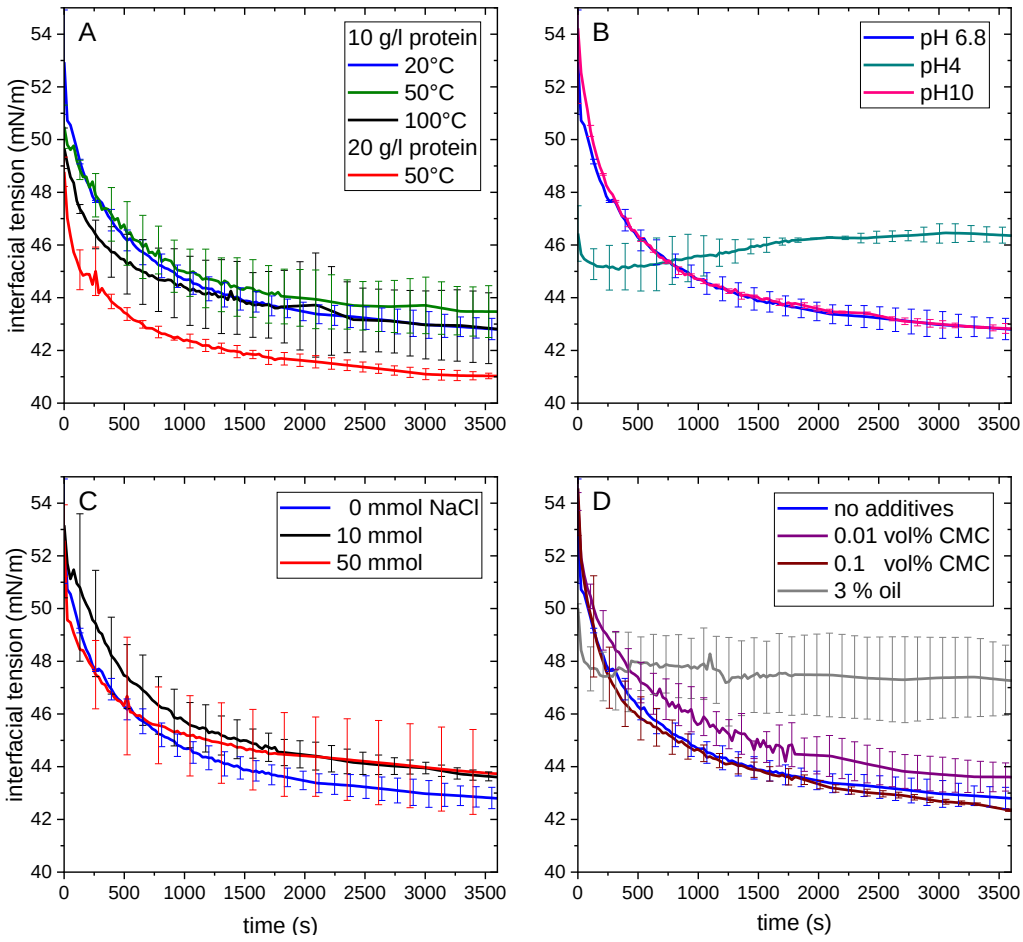

Figure 4.A2: Interfacial tension versus drop surface lifetime in pendant drop experiments with lupin protein solutions at various (A) pretreatment temperatures, (C) pH, (B) ionic strength, and (D) with sodium carboxymethyl cellulose (CMC) and with sunflower seed oil in emulsion. The protein concentration was 10 g/l if not stated otherwise. Displayed data are average values and the error bars absolute deviations from two measurements with independently prepared solutions

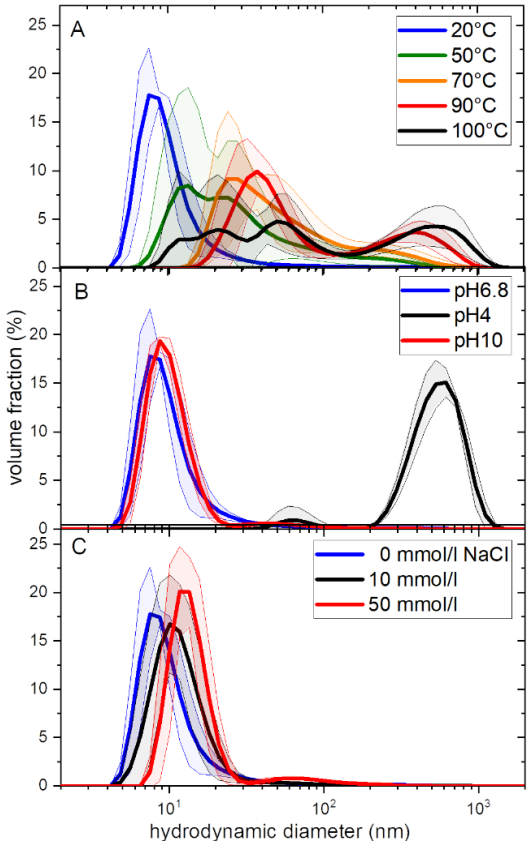

Figure 4.A3: Volume based size distributions of lupin protein aggregates in supernatants of protein isolate solutions at 1 % protein concentration (A) after heat pretreatment at various temperatures, (B) at pH 6.8, pH 4, and pH 10, and (C) after addition of various amounts of sodium chloride, measured using dynamic light scattering.

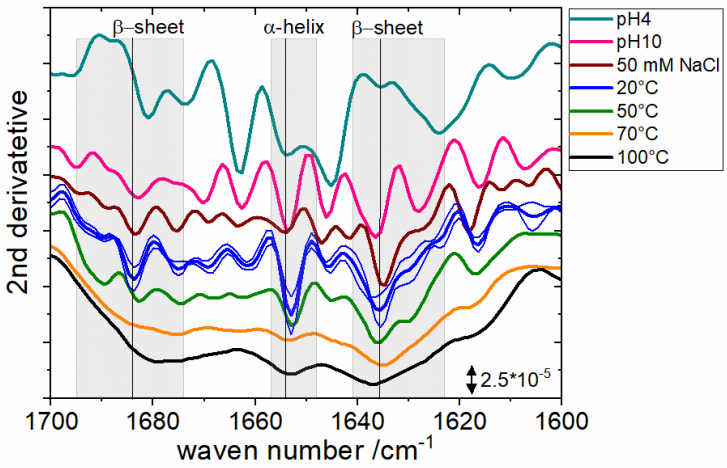

Figure 4.A4: Second derivative of the FT-IR adsorption spectrogram of lupin protein solution after heat treatment, and at different ionic strength and pH, respectively, versus wave number in the amide I adsorption range. The standard deviation for three independently prepared samples is displayed for the sample pretreated at 20°C (blue area). Average (straight lines) and standard deviation (grey bars) of the adsorption peaks of ß-sheet and α-helix secondary protein structure are displayed (Goormaghtigh et al., 1994).

Table 4.A1: Newtonian plateau viscosities, electrical conductivities and interfacial elastic moduli of lupin protein solutions

Sample specification	Viscosity /mPa s	Elect. conductivity /mScm^{-1}	Interfacial elastic modulus /mNm^{-1}
10g/l protein	1.45 ±0.04	1.5	32 ±1
10g/l protein heated to 50°C	1.49±0.06	1.3	36 ±0
10g/l protein heated to 70°C		1.3	42 ±1
10g/l protein heated to 90°C		1.2	40 ±1
10g/l protein heated to 100°C	1.44 ±0.04	1.1	36 ±1
20g/l protein heated to 50°C	1.49 ±0.06	2.3	29 ±2
10g/l protein with pH4	1.13 ±0.02	4.0	24 ±2
10g/l protein with pH10	1.31 ±0.05	2.4	25 ±3
10g/l protein + 10 mM NaCl	1.24 ±0.05	2.4	31 ±2
10g/l protein + 50 mM NaCl	1.20 ±0.04	5.9	33 ±3
10g/l protein + 0.01 vol% CMC	1.71 ±0.01	1.5	32 ±2
10g/l protein + 0.1 vol% CMC	12.3 ±0.45	1.7	32 ±3
10g/l protein + 3 wt% oil	1.52 ±0.08	1.4	38 ±5

5 Elasticity and yield stress of foams: Contribution of interfacial elasticity

Full title: Elasticity and yield stress of foams: Contribution of interfacial elasticity

Authors: Annika Ricarda Völp, Norbert Willenbacher

Status: submitted

Bibliografic data: Soft Matter, 2021, 17. Jg., Nr. 14, S. 3937-3944.

DOI: 10.1039/D0SM02246B

The link between interfacial elasticity of foaming solutions and the elasticity and yield stress of their aqueous foams is probed for a variety of surfactant, block-copolymer, protein, food, and particle-stabilized (Pickering) foams. We measured interfacial tension σ and interfacial elastic moduli of foaming solutions in dilation E_∞ as well as in shear G_i‘ at concentrations suitable for foaming and compared them to the shear modulus and yield stress of corresponding foams normalized by bubbles’ Sauter radius R_{32} and foams’ gas volume fraction. The interfacial shear modulus was only measurable for the foaming solutions including proteins or nanoparticles. For these systems the foam shear modulus scaled reasonably well with $(\sigma+2\ G_i')/R_{32}$. The interfacial dilatational modulus was accessible for all investigated systems and the foam shear modulus as well as yield stress scaled with a generalized Laplace pressure $(\sigma+2\ E_\infty)/R_{32}$. But foams stabilized by nanoparticles or aggregated proteins exhibited even higher shear modulus and yield stress values not captured by the proposed scaling with the generalized Laplace pressure and also show an unexpectedly high dependence of these characteristics on the gas volume fraction. We attribute this to attractive forces between particles and/or structure formation across the lamellae that become increasingly dominant as the lamellae narrow down during foam drainage.

5.1 Introduction

Foams and emulsions are complex disperse systems with unique texture and rheology. Though the individual phases are purely viscous, foams and emulsions display viscoelastic behavior when the dispersed phase exceeds the maximum packing fraction and the bubbles or droplets start to deform. Such foams and emulsions exhibit a yield stress, i.e. a critical stress at which neighboring bubbles or droplets rearrange topologically. Princen (Princen, 1982, 1979) concluded from a two-dimensional model of equally-sized hexagonal cells that the elastic modulus G' and yield stress τ_y of foams or emulsions exceeding the maximum packing fraction φ_c scale with the Laplace pressure within the cells, i.e. the ratio of interfacial tension σ and bubble or droplet radius R. For the two-dimensional case an analytical solution for the dependence of these rheological parameters on the dispersed volume fraction φ was derived. Based on experiments with polydisperse emulsions stabilized by a small molecular weight surfactant (ammonium laureth sulfate), Princen and Kiss (Princen and Kiss, 1986) established an empirical dependence of rheological parameters on (φ-φ_c) using $\varphi_c = 0.712$ close to the critical volume fraction $\varphi_c = 0.74$ of hexagonal close packed monodisperse spheres and suggested to express the bubble or droplet size in terms of the Sauter radius R_{32}. Mason et al.(Mason et al., 1996, 1995) refined the models suggesting the following semi-empirical equations:

$$G' = a\frac{\sigma}{R_{32}}\varphi(\varphi - \varphi_c) \tag{5.1}$$

$$\tau_y = k\frac{\sigma}{R_{32}}(\varphi - \varphi_c)^2 \tag{5.2}$$

Based on experimental data for carefully prepared monodisperse emulsions of silicon oil in water also stabilized with small molecular weight surfactant (sodium dodecylsulphate) they found numerical pre-factors $a = 1.64$ and $k = 0.51$, for the critical gas volume fraction they chose $\varphi_c \approx 0.635$ corresponding to randomly close packed monodisperse spheres. Marze et al. (Marze et al., 2009) confirmed the models to hold true for foams stabilized by small molecular weight surfactants (sodium dodecylsulphate; potassium cocoyl glycinate) and found numerical values $a = 1.53$ and $k = 0.62$ but stated that the elastic modulus of casein stabilized foams was lower than predicted from Eq.5.1. They related this conflicting behavior to the slower adsorption dynamics of the larger casein molecules, the viscoelasticity of the casein covered interface and thicker interfacial films. Dimitrova and Leal-Calderon(Dimitrova and Leal-Calderon, 2004) found substantially higher shear moduli for hexadecane-water emulsions stabilized with casein, ß-lactoglobulin and bovine serum albumin than known for sodium docecyl sulfate. They reported that G' values of those three emulsions increased with literature values for their corresponding interfacial dilatational elasticity E_A ranging from 9 to 26 mN/m. Davis et al. (Davis et al., 2004) tried to correlate the yield stress of whey protein foams with the dilatational interfacial elastic modulus of the foaming solution (varying from 15 to 80 mN/m) at various pH and ionic strength, but did not consider the foams' gas volume fraction nor the bubble size.

Lexis and Willenbacher (Lexis and Willenbacher, 2014b) found the elastic moduli of milk protein stabilized foams to increase with the surface elastic modulus in shear (varying from 5 to 100 mN/m) and in dilation (varying from 0.1 to 80 mN/m). The shear moduli of these foams exceeded the values predicted by Eq.5.2 by more than a factor of ten. They also correlated the foams' yield stress with the critical interfacial shear strain at which the interfacial layer structure breaks. Even higher foam elastic modulus and yield stress values, not captured by the correlation between foam and interfacial viscoelastic properties, were found under conditions favoring protein aggregation and were attributed to lamellae spanning structures. Tsibranska et al. (Tsibranska et al., 2020b) suggested the bulk elastic modulus of emulsions to scale with interfacial dilatational elastic modulus E_A >5mN/m as follows:

$$G' = 1.7\frac{\sigma}{R_{32}}\varphi(\varphi - \varphi_c)(1.5\ lgE_A) \qquad (5.3)$$

However, Eq.5.3 is based on a limited set of data comprising two hexadecane-water emulsions and one sunflower oil- water emulsion stabilized by saponins. Costa et al. (Costa et al., 2013) investigated the dependency of the complex shear modulus G^* of foams on frequency f and found deviations from the expected $G^* \sim f^{1/2}$ scaling for surfactant mixture solutions with high complex interfacial dilatational moduli E^*. At sufficiently high dilatational frequency exchange between the foaming agent at the interface and in the bulk is prevented and E^* reaches the limiting elasticity $E_\infty = E' = E_A$, while E'' tends to zero(Costa et al., 2013). Costa et al. assumed that the complex foam modulus G^* is related to the surface tension as well as the interfacial elasticity and suggested $G^* \sim \sigma/R_{32} + E_\infty/R_{32}$, omitting dimensionless pre-factors.

Based on these studies a contribution of the interfacial elasticity to the elastic modulus and yield stress of foams and emulsions should be taken into account. However, this is not considered in the widely used model equations describing foam elasticity and yield stress (Eqs.5.1 and 5.2), which were derived from investigations on emulsions and foams stabilized by low molecular weight surfactants lacking in substantial interfacial elasticity. We are not aware of any systematic investigation on the quantitative contribution of the interfacial elasticity to the foam elasticity or yield stress comprising of different types of foaming agents.

We determined the interfacial tension and interfacial elastic moduli of surfactant, block copolymer, and protein solutions, food systems and nanoparticle dispersions in shear as well as in dilation at amphiphile concentrations suitable for foaming. The elastic shear moduli and yield stresses of foams prepared from the same foaming solutions were measured and normalized to the respective bubble Sauter radii and gas volume fractions according to the suggested scaling in Eqs.5.1 and 5.2. The critical gas volume fraction was set to $\varphi_c \approx 0.635$ as suggested earlier (Marze et al., 2009). We correlated normalized shear modulus and yield stress values to the interfacial elasticity data and propose a quantitative contribution of the latter to the foam rheological characteristics yielding a refinement of Eqs.5.1 and 5.2.

5.2 Experimental

5.2.1 Solution preparation and interface characterization

Food systems, aqueous solutions of surfactants, block copolymers and proteins, and dispersions of nanoparticles were prepared as stated in Table 5.1. For reasons of readability, we refer to all these systems as foaming solutions in the following.

The gas/ liquid interfaces of the foaming solutions were characterized in oscillatory dilation at frequencies between 0.05 Hz and 0.67 Hz using the pendant drop method (PAT1, Sintaface) or in case of the block copolymer solutions, at frequencies between 0.1 and 3 Hz using the rising bubble method (Tracker, Teclis Scientific). The drop surface area varied between 10 to 30 mm², depending on the maximum drop volume of each foaming solution, respectively. After the equilibrium of the interfacial tension σ was reached, the surface area was dilated in oscillation with a deformation amplitude in the linear viscoelastic regime (max. 10% of the drop surface area) and stepwise increased frequency to obtain E_∞ (see exemplary frequency dependencies of E' in Fig.5.A1 under Footnotes). Since the increase in E' with frequency is weak at least for the highest frequencies accessible here, the values obtained at the maximum applicable frequency were treated as the equilibrium values E_∞. In shear, the solution surfaces were stressed in oscillation using a rotational rheometer (DHR3,TA Instruments) equipped with a double wall ring geometry (Vandebril et al., 2010) (70 mm ring diameter) at a frequency of 1 Hz and strains in the linear viscoelastic regime to obtain the interfacial elastic shear modulus G_i' (see exemplary strain dependencies of G_i' in Fig.5.A2 under Footnotes). Note, typically the interfacial elastic modulus is smaller in shear than in dilation(Cohen-Addad et al., 2013; Lin et al., 2018; Pagureva et al., 2016) and for several foaming solutions the elastic interfacial shear moduli were below the measuring limit of the rheometer. Furthermore, it should be noted that the interfacial modulus data were determined at the amphiphile concentrations used for foam preparation and thus should be treated as apparent values not necessarily matching the true interfacial elasticity of an amphiphilic monolayer.

Table 5.1: Foaming agents, their concentrations applied for foaming and interfacial elasticity measurements, and the preparation method of the foaming solutions or dispersions.

Foaming agent	Concentrations	Preparation
Glycolipid Sorbitol decenoate; Glycolipid Glucose 4-methyl-nonanoate	2 g/l 1.2 g/l	as described in(Hollenbach et al., 2020)
Block copolymer Poloxamer 407 (Sigma Aldrich)	0.05, 0.5 and 5 mM poloxamer in 0.1, 50 and 100 mM NaCl, respectively	dissolved in demineralized water at 20°C
Block copolymer Poloxamer 188 (Sigma Aldrich)	0.5 mM poloxamer in 50 mM NaCl	dissolved in demineralized water at 20°C
Guinness Stout beer		degassed; at 20°C
Whole milk powder (Nestlé)	10 wt.%	as described in(Völp et al., 2020b)
Bovine serum albumin (Santa Cruz Biotechnology)	1 wt.% at pH 6.8 in 0, 10, 50, 100 mM NaCl, respectively, and at pH4.7 (isoelectric point)	dissolved in demineralized water at 20°C
Lupine protein (Prolupin)	1 wt.% heat treated, at pH 4. pH 6.8, pH 10, and in 0, 10, 50 mM NaCl, respectively	as described in(Völp et al., n.d.)
Hexylamine coated silica nanoparticle 20 nm (LUDOX® TMA, Grace)	2.5 wt.% coated with 5, 50, and 70 mM hexylamine in 0, 10, 50 and 100 mM NaCl and 1 mM CaCl2, respectively	as described in(Carl et al., 2015)

5.2.2 Foam preparation and characterization

Foams were produced in glass filter funnels (16 - 40 µm pore size VitraPOR®Por.4, Robu) perfused by 60 ml nitrogen per minute as described in (Hollenbach et al., 2020; Lexis and Willenbacher, 2014a), except for the reconstituted whole milk foams, which were produced in a commercial milk whipper (Aeroccino4, Nespresso), as described in (Völp et al., 2020b). Recording of foam age was started once the filter funnel was completely filled with foam and the nitrogen flow was stopped or the whipper stopped the foaming process. The ratios between foam and solution conductivity during free drainage of the foams were measured at the center of the foam column using a rod-shaped electrode with 5 mm measuring gap width connected to a conductivity meter (Inlab731 and SevenCompact S230, Mettler Toledo).

The gas volume fraction φ of the foams was calculated from the relative foam conductivity κ as described in (Feitosa et al., 2005b):

$$\varphi = 1 - \frac{3\kappa(1+11\kappa)}{1+25\kappa+10\kappa^2} \quad (5.4).$$

The foams' Sauter radius R_{32} was determined from minimum 100 bubbles on images captured in the center of the foam column with an endoscope connected to a CCD camera (TVS80.280.BF6.AD10.2x-Zoom endoscope, Visitool and Lu 160 camera, Lumenera or VH-B55 endoscope and VHX-950F digital microscope, Keyence). The foams were illuminated from outside through the transparent container wall using a 600 lm LED lamp. The bubbles size distribution was automatically determined from the images without further processing using a template matching based bubble detection tool as described elsewhere (Völp et al., 2020a). The images were screened for similarities with circular templates differing in radius and the Sauter bubble radius R_{32} was calculated from the ensemble of detected bubbles. At specific foam ages corresponding to desired gas volume fractions between 0.85 and 0.95, foams were transferred into the gap of a plate-plate geometry and sheared in oscillation using a rotational rheometer (RheoScope 1, Thermo Fisher Scientific) at 1 Hz frequency and varying stress amplitude between 0.1 and 100 Pa as described in (Lexis and Willenbacher, 2014a). The gap width between the plates, which were 60 mm in diameter and covered with sandpaper to prevent wall slip, was set to 5 or 6 mm, but never less than ten times the maximum bubble diameter. Effects of wave propagation within the gap were negligible as the smallest possible wavelength was estimated to be about ten times larger than the gap width even for the smallest G' values measured at the selected oscillation frequency of 1 Hz (Ewoldt et al., 2015). As typical for highly concentrated, densely packed foams the frequency independent regime of G' was found at oscillation frequencies around 1 Hz (Marze et al., 2009) and the measured elastic moduli G' are termed shear moduli G_0. The foam yield stress was either measured with the same plate-plate setup or with a four bladed vane rotor (36 mm diameter, 9 mm height) submerged into the foaming apparatus as described in (Völp et al., 2020b). The shear stress was increased in 12 steps between 0.1 Pa 100 Pa and the deformation was recorded during a total measuring time of 60 s. The yield stress τ_y was determined from logarithmically plotted deformation versus shear stress data using the tangent intersection method (Willenbacher and Lexis, 2018). The results shown in the subsequent sections were determined from at least three measurements with freshly prepared foams, the displayed data are average values and the standard deviations are shown as error bars, error propagation was considered where applicable.

5.3 Results and discussion

The interfacial tension, σ and the interfacial elastic moduli in shear G_i' and dilation E_∞ of the foaming solutions are displayed in Table 2.

Table 5.2: Interfacial tension σ (max.4% error), interfacial elastic moduli in shear G_i' (max.33% error) and dilation E_∞ (max.22% error) in mN/m.

Foaming agent		σ	G_i'	E_∞
Sorbitol decenoate		26.6		3.3
Glucose 4-methyl-nonanoate		29.4		5.2
Poloxamer 407	0.05 mM Poloxamer	39.5		11.6
	+ 100 mM NaCl	41.1		12.5
	0.5 mM Poloxamer			
	+ 50 mM NaCl	39.3		10.9
	5 mM Poloxamer	38.6		8.6
	+ 100 mM NaCl	38.2		11.1
Poloxamer 188	0.5 mM Poloxamer			
	+50 mM NaCl	44.2		14.7
Guinness Stout		44.2		18.7
Milk powder		47		37.3
Bovine serum albumin	pH 4.7	53.1	8.8	73.2
	pH 6.8	52.3	12.1	56.6
	+ 10 mM NaCl	55.6	26.1	45.9
	+ 50 mM NaCl	55.2		64.8
	+ 100 mM NaCl	53.7		57.5
	+ 50 mM KCL	52		21.1
LPI	pH6.7 20°C	43.2		31.5
	+10 mM NaCl	42.9		30.7
	+50 mM NaCl	42.7		32.7
	50°C	41.9		36.4
	70°C	41.5		42.4
	90°C	41.3		39.5
	100°C	42.6		35.5
	pH4	46.5		24.2
	pH10	42.5		25.2
TMA	5 mM Hexylamin	63.5	58.6	
	50 mM Hexylamin	42.3	328	62.5
	+ 10 mM NaCl	39.6	391	78.3
	+ 50mM NaCl	43.8		139
	+ 100mM NaCl	40	816	115
	+ 1mM CaCl2	55.6		157
	70 mM Hexylamin	45.4	212	

Fig.5.1 shows the foam shear moduli normalized to the reciprocal bubble's Sauter radius R_{32}^{-1} and $\varphi(\varphi-\varphi_c)$ versus the equilibrium interfacial tension σ, the interfacial dilatational modulus E_∞ and the interfacial shear modulus G_i' of the foaming solutions, respectively. The critical gas volume fraction φ_c was set to 0.635 corresponding to randomly packed monodisperse spheres. Preliminary data analysis revealed that it was not feasible to determine φ_c from the measured bubble size distribution as suggested earlier [20] since the experimental uncertainty was too high and would have blurred the correlations between foam rheological quantities and interfacial elasticity of corresponding foaming solutions. The interfacial tension of the foaming agent solutions covers the range from 25 to 70 mN/m. The interfacial moduli of the same solutions vary in a much broader range from 2 to 200 mN/m in dilation and from about 10 to 1000 mN/m in shear.

The normalized shear moduli of the foams show no unique correlation with the equilibrium surface tension (Fig.5.1A). But clearly, the foam modulus increases monotonically with the dilatational modulus, as can be seen in Fig.5.1B, and according to Fig.5.1C also with the interfacial shear modulus of the foaming solutions, albeit to a weaker extend. The strong coupling of foam and interfacial modulus is demonstrated covering two orders of magnitude in interfacial modulus values.

Costa et al. suggest that the contribution of interfacial tension and interfacial elasticity superimpose linearly. Thus, we propose the following model:

$$G_0 = 1.6\frac{(\sigma + C\ G_i')}{R_{32}}\varphi(\varphi - \varphi_c). \qquad (5.5)$$

where C is a fitting parameter. Eq.5.5 reduces to the widely accepted model Eq.5.1 for $G_i' = 0$, as it is the case for small molecular weight surfactants. Fig.5.2 shows the normalized foam moduli versus σ+2 G_i'. With C = 2, Eq.5.5 fits the data for animal-based proteins and silica particles very well, covering two orders of magnitude in σ+2 G_i' and more than one order of magnitude in G_0. The high interfacial shear elasticity of particle dispersions is attributed to a strong interfacial network and jamming effects, occurring when the interface is sheared or compressed. However, for a given foaming solution. i.e. constant σ+2 G_i', strong differences between the normalized shear modulus data corresponding to foams with different gas volume fractions indicate additional physical mechanisms contributing to foam elasticity not captured by the interfacial elasticity. Proteins show lower interfacial shear elasticities but also form interfacial networks. This is indicated by the onset of non-linearity of G_i' at deformations <5% corresponding to network break-up. However, Eq.5.5 is not applicable to surfactant and block copolymer or lupin protein stabilized foams as these foaming agents do not exhibit measurable interfacial shear elasticities.

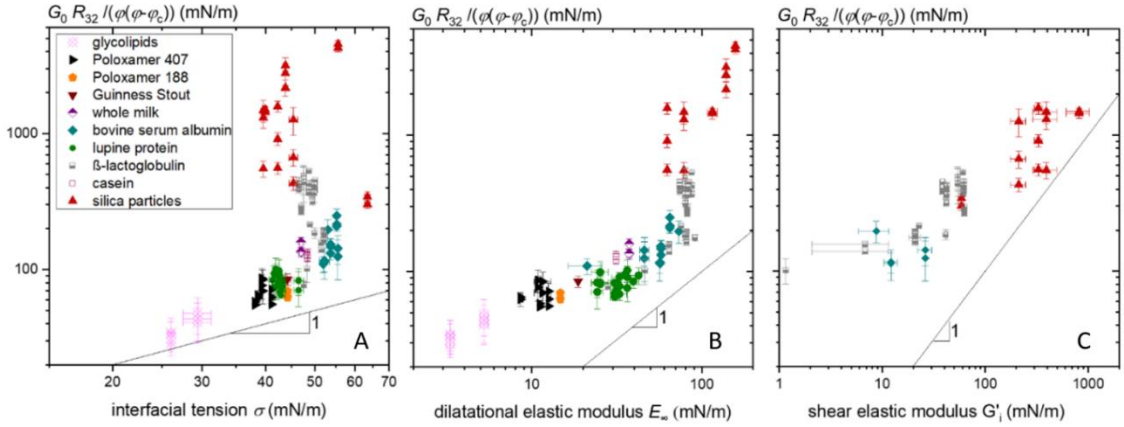

Figure 5.1: Foam elastic modulus G_0 normalized to the reciprocal bubble Sauter radius R_{32}^{-1} and $\varphi(\varphi-\varphi_c)$ versus (A) interfacial tension σ, (B) interfacial dilatational elastic modulus E_∞ and (C) interfacial shear elastic modulus G_i' of the corresponding foaming solutions. Data for ß-lactoglobulin were reused from (Lexis and Willenbacher, 2014b).

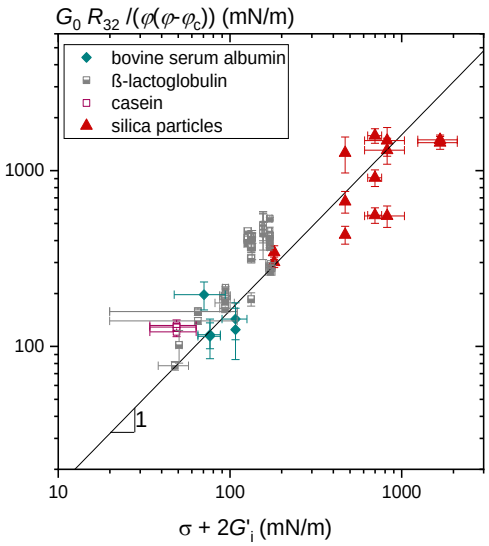

Figure 5.2: Foam elastic modulus G_0 normalized by the reciprocal bubble Sauter radius R_{32}^{-1} and $\varphi(\varphi-\varphi_c)$ versus the sum of interfacial tension σ and twice the interfacial shear modulus G_i' of the foaming solution. Solid line shows the linear relationship with the pre-factor 1.6. Data for ß-lactoglobulin were reused from (Lexis and Willenbacher, 2014b).

Foaming systems that do not show measurable interfacial shear moduli G_i' still exhibit high frequency dilatational elastic moduli E_∞. The dependence of normalized foam moduli and yield stresses on $\sigma+2E_\infty$ are depicted in Figs.5.3A and B, respectively. The correlation between the foam elasticity and $\sigma+2E_\infty$ is quite distinct for a broad variety of foaming agents. The foam yield stress also correlates with $\sigma+2E_\infty$ but less clearly.

Solving the differential equation for a sphere

$$E_A = A\frac{d\sigma}{dA} = \frac{R}{2}\frac{d\sigma}{dR} \tag{5.6}$$

yields the radius-dependent interfacial tension of a spherical bubble with an interfacial area A

$$\sigma(R) = \sigma_0 + 2E_A ln\left(\frac{R(t)}{R_0}\right) \tag{5.7}$$

with the initial interfacial tension σ_0, the initial radius R_0, and the radius $R(t)$ of the dilated bubble (Kloek et al., 2001). For $ln(R(t)/R_0)\approx 1$, $\sigma+2E_\infty$ reflects $\sigma(R)$ in Eq.5.7. For a sheared foam the deformation of the gas bubbles is more complex but qualitatively Eq.5.7 rationalizes why foam modulus and yield stress may scale with $\sigma+2E_\infty$ and accordingly $(\sigma+2E_\infty)/R_{32}$ may be termed generalized Laplace pressure.

The correlations shown in Figs.5.3A and B suggest the following model equations:

$$G' = a_d \frac{(\sigma+2E_\infty)}{R_{32}}\varphi(\varphi - \varphi_c) \tag{5.8}$$

$$\tau_y = k_d \frac{(\sigma+2E_\infty)}{R_{32}}(\varphi - \varphi_c)^2 \tag{5.9}$$

which fit the majority of the data with $a_d = 1$ and $k_d = 0.25$. Note that these pre-factors are slightly smaller than their analogues a in Eq.5.1 and k in Eq.5.2 derived for small molecular weight surfactants where E_∞ is neglectable.

However, the extremely high elasticities of foams stabilized by silica particles or aggregated proteins deviate from this scaling. Foam elasticity and yield stress in these cases are obviously not captured by the interfacial tension and its change upon interfacial dilation. They may be dominated by strong attractive forces within the stabilizing surface layers presumably resulting in structures spanning across foam lamellae. This is corroborated by the unusually strong dependence of foam modulus and yield stress on φ observed in these cases, exceeding the well-known scaling $\varphi(\varphi-\varphi_c)$ and $(\varphi-\varphi_c)^2$ observed for many surfactant or protein stabilized foams and emulsions by far. Recently synergetic effects between interfacial elasticity and strong attractive forces among emulsion droplets was reported to lead to high bulk elastic moduli (Tsibranska et al., 2020a). Such strong attractions among gas bubbles may also contribute to the high elastic modulus and yield stress values as well as their strong dependence on gas volume fraction observed here.

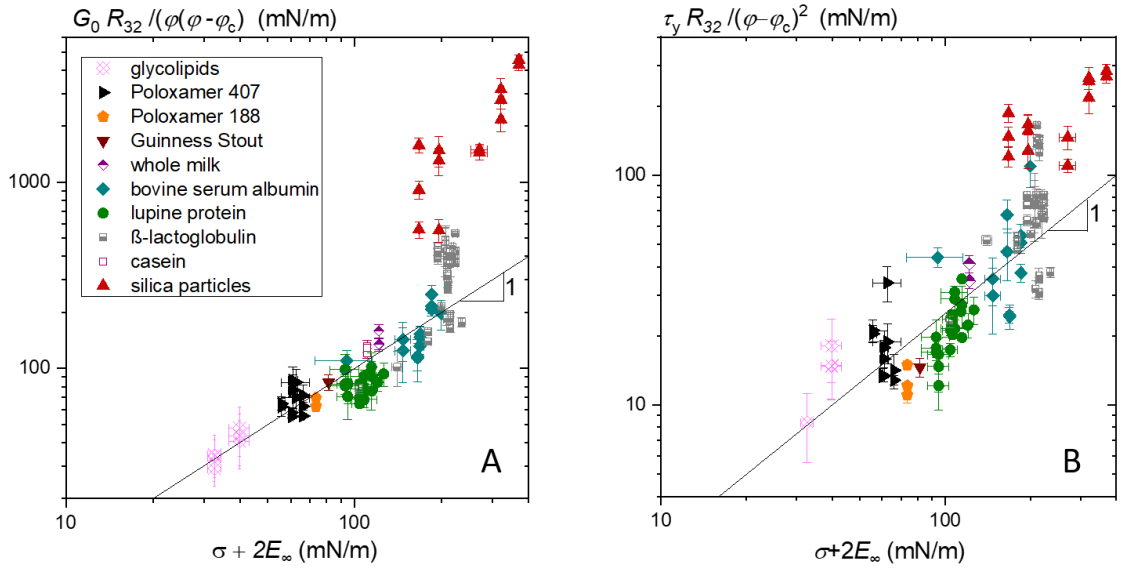

Figure 5.3: (A) Foam elastic modulus G_0 normalized by the reciprocal bubble Sauter radius R_{32}^{-1} and $\varphi(\varphi-\varphi_c)$ and (B) foam yield stress normalized by the reciprocal bubble Sauter radius R_{32}^{-1} and $(\varphi-\varphi_c)^2$ versus the sum of interfacial tension σ and twice the high frequency elastic modulus E_∞ of the foaming solution in dilation**.** Solid lines show the linear relationship with the pre-factor $a_d = 1$ in a) and $k_d = 0.25$ in (B)**.** Data for ß-lactoglobulin were reused from(Lexis and Willenbacher, 2014b).

This distinct dependency of the foams' elastic modulus and yield stress on gas volume fraction φ is shown in Figs.5.4A and B for foaming solutions of various ionic strength containing dissolved proteins or particles, respectively. For protein solutions without added salt, the foam elastic modulus increases with $\varphi(\varphi-\varphi_c)$ and yield stress increases with $(\varphi-\varphi_c)^2$ as predicted from model Eqs.5.7 and 5.8. When the ionic strength of the ß-lactoglobulin solution is increased, the foam elastic modulus and yield stress also obey the common φ-scaling but with increased pre-factors a_d and k_d. In case of particle stabilized foams, the elastic modulus and yield stress increase with $\varphi(\varphi-\varphi_c)$ and $(\varphi-\varphi_c)^2$ according to a scaling exponent ≈2. Hence our data indicate a stronger increase of foam elastic modulus and yield stress during drainage of foams stabilized by hydrophobized silica nanoparticles and under conditions allowing for a denser packing of the foaming agents at the interface, as it is the case for proteins at high ionic strength of the solution. Such protein aggregates are frequently considered as 'nanoparticles' and form highly stable foams since they are partially hydrophobic and small enough (<70 nm for ß-lactoglobulin) to adsorb onto the interface (Fameau and Salonen, 2014; Murray and Ettelaie, 2004). In former studies, high foam elasticity was attributed to interlamellar network formation of aggregated proteins (Lexis and Willenbacher, 2014a, 2014b). Accordingly, the stronger increase of the elastic modulus and yield stress with increasing gas volume fraction could be explained by compaction of these networks when the lamellae narrow down.

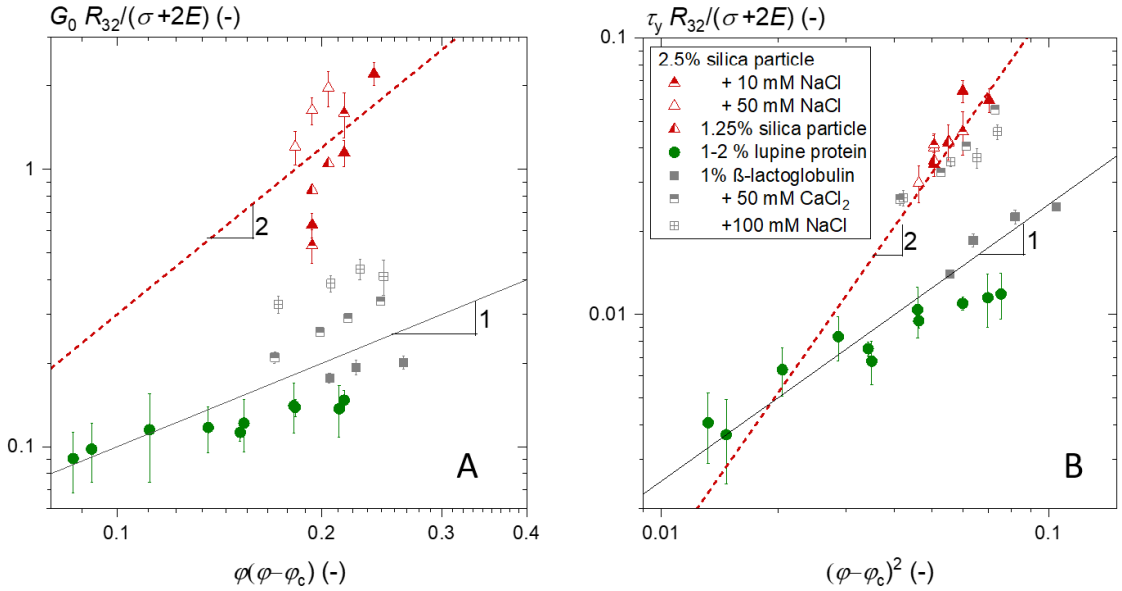

Figure 5.4: (A) Foam elastic modulus and (B) foam yield stress normalized by $(\sigma+2E_\infty)/R_{32}$ versus $\varphi(\varphi-\varphi_c)$ and $(\varphi-\varphi_c)^2$, respectively. Solid lines show a linear dependence and dashed lines show a quadratic dependence. Data for ß-lactoglobulin were reused from(Lexis and Willenbacher, 2014b).

5.4 Conclusions

We investigated close packed aqueous foams stabilized by a broad variety of amphiphiles, including glycolipid surfactants, block copolymers, plant- and animal-based proteins, as well as nanoparticles, in order to elucidate the coupling between foam flow and the interfacial elasticity of the corresponding amphiphile solution.

We measured the shear modulus G_0 and yield stress τ_y of foams at various gas volume fractions φ and determined the mean Sauter diameter R_{32} simultaneously. Interfacial elasticity was characterized in terms of dilatational as well as shear modulus E_∞ and G_i', respectively.

Our data cover more than two orders of magnitude regarding the absolute values of foam shear modulus, yield stress and interfacial elastic moduli.

In line with previous investigations foam modulus and yield stress strongly vary with interfacial elasticity.

Foams stabilized by nanoparticles and certain protein solutions exhibit a pronounced interfacial shear elasticity, but the range of linear response is narrow, indicating strong attractive interactions or jamming of particles in the surface layer. In these cases, the foam modulus scales as $G_0 = a_s[(\sigma+2G_i)/R_{32}](\varphi(\varphi-\varphi_c))$ with $a_s = 1.6$ and for vanishing elasticity reduces to the well-known model presented in Eq.5.1 confirmed for numerous foams and emulsions stabilized by low molecular weight surfactants.

Dilatational elasticity of foaming solutions could be determined for all investigated systems also including the glycolipid surfactants and block-copolymers.

For this comprehensive data set scaling laws $G_0 = a_d[(\sigma+2E_\infty)/R_{32}](\varphi(\varphi-\varphi_c))$ and $\tau_y = k_d[(\sigma+2E_\infty)/R_{32}](\varphi-\varphi_c)^2$ are confirmed. The numerical pre-factors $a_d = 1$ and $k_d = 0.25$, however, deviate from those reported in the literature for various foam and emulsion systems based on amphiphiles without measurable dilatational elasticity. The term $(\sigma+2E_\infty)/R_{32}$ represents a generalized Laplace pressure and characterizes the change of surface tension with deformation.

Substantial deviations from this simple scaling were, however, observed for systems either stabilized by hydrophobic silica nanoparticles or by β-lactoglobulin aggregated at high ionic strength or at the isoelectric point. In these cases, strong attractive interactions among particles or particulate protein molecules are present and even structure formation across the foam lamellae may occur which strongly contribute to the foam modulus and yield stress but do not show up in E_∞. This hypothesis is further supported by the previously not reported strong dependence of normalized modulus or yield stress on gas volume fraction found for these systems.

The strong correlation between bulk and interfacial elasticity for close packed foams and the empirical scaling laws found to be valid for a broad range of different foam forming amphiphiles may stimulate further theoretical work providing a deeper understanding of these phenomena which are of significant technical relevance.

5.5 Appendix

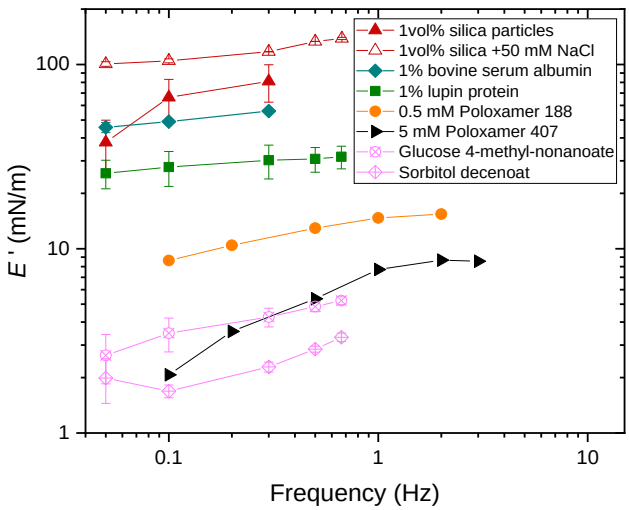

Figure 5A1: Frequency dependence of the interfacial elastic modulus measured in oscillatory dilation at deformation amplitudes in the linear viscoelastic regime.

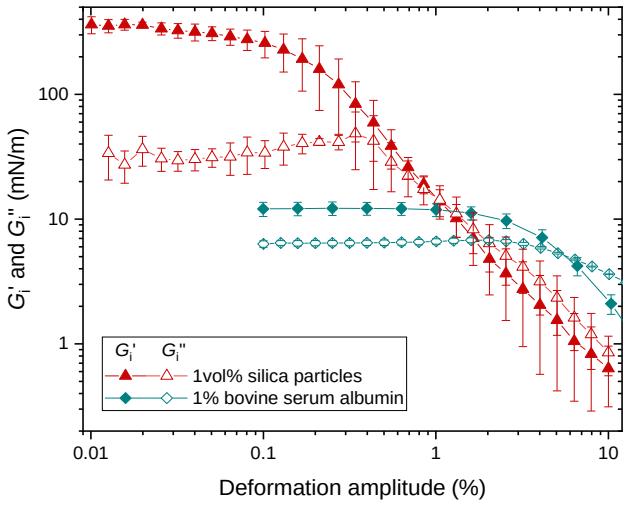

Figure 5.A2: Strain dependence of interfacial storage modulus G_i' and loss modulus G_i'' measured in oscillatory shear at a frequency of 1 Hz.

6 Summary and Outlook

Foams, which are produced from solutions of surface-active substances, are encountered in many ways in everyday life, primarily in foods, but also as cosmetic products, cleaning or fire extinguishing agents. Foams also play an important role in technical processes, e.g. in separation processes such as foam fractionation for the purification of surfactants or proteins and froth flotation to collect metal grains from ores or clean wastewater from organic pollutants. Accordingly, the physicochemical properties of foams as structure, stability and foam rheology have been intensively investigated. Advances in analytical methods, namely *high-throughput bubble size distribution analysis* and *in-situ rheological and structural foam characterization*, are presented in this thesis.

For the above-mentioned technical applications, but also for the application and sensory properties of cosmetics or the consistency and taste of foamed foods, the flow behavior of the corresponding foams plays an important role. The structure and rheology of *lupin protein stabilized foams* are addressed exemplary for food foams. This thesis also provides progress in the understanding of the *correlation between apparent yield stress and shear modulus of foam and interfacial viscoelasticity* of the corresponding solutions.

Furthermore, experimental results indicate that under certain conditions in protein solutions and particle dispersions aggregation and structuring within the foam lamellae play an important role for the flow behavior of the corresponding foams. Considerable gaps still exist with respect to the knowledge and understanding of the structure and aggregate formation in individual foam lamellae and their interfaces.

High-throughput bubble size distribution analysis

The analysis of the size distribution of objects in disperse systems is of particular interest e.g. for prediction of dispersion stability, texture and flow. Endoscopy combined with automated image analysis is well established to access size distributions of emulsions or bubbles produced in stirred vessels, at dispersed volume fraction below 45%. In foams, endoscopy is also appropriate for bubble size distribution analysis, because it allows for in-situ observation of fragile foam structures and overcomes drawbacks of bubble observation through the container wall, e.g. capturing bubbles sheared or distorted at the wall. In food or personal care foams, however, the gas volume fraction is often higher than the maximum packing fraction of spheres (~64 vol%), and spatially varying contrast, light reflections and bubble overlap on the images challenge automated bubble detection, especially when fast transient phenomena need to be monitored. An approach to determine the bubble size distribution inside densely packed foams was developed, combining endoscopic imaging and template matching image analysis. The endoscopic setup is optimized for imaging foams in backlight illumination with no need of filtering or post-processing, if the template matching technique is used for particle detection and subsequent size distribution analysis. This technique has been implemented in a customized software tool and consists of the selection of a template inhering similarity

with the objects on the image, screening of the image for sections with high similarity to the template (calculated using a zero normalized cross correlation (ZNCC)) and subsequent validation of the matches. The distributions of the cumulative volume fraction acquired using template matching agree very well to those obtained manually. Also, more bubbles were detected with a higher accuracy using template matching without preprocessing of the heterogeneously illuminated image than e.g. with Canny edge detection and subsequent Hough transformation. It is also demonstrated that the application of the tool is not restricted to foams. The software tool can compete with time and cost consumptive methods such as manual counting, Coulter counting or laser diffraction and sizes of particles, droplets and bubbles in micro- or endoscopic images can be analyzed with great accuracy. The method does not require dilution and can be used to distinguish between different particle types, and it allows for size detection of anisotropic particles in two dimensions. The template matching approach is especially useful for analysis of endoscopic images with poor and heterogeneous contrast where thresholding, edge detection and Hough transformation fails. The high time resolution of the size distribution analysis using template matching is particularly suitable for capturing fast transient phenomena in situ and was used throughout the investigations of this project.

In-situ rheological and structural foam characterization

The flow properties of food foams determine the processing, lifetime and sensorial perception of the consumer. For development of foam products and quality control characterization of the foam structure and yielding behavior are essential. An experimental setup, which allows for characterization of foam rheology and structure at different heights of a foam column within a commercial whipper is presented. The cylindrical container with excentric whipping coil and heating plate at the bottom is built into a rotational rheometer. Yield stresses are measured with a vane rotor of 1 cm height at intervals of 1 cm along the rotational axis of the container and yield stress profiles were resolved for the first time. Bubble size distributions are analyzed by endoscopic imaging and automated bubble detection as discussed above at same heights with temporal resolution on the order of seconds. Gas volume fractions are obtained from electrical conductivity measurements. Brass rings at the inner container wall and a height adjustable ring submerged into the foam serve as electrodes to detect the conductivity at intervals of 1 cm along the foam axis.

Foams made from UHT milk and reconstituted milk have been investigated for up to 20 min foam age. The gas volume fraction increased linearly with height within the foam column, whereas the mean bubble size and bubble size distribution remained constant. During foam aging, the mean and width of the bubble size distribution increased linearly with time. The yield stress increased with height as well as with ongoing foam drainage as expected from the change in gas volume fraction and scales in accordance to the currently accepted phenomenological model. The gradients in gas volume fraction and yield stress along the column axis increased over time depending on the milk composition. At higher fat content of the milk the gas volume fraction gradient was reduced, and foam lifetime was longer. The developed method offers in-situ characterization of key morphological and rheological parameters of foams and enables fast evaluation of new foam formulations

based on dairy products or plant-based milk substitutes.

Lupin protein stabilized foams

Aqueous solutions of the water-soluble fraction of protein isolate from Lupinus.angustifolius seeds were investigated in terms of foamability and foam stability based on manual shaking tests. Pneumatically produced foams were characterized in terms of gas volume fraction and bubble size distribution, as well as yield stress and elastic modulus. These foam characteristics were discussed in correlation to the interfacial tension and interfacial elastic modulus of corresponding protein solutions. Protein solutions were prepared at different pH and ionic strength, and proteins were also exposed to different heat pretreatment. Precipitated protein aggregates >1 µm were removed prior to foaming, and their effect on foaming characteristics was investigated using samples with defined concentration of such precipitates. With regard to application in vegan milk foam beverages, the effect of carboxymethyl cellulose dissolved as thickening agent and emulsified sunflower seed oil on the foam and interfacial properties was also investigated.

Furthermore, we formulated a milk-like emulsion comprising 3% oil, lupin protein solution prepared at 50°C, containing 20 g/l protein after separation of protein precipitates, and 0.1 vol% carboxymethyl cellulose. Foam was produced from this lupin "plant milk" in a commercial milk whipper. The time evolution of foaming capacity and gas volume fraction for this lupine "plant milk" is very similar to that of ultra-high temperature bovine milk with 3.6% fat and 33 g/l protein. Also, the foam stability did not differ during the observation time of 15 minutes. The yield stress of the lupin "plant-milk" foam was slightly higher than that of the bovine UHT milk foam when the gas volume fraction had reached a quasi-stationary value at 300 s foam age. This is consistent with the lower Sauter radii of the bubbles in the lupine "plant milk" foam. The foam displayed a smooth surface with bubbles smaller than the eye's resolution capacity (< 300 µm) and a stiffness that allowed to form a foam pile. The structure and rheology of foams made from solutions of the soluble fraction of lupin protein isolate turned out to be surprisingly robust against temperature denaturation of the protein, although the protein conformation and size distribution were significantly affected by the denaturation temperature. These preliminary results suggest that lupine proteins are a promising base for the formulation of vegan aerated food products.

We probed the hypothesis that aggregates sufficiently big to hinder drainage by blocking plateau channels can stabilize protein foams significantly. In the presence of aggregated protein precipitates, not only the initial gas volume fraction was decreased, but also its growth rate was lower than in foams produced from the same solution after separation of the precipitates.

Correlation between apparent yield stress and shear modulus of foam and interfacial viscoelasticity

Foams with gas volume fraction exceeding the critical volume fraction, corresponding to the maximum packing fraction of the bubbles, exhibit elastic behavior under small shear

stresses and a critical stress, also termed yield stress, at which bubble rearrangements enable the onset of foam flow. The elastic modulus G_0 and the yield stress τ_y scale with the Laplace pressure inside the bubbles, given by the ratio between surface tension σ and the Sauter bubble radius R_{32}, the foam gas volume fraction φ and the critical volume fraction $\varphi_c \approx 0.635$ for randomly close packed monodisperse spheres. In strained foams and emulsion, droplets and bubbles are stretched, and their interfaces are dilated. Hence, the force needed to strain foam or emulsion is not solely determined by the equilibrium interfacial tension but also by the change of interfacial tension upon change of the interfacial area which is characterized by the interfacial elasticity. In case of small molecular weight surfactants, the interfacial elasticity is negligible small but for other foaming systems considerable interfacial elastic moduli were determined and consequently a significant impact on elasticity and onset of flow of the corresponding foams was measured.

The experimentally observed interfacial tension and the interfacial elasticity in dilation and shear were related to the elastic response of the foams produced with the same foaming agent solution for a broad variety of foaming systems. Foam elastic moduli were normalized to their respective bubble Sauter radii, gas volume fractions and critical gas volume fractions. The normalized shear moduli of the foams show no clear correlation with the equilibrium surface tension. However, the normalized elastic modulus increases clearly with increasing high-frequency dilatational elastic modulus E_∞, and also with increasing shear elastic modulus G_i' of the foaming solutions, albeit to a weaker extend.

From the scaling of the macroscopic elasticity of foams with the sum of the equilibrium interfacial tension and the interfacial shear elasticity, the model $G_0 = a[(\sigma + 2\,G_i')/R_{32}](\varphi(\varphi - \varphi_c))$ was derived that reduces to the widely accepted model if $G_i' = 0$, as it is the case for small molecular weight surfactants. However, it was not applicable to surfactant and block copolymer or lupin protein stabilized foams as these foaming agents did not exhibit measurable interfacial shear elasticities G_i'. Dilatational elasticity E_∞ of foaming solutions could be determined for all investigated systems also including the glycolipid surfactants and block-copolymers. For this comprehensive data set, scaling laws $G_0 = a[(\sigma + 2\,E_\infty)/R_{32}](\varphi(\varphi - \varphi_c))$ and $\tau_y = k[(\sigma + 2\,E_\infty)/R_{32}](\varphi - \varphi_c)^2$ are confirmed.

Substantial deviations from this simple scaling were, however, observed for foams either stabilized by hydrophobic silica nanoparticles or by β-lactoglobulin aggregated at high ionic strength or at the isoelectric point. In these cases, strong attractive interactions among particles or particulate protein molecules are present and even structure formation across the foam lamellae may occur and strongly contribute to the foam modulus and yield stress. These phenomena, however, do not show up in E_∞. This hypothesis is further supported by the strong dependence of normalized modulus or yield stress on gas volume fraction found for these systems.

The central remaining open question is: What is the influence of aggregation and structure formation at the interface and in foam lamellae on the flow behavior of foams? Further

studies are needed to provide information on the arrangement and conformation of the investigated proteins and particles at the interface and the structure of the interfacial layer laterally and perpendicular to the interface. Furthermore, it is unclear how the interfaces interact with each other in the foam films that make up the macroscopic foam.

The Thin Film Pressure Balance method can be used to test the hypothesis of aggregate and structure formation in the lamellae under specific physicochemical conditions (pH, ion concentration and valence) for selected proteins and particles. The thickness of an isolated lamella is determined using interferometric microscopy as a function of applied pressure. From static measurements at equilibrium, the forces that opposing lamella interfaces exert on each other are obtained. The presence of lamella spanning protein or particles aggregates could be evidenced from increased minimum lamella thickness. From kinetic measurements, the lamella stability and information about drainage or indirectly about structural changes in the interface could be determined. The structure formation of protein or particle aggregates across single lamellae could then be correlated to the rheological characteristics of the bulk foam.

X-ray and neutron reflectometry (XRR and NR) allow the determination of the surfactant density profile perpendicular to the interface of a foaming solution with an extremely high resolution on atomic scale. Accordingly, layer thicknesses, roughness and, composition the interfaces can be determined. Grazing incidence small angle x-ray and neutron scattering (GISAXS and GISANS) can be used to investigate lateral structures at interfaces and in thin films from molecular dimensions to mesoscopic length scales in the micrometer range. By changing the angle of incidence of the radiation on the interface of the foaming solutions, the interfacial layers can be analyzed on various depth. In this way, structures at the interface can be distinguished from bulk structures. With the combination of XRR, NR, GISAXS, and GISANS, it should thus be possible to elucidate the entire morphology of complex interfaces in detail. It enables a comprehensive comparison of the interfaces in foams stabilized with different surface-active species, from high and low molecular surfactants to proteins and particles, that have been presented in this thesis. The insights on the individual interfacial morphology could then explain the distinct interfacial viscoelasticity as well as the bulk foam rheology. It would extend the present investigations to a holistic multi-scale approach to a soft matter of high complexity with still hidden secrets, that we call foam.

7 Bibliography

Abidin, M.I.I.Z., Raman, A.A.A., Nor, M.I.M., 2013. Review on measurement techniques for drop size distribution in a stirred vessel. Industrial and Engineering Chemistry Research 52, 16085–16094. https://doi.org/10.1021/ie401548z

Aiking, H., 2011. Future protein supply. Trends in Food Science and Technology 22, 112–120. https://doi.org/10.1016/j.tifs.2010.04.005

AMA Marketing, n.d. Welche der folgenden Kaffeearten bestellen Sie im Kaffeehaus / im Restaurant am liebsten? [WWW Document]. In Statista - Das Statistik-Portal.

Bals, A., Kulozik, U., 2003a. The influence of the pore size, the foaming temperature and the viscosity of the continuous phase on the properties of foams produced by membrane foaming. Journal of Membrane Science. https://doi.org/10.1016/S0376-7388(03)00168-6

Bals, A., Kulozik, U., 2003b. Effect of pre-heating on the foaming properties of whey protein isolate using a membrane foaming apparatus. International Dairy Journal. https://doi.org/10.1016/S0958-6946(03)00111-0

Batchelor, G.K., 1970. The stress system in a suspension of force-free particles. Journal of Fluid Mechanics 41, 545–570. https://doi.org/10.1017/S0022112070000745

Bhamla, M.S., Giacomin, C.E., Balemans, C., Fuller, G.G., 2014. Influence of interfacial rheology on drainage from curved surfaces. Soft Matter 10, 6917–6925. https://doi.org/10.1039/c3sm52934g

Binks, B.P., Murakami, R., 2006. Phase inversion of particle-stabilized materials from foams to dry water. Nature materials 5, 865–869. https://doi.org/10.1038/nmat1757

Blunk, D., 2018. Fire Fighting Foams, in: Foam Films and Foams. CRC Press, pp. 433–444.

Böhme, A., Dietze, M., Geform, A., Priebke, A., Schachler, B., Struck, C., Wehling, P., 2016. Lupinen - Anbau und Verwertung. Gesellschaft zur Förderung der Lupine (G.F.L.).

Bothe, M., Christlieb, M.A., Hoffmann, M., Tedjasukmana, O., Michaux, F., Rollbusch, P., Becker, M., Schlüter, M., 2017. Bubble size and bubble velocity distribution in bubble columns under industrial conditions. Canadian Journal of Chemical Engineering 95, 902–912. https://doi.org/10.1002/cjce.22759

Campbell, G.M., Mougeot, E., 1999. Creation and characterisation of aerated food products. Trends in Food Science & Technology 10, 283–296. https://doi.org/10.1016/S0924-2244(00)00008-X

Cantat, I., Cohen-Addad, S., Elias, F., Graner, F., Höhler, R., Pitois, O., Rouyer, F., Saint-Jalmes, A., 2013. Foams : Structure and Dynamics. OUP Oxford, New York.

Cao, F., Lisani, J.-L., Morel, J.-M., Musé, P., Sur, F., 2008. A theory of shape identification. Springer Science & Business Media.

Carl, A., Bannuscher, A., Von Klitzing, R., 2015. Particle stabilized aqueous foams at different length scales: Synergy between silica particles and alkylamines. Langmuir 31, 1615–1622. https://doi.org/10.1021/la503321m

Carrier, V., Colin, A., 2003. Coalescence in draining foams. Langmuir 19, 4535–4538. https://doi.org/10.1021/la026995b

Chang, C.H., Franses, E.I., 1995. Adsorption dynamics of surfactants at the air/water interface: a critical review of mathematical models, data, and mechanisms. Colloids and Surfaces A: Physicochemical and Engineering Aspects 100, 1–45. https://doi.org/10.1016/0927-7757(94)03061-4

Cohen-Addad, S., Höhler, R., 2014. Rheology of foams and highly concentrated emulsions. Current Opinion in Colloid & Interface Science 19, 536–548. https://doi.org/10.1016/0021-9797(89)90396-2

Cohen-Addad, S., Höhler, R., Pitois, O., 2013. Flow in Foams and Flowing Foams. Annual Review of Fluid Mechanics 45, 241–267. https://doi.org/10.1146/annurev-fluid-011212-140634

Cornwell, P.A., 2018. A review of shampoo surfactant technology: consumer benefits, raw materials and recent developments. International Journal of Cosmetic Science 40, 16–30. https://doi.org/10.1111/ics.12439

Costa, S., Höhler, R., Cohen-Addad, S., 2013. The coupling between foam viscoelasticity and interfacial rheology. Soft Matter 9, 1100. https://doi.org/10.1039/c2sm26644j

Cox, S.J., Whittick, E.L., 2006. Shear modulus of two-dimensional foams: The effect of area dispersity and disorder. European Physical Journal E. https://doi.org/10.1140/epje/i2006-10044-x

Cullen, P.J., O'Donnell, C.P., Houška, M., 2003. Rotational rheometry using complex geometries - A review. Journal of Texture Studies 34, 1–20. https://doi.org/10.1111/j.1745-4603.2003.tb01052.x

Davis, J.P., Foegeding, E.A., Hansen, F.K., 2004. Electrostatic effects on the yield stress of whey protein isolate foams. Colloids and Surfaces B: Biointerfaces 34, 13–23. https://doi.org/10.1016/j.colsurfb.2003.10.014

de Gennes, P.-G., Brochard-Wyart, F., Quéré, D., 2013. Capillarity and wetting phenomena: drops, bubbles, pearls, waves. Springer Science \& Business Media.

Deminiere, B., Colin, A., Leal-Calderon, F., Muzy, J.F., Bibette, J., 1999. Cell growth in a 3d cellular system undergoing coalescence. Physical Review Letters 82, 229–232. https://doi.org/10.1103/PhysRevLett.82.229

Denkov, N.D., Subramanian, V., Gurovich, D., Lips, A., 2005. Wall slip and viscous dissipation in sheared foams: Effect of surface mobility. Colloids and Surfaces A: Physicochemical and Engineering Aspects 263, 129–145. https://doi.org/10.1016/j.colsurfa.2005.02.038

Denkov, N.D., Tcholakova, S., Golemanov, K., Ananthapadmanabhan, K.P., Lips, A., 2008. Viscous friction in foams and concentrated emulsions under steady shear. Physical Review Letters 100, 1–4. https://doi.org/10.1103/PhysRevLett.100.138301

Denkov, N.D., Tcholakova, S., Golemanov, K., Ananthpadmanabhan, K.P., Lips, A., 2009. The role of surfactant type and bubble surface mobility in foam rheology. Soft Matter 5, 3389–3408. https://doi.org/10.1039/b903586a

Diamond, A., 2011. WNCC - Weighted Normalized Cross Correlation [WWW Document]. URL www.mathworks.com/matlabcentral/fileexchange/33340-wncc-weighted-normalized-cross-correlation (accessed 4.28.20).

Dimitrova, T.D., Leal-Calderon, F., 2004. Rheological properties of highly concentrated protein-stabilized emulsions. Advances in Colloid and Interface Science 108–109, 49–61. https://doi.org/10.1016/j.cis.2003.10.002

Dollet, B., Raufaste, C., 2014. Rheology of aqueous foams. Comptes Rendus Physique 15, 731–747. https://doi.org/10.1016/j.crhy.2014.09.008

Dombrowski, J., Johler, F., Warncke, M., Kulozik, U., 2016. Correlation between bulk characteristics of aggregated β-lactoglobulin and its surface and foaming properties. Food Hydrocolloids. https://doi.org/10.1016/j.foodhyd.2016.05.027

Drenckhan, W., Hutzler, S., 2015. Structure and energy of liquid foams. Advances in colloid and interface science 224, 1–16. https://doi.org/10.1016/j.cis.2015.05.004

Drenckhan, W., Saint-Jalmes, A., 2015. The science of foaming. Advances in Colloid and Interface Science 222, 228–259. https://doi.org/10.1016/j.cis.2015.04.001

Durand, M., Langevin, D., 2002. Physicochemical approach to the theory of foam drainage. The European Physical Journal E 7, 35–44. https://doi.org/10.1140/epje/i200101092

Durian, D.J., Weitz, D.A., Pine, D.J., 1991. Scaling behavior in shaving cream. Physical Review A 44, 7902–7906.

Engelhardt, K., Lexis, M., Gochev, G., Konnerth, C., Miller, R., Willenbacher, N., Peukert, W., Braunschweig, B., 2013. pH E ff ects on the Molecular Structure of β - Lactoglobulin Modi fi ed Air − Water Interfaces and Its Impact on Foam Rheology.

Ewoldt, R.H., Johnston, M.T., Caretta, L.M., 2015. Experimental Challenges of Shear Rheology: How to Avoid Bad Data, Spagnolie S. (eds) Complex Fluids in Biological Systems. Springer, New York.

Exerowa, D., Kolarov, T., Khristov, K., 1987. Direct measurement of disjoining pressure in black foam films. I. Films from an ionic surfactant. Colloids and Surfaces 22, 161–169. https://doi.org/10.1016/0166-6622(87)80218-4

Exerowa, D., Scheludko, A., 1971. Porous plate method for studying microscopic foam and emulsion films. CR Acad Bulg Sci 24, 47–50.

Fameau, A.L., Salonen, A., 2014. Effect of particles and aggregated structures on the foam stability and aging. Comptes Rendus Physique 15, 748–760. https://doi.org/10.1016/j.crhy.2014.09.009

FAO, 2020. FAOSTAT statistical database [WWW Document]. FAOSTAT. URL http://www.fao.org/faostat/en/#data/QC/ (accessed 8.4.20).

Farr, R.S., Groot, R.D., 2009. Close packing density of polydisperse hard spheres. Journal of Chemical Physics 131. https://doi.org/10.1063/1.3276799

Feitosa, K., Marze, S., Saint-Jalmes, A., Durian, D.J., 2005a. Electrical conductivity of dispersions: From dry foams to dilute suspensions. Journal of Physics Condensed Matter 17, 6301–6305. https://doi.org/10.1088/0953-8984/17/41/001

Feitosa, K., Marze, S., Saint-Jalmes, A., Durian, D.J.J., 2005b. Electrical conductivity of dispersions: from dry foams to dilute suspensions. J. Phys. Condens. Matter 17, 6301. https://doi.org/10.1088/0953-8984/17/41/001

Friedman, M., Brandon, D.L., 2001. Nutritional and health benefits of soy proteins. Journal of Agricultural and Food Chemistry 49, 1069–1086. https://doi.org/10.1021/jf0009246

Frostad, J.M., Tammaro, D., Santollani, L., Bochner de Araujo, S., Fuller, G.G., 2016. Soft Matter Dynamic fluid-film interferometry as a predictor of bulk foam properties †. Soft Matter 12, 9266. https://doi.org/10.1039/c6sm01361a

Fuller, G.G., Vermant, J., 2012. Complex fluid-fluid interfaces: rheology and structure. Annual review of chemical and biomolecular engineering 3, 519–43. https://doi.org/10.1146/annurev-chembioeng-061010-114202

Golemanov, K., Denkov, N.D., Tcholakova, N.D., Vethamuthu, M., Lips, a., 2008. Surfactant mixtures for control of bubble surface mobility in foam studies. Langmuir 24, 9956–9961. https://doi.org/10.1021/la8015386

Goormaghtigh, E., Cabiaux, V., Ruysschaert, J.-M., 1994. Determination of Soluble and Membrane Protein Structure by Fourier Transform Infrared Spectroscopy, in: Hilderson, H.J., Ralston, G.B. (Eds.), Physicochemical Methods in the Study of Biomembranes. Springer US, Boston, MA, pp. 405–450. https://doi.org/10.1007/978-1-4615-1863-1_10

Gopal, A.D., Durian, D.J., 2003. Relaxing in foam. Physical Review Letters 91, 1–4. https://doi.org/10.1103/PhysRevLett.91.188303

Gorissen, S.H.M., Crombag, J.J.R., Senden, J.M.G., Waterval, W.A.H., Bierau, J., Verdijk, L.B., van Loon, L.J.C., 2018. Protein content and amino acid composition of commercially available plant-based protein isolates. Amino Acids 50, 1685–1695. https://doi.org/10.1007/s00726-018-2640-5

Gunes D. Z., Engmann J., Gehin-Delval C., Schmitt C., L.M.E., 2018. Foams in Food, in: Foam Films and Foams: Fundamentals and Applications. CRC Press, Boca Raton, pp. 379–400. https://doi.org/https://doi.org/10.1201/9781351117746

Gurkov, T.D., Petkov, J.T., Campbell, B., Borwankar, R.P., 2007. Dilatational and shear rheology of protein layers at the water-air interface, in: Food Colloids. https://doi.org/10.1039/9781847550842-00181

Hartmann, C., Siegrist, M., 2017. Consumer perception and behaviour regarding sustainable protein consumption: A systematic review. Trends in Food Science and Technology 61, 11–25. https://doi.org/10.1016/j.tifs.2016.12.006

Hofmann, a., Schembecker, G., Merz, J., 2015. Role of bubble size for the performance of continuous foam fractionation in stripping mode. Colloids and Surfaces A: Physicochemical and Engineering Aspects 473, 85–94. https://doi.org/10.1016/j.colsurfa.2014.12.042

Hollenbach, R., Völp, A.R., Höfert, L., Rudat, J., Ochsenreither, K., Willenbacher, N., Syldatk, C., 2020. Interfacial and Foaming Properties of Tailor-Made Glycolipids—Influence of the Hydrophilic Head Group and Functional Groups in the Hydrophobic Tail. Molecules 25, 3797. https://doi.org/10.3390/molecules25173797

ICO, n.d. Konsum von Kaffee in ausgewählten Ländern weltweit in den Jahren 2012/13 bis 2016/17 (in 1.000 Säcken à 60 Kilogramm). [WWW Document]. In Statista - Das Statistik-Portal.

Jamialahmadi, M., Zehtaban, M.R., Müller-Steinhagen, H., Sarrafi, A., Smith, J.M., 2001. Study of Bubble Formation Under Constant Flow Conditions. Chemical Engineering Research and Design 79, 523–532. https://doi.org/10.1205/02638760152424299

Jayasena, V., Chih, H.J., Science, F., 2010. Functional Properties of Sweet Lupin Protein Isolated and Tested at Various pH Levels. Research Journal of Agriculture and Biological Sciences 6, 130–137.

Jimenez-Junca, C., Sher, A., Gumy, J.C., Niranjan, K., 2015. Production of milk foams by steam injection: The effects of steam pressure and nozzle design. Journal of Food Engineering 166, 247–254. https://doi.org/10.1016/j.jfoodeng.2015.05.035

Jimenez-Junca, C.A., Gumy, J.C., Sher, A., Niranjan, K., 2011. Rheology of Milk Foams Produced by Steam Injection. Journal of Food Science 76, 569–575. https://doi.org/10.1111/j.1750-3841.2011.02387.x

Jurine, S., Cox, S., Graner, F., 2005. Dry three-dimensional bubbles: Growth-rate, scaling state and correlations. Colloids and Surfaces A: Physicochemical and Engineering Aspects 263, 18–26. https://doi.org/10.1016/j.colsurfa.2005.01.015

Khan, S.A., Schnepper, C.A., Armstrong, R.C., 1988. Foam Rheology: III. Measurement of Shear Flow Properties. Journal of Rheology 32, 69–92. https://doi.org/10.1122/1.549964

Khristov, K., Exerowa, D., Minkov, G., 2002. Critical capillary pressure for destruction of single foam films and foam: Effect of foam film size. Colloids and Surfaces A: Physicochemical and Engineering Aspects 210, 159–166. https://doi.org/10.1016/S0927-7757(02)00377-1

Kinsella, J.E., 1981. Functional properties of proteins: Possible relationships between structure and function in foams. Food Chemistry. https://doi.org/10.1016/0308-8146(81)90033-9

Kloek, W., van Vliet, T., Meinders, M., 2001. Effect of bulk and interfacial rheological properties on bubble dissolution. Journal of Colloid and Interface Science 237, 158–166. https://doi.org/10.1006/jcis.2001.7454

Koczo, K., Lobo, L.A., Wasan, D.T., 1992. Effect of oil on foam stability: Aqueous foams stabilized by emulsions. Journal of Colloid And Interface Science 150, 492–506. https://doi.org/10.1016/0021-9797(92)90218-B

Koehler, S.A., Hilgenfeldt, S., Stone, H.A., 2000. Generalized view of foam drainage: Experiment and theory. Langmuir 16, 6327–6341. https://doi.org/10.1021/la9913147

Krägel, J., Derkatch, S.R., Miller, R., 2008. Interfacial shear rheology of protein-surfactant layers. Advances in Colloid and Interface Science 144, 38–53. https://doi.org/10.1016/j.cis.2008.08.010

Kraynik, A.M., 2006. The structure of random foam. Advanced Engineering Materials 8, 900–906. https://doi.org/10.1002/adem.200600167

Kraynik, A.M., Reinelt, D.A., Van Swol, F., 2004. Structure of random foam. Physical Review Letters 93, 1–4. https://doi.org/10.1103/PhysRevLett.93.208301

Kruyt, N.P., 2007. On the shear modulus of two-dimensional liquid foams: A theoretical study of the effect of geometrical disorder. Journal of Applied Mechanics, Transactions ASME. https://doi.org/10.1115/1.2424241

Lacasse, M.D., Grest, G.S., Levine, D., Mason, T.G., Weitz, D.A., 1996. Model for the elasticity of compressed emulsions. Physical Review Letters 76, 3448–3451. https://doi.org/10.1103/PhysRevLett.76.3448

Lambert, J., Mokso, R., Cantat, I., Cloetens, P., Glazier, J.A., Graner, F., Delannay, R., 2010. Coarsening foams robustly reach a self-similar trowth regime. Physical Review Letters 104, 1–4. https://doi.org/10.1103/PhysRevLett.104.248304

Lazidis, A., Parizotto, L.D.A., Spyropoulos, F., Norton, I.T., 2017. Microstructural design of aerated food systems by soft-solid materials Food Hydrocolloids Reprint of:

Microstructural design of aerated food systems by soft-solid materials. Food hydrocolloids 78, 26–35. https://doi.org/10.1016/j.foodhyd.2017.07.030

Lech, F.J., Delahaije, R.J.B.M., Meinders, M.B.J., Gruppen, H., Wierenga, P.A., 2016. Identification of critical concentrations determining foam ability and stability of β-lactoglobulin. Food Hydrocolloids. https://doi.org/10.1016/j.foodhyd.2016.01.005

Lewis, J.P. (Industrial L.& M., 1995. Fast Normalized Cross-Correlation Template Matching by Cross-. Vision Interface 1995, 1–7. https://doi.org/10.1007/s00034-009-9130-7

Lexis, M., Willenbacher, N., 2018. Foam Rheology, in: Foam Films and Foams: Fundamentals and Applications. CRC Press.

Lexis, M., Willenbacher, N., 2014a. Yield stress and elasticity of aqueous foams from protein and surfactant solutions - The role of continuous phase viscosity and interfacial properties. Colloids and Surfaces A: Physicochemical and Engineering Aspects 459, 177–185. https://doi.org/10.1016/j.colsurfa.2014.06.030

Lexis, M., Willenbacher, N., 2014b. Relating foam and interfacial rheological properties of β-lactoglobulin solutions. Soft Matter 10, 9626–9636. https://doi.org/10.1039/c4sm01972e

Lin, G., Frostad, J.M., Fuller, G.G., 2018. Influence of interfacial elasticity on liquid entrainment in thin foam films. Physical Review Fluids 3, 114001. https://doi.org/10.1103/PhysRevFluids.3.114001

Lucas, M.M., Stoddard, F.L., Annicchiarico, P., Frías, J., Martínez-Villaluenga, C., Sussmann, D., Duranti, M., Seger, A., Zander, P.M., Pueyo, J.J., 2015. The future of lupin as a protein crop in Europe. Frontiers in Plant Science 6, 1–6. https://doi.org/10.3389/fpls.2015.00705

Lykema, J., Fleer, G. J., Kleijn, J. M., Leermakers, F. A. M., Norde, W., & Van Vliet, T., 2000. Fundamentals of Interface and Colloid Science, Liquid–Fluid Interfaces. Academic Press.

Martinie, L., Buggisch, H., Willenbacher, N., 2013. Apparent elongational yield stress of soft matter. Journal of Rheology 57, 627–646. https://doi.org/10.1122/1.4789785

Marze, S., Guillermic, R.M., Saint-Jalmes, A., 2009. Oscillatory rheology of aqueous foams: Surfactant, liquid fraction, experimental protocol and aging effects. Soft Matter 5, 1937–1946. https://doi.org/10.1039/b817543h

Marze, S.P.L., Saint-Jalmes, A., Langevin, D., 2005. Protein and surfactant foams: Linear rheology and dilatancy effect, in: Colloids and Surfaces A: Physicochemical and Engineering Aspects. pp. 121–128. https://doi.org/10.1016/j.colsurfa.2005.01.014

Mason, T.G., Bibette, J., Weitz, D. a., 1996. Yielding and Flow of Monodisperse Emulsions. Journal of colloid and interface science 179, 439–448. https://doi.org/10.1006/jcis.1996.0235

Mason, T.G., Bibette, J., Weitz, D.A., 1995. Elasticity of Compressed Emulsions. Physical Review Letters 75, 2051–2054.

Matzke, E.B., 1946. The three-dimensional shape of bubbles in foam; an analysis of the role of surface forces in three-dimensional cell shape determination. American journal of botany. https://doi.org/10.2307/2437492

Merkus, H.G., 2009. Particle Size Measurements: Fundamentals, Practice, Quality, Particle Technology Series. Springer Netherlands.

Miller, R., Ferri, J.K., Javadi, A., Krägel, J., Mucic, N., Wüstneck, R., 2010. Rheology of interfacial layers 937–950. https://doi.org/10.1007/s00396-010-2227-5

Monteiro, M.R.P., Alves, F.D., Silva, M.R., 2020. Evaluation of technological properties of lupine flour (Lupinus albus and Lupinus angustifolius). Scientific Electronic Archives 13, 46. https://doi.org/10.36560/1352020882

Murray, B.S., Ettelaie, R., 2004. Foam stability: proteins and nanoparticles. Current Opinion in Colloid & Interface Science 9, 314–320. https://doi.org/10.1016/j.cocis.2004.09.004

Mysels, K., Malcolm, J.N., 1966. Direct Measurement of the Variation of Repulsion with Distance. Discuss. Faraday Soc. 42, 42–50.

Neacsu, M., McBey, D., Johnstone, A.M., 2017. Meat Reduction and Plant-Based Food: Replacement of Meat: Nutritional, Health, and Social Aspects, in: Sustainable Protein Sources. https://doi.org/10.1016/B978-0-12-802778-3.00022-6

Pagureva, N., Tcholakova, S., Golemanov, K., Denkov, N., Pelan, E., Stoyanov, S.D., 2016. Surface properties of adsorption layers formed from triterpenoid and steroid saponins. Colloids and Surfaces A: Physicochemical and Engineering Aspects 491, 18–28. https://doi.org/10.1016/j.colsurfa.2015.12.001

Palencia, C., Lauwaet, K., de La Cueva, L., Acebrón, M., Conde, J.J., Meyns, M., Klinke, C., Gallego, J.M., Otero, R., Juárez, B.H., 2014. Cl-capped CdSe nanocrystals via in situ generation of chloride anions. Nanoscale 6, 6812–6818. https://doi.org/10.1039/c4nr00431k

Panckow, R., Maaß, S., Emmerich, J., Kraume, M., 2013. Automatisierte Quantifizierung von Blasengrößenverteilungen in einem gerührten Luft/Wasser-System. Chemie-Ingenieur-Technik 85, 1036–1045. https://doi.org/10.1002/cite.201200228

Panckow, R.P., Reinecke, L., Cuellar, M.C., Maa, S., 2017. Photo-Optical In-Situ Measurement of Drop Size Distributions: Applications in Research and Industry. Oil and Gas Science and Technology 72. https://doi.org/10.2516/ogst/2017009

Pandolfini, P., Makievski, A.V., Ravera, F., Loglio, G., Liggieri, L., 2011. Determination Of Interfacial Properties By The Pendant Drop Tensiometry: Optimisation Of Experimental And Calculation Procedures, in: Bubble and Drop Interfaces. https://doi.org/10.1163/ej.9789004174955.i-558.12

Petkov, J.T., Gurkov, T.D., Campbell, B.E., Borwankar, R.P., 2000. Dilatational and shear elasticity of gel-like protein layers on air/water interface. Langmuir 16, 3703–3711. https://doi.org/10.1021/la991287k

Pratt, K.W., Koch, W.F., Wu, Y.C., Berezansky, P.A., 2001. Molality-based primary standards of electrolytic conductivity (IUPAC Technical report). Pure and Applied Chemistry 73, 1783–1793. https://doi.org/10.1351/pac200173111783

Princen, H.M., 1985. Rheology of foams and highly concentrated emulsions. II. experimental study of the yield stress and wall effects for concentrated oil-in-water emulsions. Journal of Colloid And Interface Science 105, 150–171. https://doi.org/10.1016/0021-9797(85)90358-3

Princen, H.M., 1982. Rheology of foams and highly concentrated emulsions: I. Elastic properties and yield stress of a cylindrical model system. Journal of Colloid and interface science 91, 160–175.

Princen, H.M., 1979. Highly concentrated emulsions. I. Cylindrical systems. Journal of Colloid and Interface Science. Journal of Colloid and Interface Science 71, 55–66.

Princen, H.M., Kiss, A.D., 1989. Rheology of foams and highly concentrated emulsions. IV. An experimental study of the shear viscosity and yield stress of concentrated emulsions. Journal of Colloid And Interface Science 128, 176–187. https://doi.org/10.1016/0021-9797(89)90396-2

Princen, H.M., Kiss, A.D., 1987. Osmotic Pressure of Foams and Highly Concentrated Emulsions. 2. Determination from the Variation in Volume Fraction with Height in an Equilibrated Column. Langmuir 3, 36–41. https://doi.org/10.1021/la00073a007

Princen, H.M., Kiss, A.D., 1986. Rheology of foams and highly concentrated emulsions: III. Static shear modulus. ournal of Colloid and Interface Science 112, 427–437.

Rami-shojaei, S., Vachier, C., Schmitt, C., 2009. Automatic analysis of 2D foam sequences: Application to the characterization of aqueous proteins foams stability. Image and Vision Computing 27, 609–622. https://doi.org/10.1016/j.imavis.2008.10.004

Raymundo, A., Empis, J., Sousa, I., 1998. White lupin protein isolate as a foaming agent. European Food Research and Technology 207, 91–96. https://doi.org/10.1007/s002170050300

Razi, S.M., Motamedzadegan, A., Shahidi, S.A., Rashidinejad, A., 2019. Physical and Rheological Properties of Egg Albumin Foams Are Affected by Ionic Strength and Basil Seed Gum Supplementation. International Journal of Chemical Engineering 2019. https://doi.org/10.1155/2019/2502908

Rio, E., Biance, A.-L., 2014. Thermodynamic and Mechanical Timescales Involved in Foam Film Rupture and Liquid Foam Coalescence. ChemPhysChem 15, 3692–3707. https://doi.org/10.1002/cphc.201402195

Rodríguez-Ambriz, S.L., Martínez-Ayala, A.L., Millán, F., Dávila-Ortíz, G., 2005. Composition and functional properties of Lupinus campestris protein isolates. Plant Foods for Human Nutrition 60, 99–107. https://doi.org/10.1007/s11130-005-6835-z

Rouimi, S., Schorsch, C., Valentini, C., Vaslin, S., 2005. Foam stability and interfacial properties of milk protein-surfactant systems. Food Hydrocolloids 19, 467–478. https://doi.org/10.1016/j.foodhyd.2004.10.032

Saint-Jalmes, A., Durian, D.J., 1999. Vanishing elasticity for wet foams: Equivalence with emulsions and role of polydispersity. Journal of Rheology 43, 1411–1422. https://doi.org/10.1122/1.551052

Saint-Jalmes, A., Langevin, D., 2002. Time evolution of aqueous foams: Drainage and coarsening. Journal of Physics Condensed Matter 14, 9397–9412. https://doi.org/10.1088/0953-8984/14/40/325

Saint-Jalmes, A., Zhang, Y., Langevin, D., 2004. Quantitative description of foam drainage: Transitions with surface mobility. European Physical Journal E 15, 53–60. https://doi.org/10.1140/epje/i2004-10036-x

Samaniuk, J.R., Vermant, J., 2014. Micro and macrorheology at fluid-fluid interfaces. Soft matter 10, 7023–33. https://doi.org/10.1039/c4sm00646a

Sathe, S.K., Deshpande, S.S., Salunkhe, D.K., 1982. Functional Properties of Lupin Seed (Lupinus mutabilis) Proteins and Protein Concentrates. Journal of Food Science 47, 491–497. https://doi.org/10.1111/j.1365-2621.1982.tb10110.x

Sauret, A., Boulogne, F., Cappello, J., Dressaire, E., Stone, H.A., 2015. Damping of liquid sloshing by foams. Physics of Fluids 27, 022103. https://doi.org/10.1063/1.4907048

Sedev, R., Connor, J.N., 2018. The Froth in Froth Flotation, in: Foam Films and Foams: Fundamentals and Applications. CRC Press.

Stabile, M.C.C., Guimarães, A.L., Silva, D.S., Ribeiro, V., Macedo, M.N., Coe, M.T., Pinto, E., Moutinho, P., Alencar, A., 2020. Solving Brazil's land use puzzle: Increasing production and slowing Amazon deforestation. Land Use Policy 91, 104362. https://doi.org/10.1016/J.LANDUSEPOL.2019.104362

Stamenović, D., 1991. A model of foam elasticity based upon the laws of plateau. Journal of Colloid And Interface Science. https://doi.org/10.1016/0021-9797(91)90116-P

Statista, n.d. Was für Kaffee trinken Sie normalerweise auswärts, also z.B. im Café, im Restaurant oder unterwegs? [WWW Document]. In Statista - Das Statistik-Portal.

Sujak, A., Kotlarz, A., Strobel, W., 2006. Compositional and nutritional evaluation of several lupin seeds. Food Chemistry 98, 711–719. https://doi.org/10.1016/j.foodchem.2005.06.036

Tcholakova, S., Denkov, N.D., Golemanov, K., Ananthapadmanabhan, K.P., Lips, A., 2008. Theoretical model of viscous friction inside steadily sheared foams and concentrated emulsions. Physical Review E - Statistical, Nonlinear, and Soft Matter Physics 78, 1–18. https://doi.org/10.1103/PhysRevE.78.011405

Tsibranska, S., Tcholakova, S., Golemanov, K., Denkov, N., Arnaudov, L., Pelan, E., Stoyanov, S.D., 2020a. Origin of the extremely high elasticity of bulk emulsions, stabilized by Yucca Schidigera saponins. arXiv 1–26.

Tsibranska, S., Tcholakova, S., Golemanov, K., Denkov, N., Pelan, E., Stoyanov, S.D., 2020b. c. Journal of Colloid and Interface Science 564, 264–275. https://doi.org/10.1016/j.jcis.2019.12.108

van der Net, A., Blondel, L., Saugey, A., Drenckhan, W., 2007. Simulating and interpretating images of foams with computational ray-tracing techniques. Colloids and Surfaces A: Physicochemical and Engineering Aspects 309, 159–176. https://doi.org/10.1016/j.colsurfa.2006.11.057

Vandebril, S., Franck, A., Fuller, G.G., Moldenaers, P., Vermant, J., 2010. A double wall-ring geometry for interfacial shear rheometry. Rheologica Acta 49, 131–144. https://doi.org/10.1007/s00397-009-0407-3

Vera, M.U., Durian, D.J., 2002. Enhanced Drainage and Coarsening in Aqueous Foams. Physical Review Letters 88, 4. https://doi.org/10.1103/PhysRevLett.88.088304

Verbist, G.D., Weaire, D., Kraynik, A.M., 1996. The foam drainage equation. Journal of Physics Condensed Matter 8, 3715–3731. https://doi.org/10.1088/0953-8984/8/21/002

Vogelsang-O'Dwyer, M., Bez, J., Petersen, I.L., Joehnke, M.S., Detzel, A., Busch, M., Krueger, M., Ispiryan, L., O'Mahony, J.A.;, Arendt, E.K.;, Zannini, Emanuele., 2020. Techno-Functional, Nutritional and Environmental Performance of Protein Isolates from Blue Lupin and White Lupin. Foods 9, 230.

Völp, A.R., Fessler, F., Reiner, J., Willenbacher, N., 2020a. High-Throughput Object Recognition and Sizing in Disperse Systems. Chemical Engineering and Technology 43, 1897–1902. https://doi.org/10.1002/ceat.201900494

Völp, A.R., Kagerbauer, L., Engmann, J., Gunes, D.Z., Gehin-Delval, C., Willenbacher, N., 2020b. In-situ rheological and structural characterization of milk foams in a commercial foaming device. Journal of Food Engineering 290, 110150. https://doi.org/10.1016/j.jfoodeng.2020.110150

Völp, A.R., Seitz, J., Willenbacher, N., n.d. Structure and rheology of foams stabilized by lupin protein isolate of Lupinus.angustifolius. Food Hydrocolloids.

Wäsche, A., Müller, K., Knauf, U., 2001. New processing of lupin protein isolates and functional properties. Nahrung - Food 45, 393–395. https://doi.org/10.1002/1521-3803(20011001)45:6<393::AID-FOOD393>3.0.CO;2-O

Weaire, D., Hutzler, S., Cox, S., Kern, N., Alonso, M.D., Drenckhan, W., 2003. The fluid dynamics of foams. Journal of Physics Condensed Matter 15. https://doi.org/10.1088/0953-8984/15/1/307

Weaire, D.L., Hutzler, Stefan., 1999. The physics of foams, Foam collapse.

Willenbacher, N., Lexis, M., 2018. Rheology of Foams, in: Foam Films and Foams: Fundamentals and Applications. CRC Press, Boca Raton. https://doi.org/https://doi.org/10.1201/9781351117746

Wong, A., Pitts, K., Jayasena, V., Johnson, S., 2013. Isolation and foaming functionality of acid-soluble protein from lupin (Lupinus angustifolius) kernels. Journal of the Science of Food and Agriculture 93, 3755–3762. https://doi.org/10.1002/jsfa.6249

World Health Organization, 2018. A healthy diet sustainably produced. International Archives of Medicine 7, 21. https://doi.org/10.1186/1755-7682-7-34

Worldpanel, K., n.d. UK's favorite coffee drinks, Sales, year ending 25 February 2018 [WWW Document]. bbc NEWS.

Xia, J., Fu, X., Zhang, X., Hu, Y., Wang, R., 2013. Design and application of endoscope with aided lens for observation of fire-fighting foam. Applied Mechanics and Materials 271, 823–828. https://doi.org/10.4028/www.scientific.net/AMM.271-272.823

Zabulis, X., Papara, M., Chatziargyriou, A., Karapantsios, T.D., 2007. Detection of densely dispersed spherical bubbles in digital images based on a template matching technique. Application to wet foams. Colloids and Surfaces A: Physicochemical and Engineering Aspects 309, 96–106. https://doi.org/10.1016/j.colsurfa.2007.01.007

Zhang, H., 2007. Electrical properties of foods, in: Barbosa-Cánovas, G. v. (Ed.), EOLSS: New York, USA. pp. 110–119.

Notations

Latin Symbols

A	m^2	interfacial area
a		numerical constant
A_{eq}	m^2	equilibrium interfacial area
A_N	$m^2\ s^{-1}$	growth of the bubble area
Bo		Bond number
Bq		Boussinesq number
C		geometrical constant, fitting parameter
c	$mol\ m^{-3}$	bulk concentration
c_0	$mol\ m^{-3}$	initial bulk concentration
$c_{sublayer}$		surfactant concentration at the boundary between the diffusion and adsorption dominated domains
Ca		capillary number
Ca_{crit}		critical capillary number
Ca_l		liquid capillary number
D	$m^2\ s^{-1}$	diffusion coefficient
D_{eff}	$m^2\ s^{-1}$	effective diffusion coefficient
d	m	bubble diameter, droplet size
d_{10}	m	10^{th} percentile of diameter
d_{50}	m	median diameter
d_{90}	m	90^{th} percentile of diameter
d_{32}	m	Sauter diameter
E	$J\ m^{-2}$	interfacial energy, energy
$\hat{E}$		scaled energy

E_A	N m^{-1}	interfacial dilatational elasticity
E^*	N m^{-1}	complex interfacial dilatational module
E'	N m^{-1}	interfacial dilatational storage module
E''	N m^{-1}	interfacial dilatational loss module
E_∞	N m^{-1}	interfacial elasticity in the high frequency limit
F	N	force
F_b	N	buoyancy force
F_g	N	gravitational force
F_V	N	Stokes force
F_σ	N	surface tension force
f	s^{-1}	frequency
G	Pa	shear modulus
G_0	Pa	plateau modulus
G^*	Pa	complex shear modulus
G'	Pa	storage modulus
G''	Pa	loss modulus
G_i	Nm^{-1}	interfacial shear elasticity
g	ms^{-2}	standard acceleration
Ga		Galilei number
H	m	gap width
h	m	height, film thickness
$\bar{I}_{x,y}$		mean grey scale of the image section underneath the template
K	m^2	foam permeability
K_H	Pa m^3 mol^{-1}	Henry adsorption constant
K_L	mol^{-1}	equilibrium Langmuir adsorption constant
K_{mobile}	m^2	Plateau border permeability for mobile interfaces
K_{rigid}	m^2	Plateau border permeability for rigid interfaces

k		numerical constant
k_B	J K^{-1}	Boltzmann constant
k_{Pb}		dimensionless Plateau-border permeability
k_v	Pa s	foam consistency
L	m	length
l_c	m	capillary length
M	Nm	torque
m	kg	mass
N		number of neighboring bubbles
n		number of bubbles per unit volume, number of template sizes
p	Pa	pressure
P_c	Pa	capillary pressure
p_{32}		polydispersity parameter
Q_g	m^3s^{-1}	gas volume flow
Q_l	m^3s^{-1}	liquid volume flow
Q_0		cumulative frequency distribution
q_0	mm^{-1}	frequency density distribution
Q_2		cumulative area distribution
q_2	mm^{-2}	area density distribution
Q_3		cumulative volume distribution
q_3	mm^{-3}	volume density distribution
R	m	bubble radius
R_B	m	bob radius
R_{crit}	m	critical bubble radius
R_{cup}	m	cup radius
R_g	kg $m^2s^{-2}mol^{-1}K^{-1}$	gas constant
$R_{lamella}$	m	lamella size

R_{Pb}	m	Plateau border curvature
R_{plate}	m	plates radius
R_{vane}	m	vane rotor radius
R_0	m	initial bubble radius
r	m	cone tip curvature, distance from the rotational axis
r_c	m	critical cone tip curvature
Re		Reynolds number
S	m^2	total interfacial area, cross-section area, bubble surface area
S_0	m^2	undeformed spherical bubble surface
T	$°C$	temperature
t	s	time
$\bar{T}$		mean grey scale of the template image
t_{foam}	s	foam age
U	m s^{-1}	velocity
U_l	m s^{-1}	liquid flow velocity
u_{foam}	m s^{-1}	flow velocity inside foam
u_{wall}	m s^{-1}	flow velocity at the wall
V	l	Volume
We		Weber number

Greek symbols

$ß$		numerical constant
Γ	mol m^{-2}	surface concentration
Γ_{max}	mol m^{-2}	maximum interfacial concentration
γ		strain
γ_{crit}		critical deformation
γ_{xy}		interfacial strain

γ_0		strain amplitude
$\dot{\gamma}$	s^{-1}	shear rate
δ	°	phase angle
ε		surface excess
Φ	rad	displacement
φ		gas volume fraction
φ_l		liquid volume fraction
$\varphi_{l,fcc}$		liquid fraction in face-centered cubic structures
$\varphi_{l,rcp}$		liquid fraction for random closed packed spheres
Π	Pa	osmotic pressure, surface pressure
Π_{crit}	Pa	critical osmotic pressure
$\Pi_{disjoin}$	Pa	disjoining pressure
κ	Sm^{-1}	solution conductivity
η	Pa s	dynamic viscosity
$\eta_{interface}$	Pa s m	interfacial viscosity
η_l	Pa s	liquid viscosity
η_∞	Pa s	fluid viscosity in the high frequency limit
ω	rad s^{-1}	angular frequency
ω_c	rad s^{-1}	characteristic relaxation frequency
ρ	kg m^{-3}	density
σ	Nm^{-1}	interfacial tension
σ_{eq}	Nm^{-1}	equilibrium interfacial tension
σ_0	Nm^{-1}	interfacial tension of pure water
τ	Pa	shear stress inside the foam, dummy variable
τ_v	Pa	viscous stress
τ_0	Pa	shear stress amplitude

Abbreviations

CMC	carboxymethyl cellulose
GISANS	grazing incidence small angle neutron scattering
GISAX	grazing incidence small angle x-ray scattering
LPI	lupin protein isolate
LVE	linear-viscoelastic regime
NR	neutron reflectometry
XRR	X-ray reflectometry
ZNCC	zero normalized cross correlation